TWO-DIMENSIONAL NANOSTRUCTURING OF METAL HEXABORIDES

AND METAL PHOSPHATES

By

MONIKA MILKOVSKA

(Under the Direction of Tina T. Salguero)

ABSTRACT

Two-dimensional materials offer a variety of exciting properties and their synthesis has been tailored to many different materials. The 2D nanostructuring of metal borides is brand new avenue for these hard, high melting point compounds. Nanosheets of metal phosphates, on the other hand, have been synthesized previously due to their application in battery storage with various degree of success. Chapter II describes the modification of LaB_6 using a top-down Mg^{2+} incorporation technique, its exfoliation into nanosheets and the comparison of the obtained results to similar lithiation approaches. Chapters III and IV detail the same methodology applied to CaB_6 and SrB_6/BaB_6, respectively, and explain the differences and similarities in the chemistry of the three alkaline-earth metal borides. And finally, Chapter V illustrates the solvothermal synthesis of $LiCoPO_4$ nanosheets and the tuning of lateral dimensions of previously synthesized $LiMnPO_4$ ones using ball-milling techniques.

INDEX WORDS: two dimensional materials, nanosheets, metal hexaborides, metal phosphates, magnesium incorporation, exfoliation, battery materials, solvothermal reactions

TWO-DIMENSIONAL NANOSTRUCTURING OF METAL HEXABORIDES AND METAL PHOSPHATES

By

MONIKA MILKOVSKA

B.Sc., Furman University, 2014

A Dissertation Submitted to the Graduate Faculty of the University of Georgia in Partial Fulfillment of the Requirements for the Degree

DOCTOR OF PHILOSOPHY

ATHENS, GEORGIA

2020

TWO-DIMENSIONAL NANOSTRUCTURING OF METAL HEXABORIDES

AND METAL PHOSPHATES

By

MONIKA MILKOVSKA

Major Professor: Tina T. Salguero

Committee: Michael Johnson

Paul Schroeder

Electronic Version Approved:

Ron Walcott
Interim Dean of the Graduate School
The University of Georgia
May 2020

DEDICATION

To all of the extraordinary women in my family

ACKNOWLEDGEMENTS

I would like to thank my entire family for all of their support throughout the years, especially the generations of amazing women who showed me that nothing is impossible. My mom, Stefka, for pushing me to do better and to be better. My sister, Raya, for all of her advice and guidance. My grandma, Mona, for all of her unwavering love even from across the ocean. My niece, Yanna, for being my light at the end of the tunnel.

I would also like to acknowledge my mentor, prof. Tina T. Salguero, for being the greatest PI a graduate student could ask for. I could never imagine doing what I did throughout my PhD career without your help and direction. Many thanks to all the Salguero group members, past and present, for all of their support, mentorship and friendship. Especially Mayra Pedraza and Yassamin Ghafouri for keeping me sane, when things got rough, and Matt Bloodgood, Greg Neher and Nick Nguyen for teaching how to be fearless in lab.

Furthermore, I would also like to recognize my committee members, prof. Michael Johnson and prof. Paul Schroeder, for providing invaluable advice and guidance throughout my UGA career.

Finally, I would like to thank Taku Cowger for being my biggest cheerleader throughout these tough six years. Thank you for believing in me even when I didn't!

TABLE OF CONTENTS

Page

CHAPTER 1

INTRODUCTION AND LITERATURE REVIEW

Two-Dimensional Materials

The study of two-dimensional (2D) materials, which was popularized in large by graphene, has extended to many different materials beyond it in the past decade. While initial work focused heavily on the 2D allotrope of carbon after the ground breaking publication by Novoselov and coworkers in 2004,[1] materials such as h-BN,[2] metal oxides,[3] metal hydroxides,[4] metal carbides,[5] metal chalcogenides[6] and many others have been explored with the goal to confine them in one dimension. Quickly, scientists discovered that exfoliation of these materials

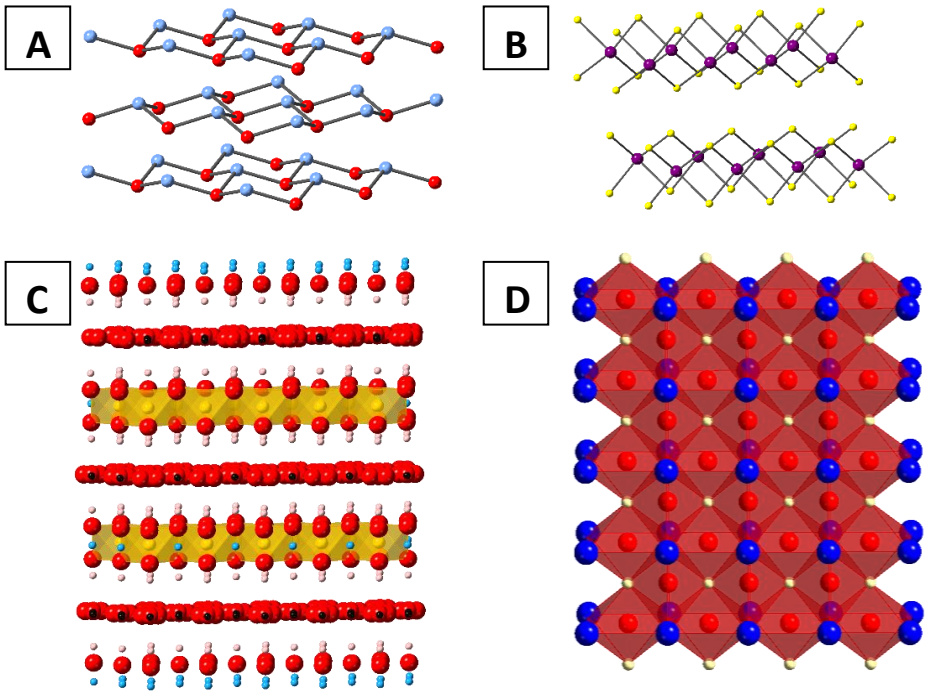

Figure 1.1 Crystal structures of h-BN (A), MoS_2 (B), $MgAl(OH)_3(CO_3)$ (C) and $BaTiO_3$ (D)

in not only possible, but it resulted in a variety of new or improved electronic, optical and chemical properties.

Classes of 2D Materials

In order to optimize the synthesis and integration of 2D materials, it is important to grasp the broad range of structures they can possess. There're three major classes of 2D materials known to date – (1) layered van der Waals materials, (2) layered ionic materials and (3) non-layered materials.

(1) Layered van der Waals materials have crystals consisting of ionically or covalently bound atoms forming layers, which are held together by weak van der Waals forces in meV/atom range perpendicular to the planar direction.[7] While graphene and h-BN remain the prime example of this group, one versatile subgroup of this family is the layered metal dichalcogenides (LMDC). They have a stoichiometry of MX_2 where M=Ti, Zr, Hf, V, Mo, W, Nb, Ta or Re and X=S, Se or Te and their structure consists of hexagonally packed MX_6 octahedra (for d^0, d^3 and some d^1 metals) or trigonal prisms (d^1 and d^2 metals).[8] Each layer consists of multiple polyhedra sharing edges with the six closest units. With such a wide variety of compositions in this group as well as their well-established polymorphism, the LMDCs have many interesting properties stemming from their conversion to two-dimensional morphologies. They can display tunable bandgap that transitions from indirect in the bulk to direct once converted to the 2D material,[9] charge density waves[10] and superconductivity.[11] More recently, alloying to LMDCs two-dimensional materials has aimed to produce synergistic effects. For example, $Mo_{(1-x)}W_xSe_2$ monolayers show photoluminescent behavior different from the two binary compounds,[12] while $Mo(S_xSe_{1-x})_2$ exhibits an increase in HER activity over both MoS_2 and $MoSe_2$.[13]

(2) Layered ionic compounds are a broad group of compounds with much stronger inlayer bonding than the van der Waals materials described above. This category includes many different compositions and structures – oxides, hydroxides, carbides, etc. Within the oxide group, some common examples include (a) perovskite-like structures such as $KCaNb_3O_{10}$,[14] (b) cation-exchanged oxides such as $LiCoO_2$, which is a known battery material[15] and water-oxidation catalyst,[16] and (C) other complex metal oxides such as La_2CuO_4, which is a superconducting material.[17] Moreover, some ternary ionic layered materials are shown to be structurally related to different van der Waals materials though removal of the interlayer atom (ex. MXenes from MAX structures).[18] This relationship allows for a comparative study of the properties between the two types of layered materials.

(3) Non-layered materials can be used to produce two-dimensional morphologies as well. These compounds consist of strongly bonded atoms in all three dimensions and in order to produce 2D structures, scientist must manage to break the thermodynamic equilibrium state and control the kinetics artificially. Similarly to the layered ionic compounds, the non-layered category contains a variety of materials. Metals such as Au, Pd and Ru constitute as significant amount of non-layered materials that are grown as 2D nanostructures. Their versatile applications in the sphere of catalysis has shown increasingly promising results. [19-21] Metal chalcogenides have also some non-layered structures. One of their most studied representatives are PbS, CdSe, SnSe and their alloys.[22-25]

Synthetic Approaches

2D materials can be synthesized through two types of approaches – top down or bottom up (Figure 1.2). The two strategies differ in the processes used in the creation of nanostructures –

the top down method forms nanoproducts from the bulk materials, the bottom up approach begins with the elements or molecular precursors to assemble the final nanomorphology.[26]

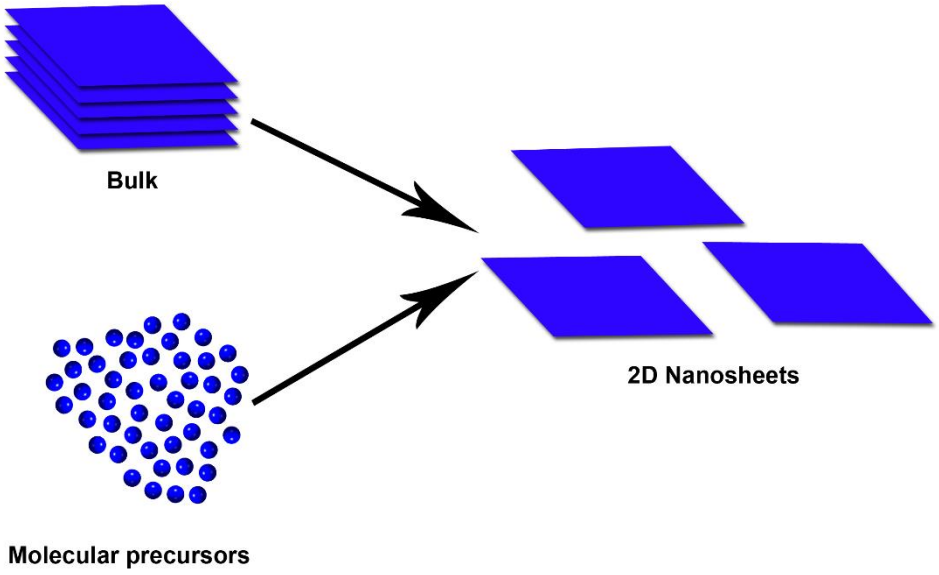

Figure 1.2 Top down vs bottom up synthetic approaches

(1) Top down approaches employ either physical- or chemical-based processes. The former the typically uses mechanical force or ultrasonic wave, while the latter depends on a chemical reaction to form the single- and several-layered two-dimensional morphologies. Microchemical exfoliation using the scotch tape methods became popular with the exfoliation of graphite into graphene[1], but quickly became popular with van der Waals materials as fundamental research on them was executed.[27] However, this approach was proven difficult to scale up, so more productive methods were developed. Ultrasonic exfoliation, for example, showed that appropriate solvents, that can prevent aggregation, can yield a well-dispersed, uniform 2D material. In a study of the most effective solvents for liquid exfoliation of MoS_2 and WS_2, Coleman and coworkers demonstrated that *n*-vinylpyrrolidone was best for the former, while DMSO was most suitable for the latter.[28]

While the previous two methods were appropriate for van der Waals materials, they weren't useful for layered ionic solids due to their inherently stronger bonding. Thus methods like ion-exchange exfoliation were developed. The technique takes advantage of the presence of an interlayer in the ionic layered materials, which is modified via an ion exchange; osmotic swelling leading to a high degree of interlayer expansion and exfoliation in solution complete the process.[29] Researchers have demonstrated the practicality and versatility of the process in the delamination of a wide range of oxides and hydroxides.[4, 30]

(2) Bottom-up strategies combat the issue of creating nanostructures from non-layered materials. They allow for precise control of morphology, crystallite size, facets and other important features of the 2D structures created through them.

Wet chemical methods such as hydro/solvothermal synthesis utilize relatively low temperatures (100-250 °C) and produce high yields.[31-33] They are shown to be sensitive to precursor concentration, solvents and surfactants, but are also scalable and usually low cost.[9] Often times these techniques use a structure-directing reagents such as PVP, which was successfully used to form ultrathin Rh nanosheets[31] and hexagonally shaped platelets of γ-Ga_2O_3.[34] Additionally, the help of templates is often used to synthesize materials confined in a specific dimension. The template can be easily removed through adjusting the pH or increasing temperature. Nonlayered materials such as α-Fe_2O_3[35] or $CuInS_2$[36] have been synthesized using a using a CuO and CuSe template respectively.

Epitaxial growth techniques such as chemical vapor deposition (CVD) have been employed to generate high-quality 2D materials. In CVD, a gaseous material reacts in either the vapor phase or on the surface of a substrate. Many parameters such as temperature, carrier gas flow rate, pressure and nature of the substrate can be varied to achieve a specific size,

morphology and orientation of the 2D structure. More significantly, the number of layers can be precisely tuned.[37] This is especially important for metal chalcogenides, which have demonstrated a band gap increase with the decrease in the number of layers.[38] Recently, the CVD method has also been used to create 2D heterostructures with interesting properties related to the layer-to-layer interaction of the different materials.[39]

Topochemical synthesis is typically a reaction that introduces a guest species into a host structure, resulting in a substantial structural changes of the host.[40] This type of 2D material synthesis can be applied to both layered and non-layered materials. For example, CaF_2 nanosheets were converted topochemically into $LaF_{3-2x}O_x$ nanosheets during a reaction with a lanthanum salts.[41] On the other hand, to produce 2D structures from nonlayered metal nitrides, metal oxides can be reduced in ammonia. For example, 2D h-MoO_3 served as a precursor to form MoN nanosheets with thickness of 0.7 nm and excellent metallic conductivity.[42]

Applications

2D materials possess features such as symmetry and reduced dimensionality in one direction leading to the manifestation of unique properties varying from their bulk counterparts. Differences in band structure, presence of adatoms and defects can improve the materials intrinsic properties. Electronic, optical and chemical behavior steers these 2D materials towards improving a wide range of current technological devices. While application of these nanostructures is vast, we highlight some important examples below.

Field emission transistors (FETs) and sensors can be fabricated for several different semiconducting materials, most notably metal dichalcogenides[38] and black phosphorus.[43] They have an advantage over conventional silicon in possessing a built-in flexibility and together with

a suitable substrate, they can be used in flexible electronics.[44] Additionally, their sensing capabilities have been shown to detect a range of molecules at and below the ppm level by measuring changes in conductance.[45-46]

The bandgap of certain metal dichalcogenides falls in the optical and near-IR region. When exfoliated, the MX_2 materials become too thin to incorporate in high efficiency photovoltaics; photodetectors can be produced instead. Grossman and coworkers demonstrated that a monolayer of MoS_2 can absorb up to 10% of incident light from the visible spectrum, which is a significant improvement from the widely used Si.[47] Moreover, the sensitivity of MoS_2 nanosheets is ~ 10^3 A/W[48] and can be even improved five-fold when combined with graphene.[49]

Battery and supercapacitor electrodes require electrically conductive materials with high surface area in order to achieve high energy and power densities. Two-dimensional nanosheets can provide that with ease. For example, graphene with its high surface-to-mass ratio, great conductivity and mechanical strength has been used as the anode material for an advanced compact energy storage.[50] Additionally, the doped version of the material is used in the cathodes and different oxides and sulfides have shown promising capacitive properties as well.[51-53]

2D materials can also be used as topological insulators, i.e. materials that behave like typical insulators but conduct electrons at their edges very efficiently. Such materials can be incorporated in low-power electronic devices as well as spintronic devices, in which electron spin is used to encode information. Some examples include Xenes such as bismuthene[54] and chalcogenides such as WTe_2.[55]

Metal Hexaborides

The metal borides are a group of inorganic materials with a variety of stoichiometries and properties. They are generally divided into two groups based on the stoichiometry between the two elements in them – metal rich boride are ones with boron:metal (B:M) ratio of less than 2:1, while boron rich borides have a B:M > 2:1 (Figure 1.3).[56] In the metal-rich group, some common examples are MoB, which is used as an alternative to precious metal is catalysis,[57] ad Fe_2B, which is used in the production of steel.[58] Boron-rich boride, on the other hand, include ultra-high temperature ceramics like ZrB_2 and more exotic structures like YB_{66}.

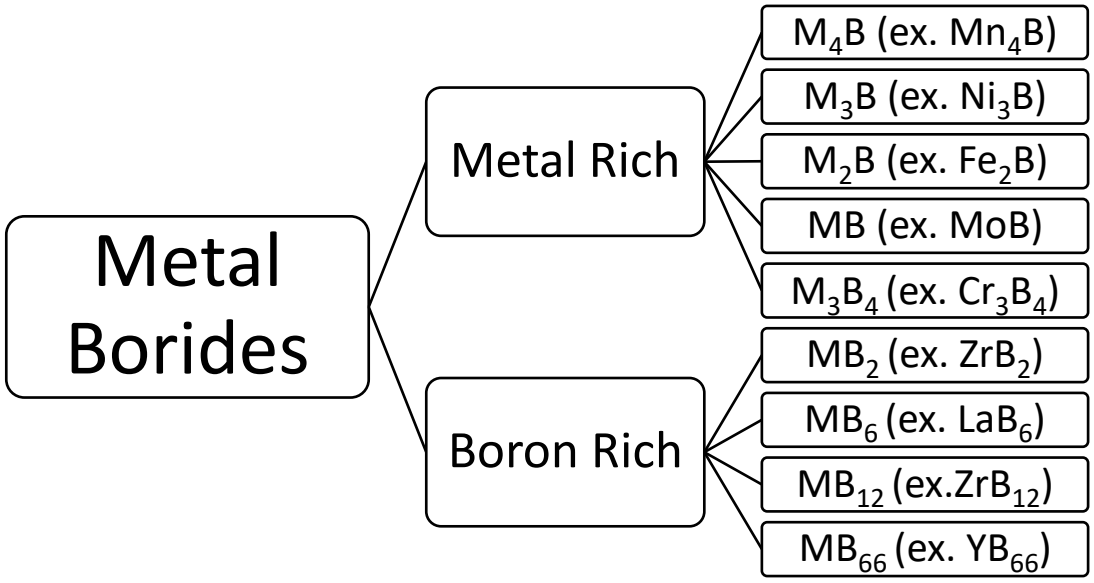

Figure 1.3. Classification of metal borides

Structure, Synthesis and Properties

Metal hexaborides (MB_6) belong to the boron-rich borides and have a B:M ratio of 6:1. There are two main groups of hexaborides – the alkaline earth metal hexaborides (M=Ca, Sr or Ba) and the rare earth metal hexaborides (M=Y, La, Ce, Pr, Nd, Sm, Eu or Gd). Metal hexaborides have a cubic crystal structure with $Pm\bar{3}m$ symmetry. The metal is at the corners of each unit cell coordinated by 24 boron atoms and each boron has a coordination of 5 and forms octahedra (Figure 1.4). The boron atoms are covalently bonded forming an extensive framework that is responsible for many of the unique physical and chemical properties of the hexaborides.[59] The boron lattice in inherently electron deficient as each boron distributes its 3 valence electrons to 5 bonds. Thus, the metal is required to donate electrons to make a stable structure; the hexaboride requires a metal cation with a charge of at least +2, which limits the hexaborides to the two groups described above.[60] Additionally, M-B bond is considered to be between ionic and covalent in character, while M-M bond shown to be ionic.[61]

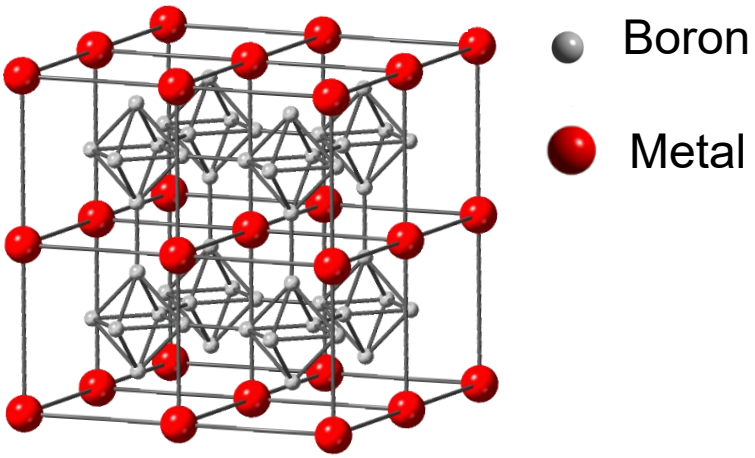

Figure 1.4. Crystal structure of metal hexaborides

The first hexaborides were synthesized by Moissan and Williams right before the turn of the 20th century – they produced CaB_6 and SrB_6 by reducing metal borates with aluminum in an arc furnace.[62] Since then many different synthetic approaches have been adopted to produce

hexaborides. Solid state reaction, for example, typically require high purity precursors and elevated temperatures above 1000 °C with borothermal and carbothermal being amongst the most widely used solid state methods.[63-64] Melt electrolysis and flux approaches utilize a molten salt bath, in which they dissolve the metal and boron precursors, to produce the hexaboride. Often the flux methods have an advantage of producing high quality single crystal hexaborides which can be up to several millimeters in length.[65] And finally, combustion reactions can also be used to synthesize hexaborides. In these reactions, the ignition of the precursor materials such as metal oxides and boron oxide drive the formation of the desired compounds.[66]

The hexaboride group possesses high melting points (typically above 2000 °C), excellent oxidative and thermal stability and relatively good hardness.[67] One of its most distinguishable features, however, is the electronic conductivity of its members. Depending on the number of electrons donated by the metal to the boron lattice, divalent hexaborides like CaB_6 and SrB_6 are semiconductors and the trivalent ones like LaB_6 are metallic.[59-60] LaB_6, which has also shown some superconducting properties at temperatures below 1K,[68] is a well-established thermionic electron emitter due to its low work function (2.6 eV) and low vapor pressure at high temperature.[69] These properties make it suitable to use in electron microscopes, electron-beam welders and free electron lasers. The alkaline earth hexaborides and their alloys, on the other hand, have a possible application as *n*-type thermoelectric materials with good Seebeck coefficients.[70]

An unusual phenomenon in MB_6 compounds is magnetism and an understanding its fundamental reasoning behind its presence has constituted the majority of the literature work in the area. For example, CeB_6 can display three distinct magnetic phases depending on the temperature and the complexities of its magnetism is also shown to depend on the purity of the

cerium compounds.[71] EuB_6 and CaB_6 have shown ferromagnetic properties attributed it to the alignment of localized Eu 4f moments and the joint effect of boron vacancies and impurities respectively.[72-73]

Nanostructuring

Much like other compounds in the literature, material scientists have nanostructured metal hexaborides in an effort to improve their existing properties or explore the potential formation of others. A range of boron sources could be used as starting materials, i.e. borohydrides, boron halogenides, boranes, boron oxide, boric acid, etc. The products obtained from these reactions have been 0D, 1D and some 3D nanomaterials.

(1) 0D nanomaterials of MB_6 are mostly nanoparticles. LaB_6 nanoparticles have been synthesized by several different routes – flask reaction at 360 °C using $NaBH_4$ as both boron source and solvent,[74] a molten salt route with KCl/LiCl eutectic salt at 600 °C[75] or a ball-milling of La salts with $LiBH_4$ followed by reaction in a stainless steel reactor.[76] The size of nanoparticles varied between 2-50 nm. Moreover, CeB_6 nanoparticles have also been produced by mechanically induced methods. For that reaction CeO_2-B_2O_3-Mg ternary system was used as a precursor and the size range of the particles was between 25-60 nm.[77]

(2) 1D nanostructures have been largely created using CVD methods. The deposition processes have been accomplished both with and without a metal catalyst. LaB_6 has been synthesized in nanowire,[78] nanotube[79] and nanoobelisk[80] morphologies via both methods, while PrB_6 nanorods[81] and nanowires[82] have been obtained via the catalyst-free route. From the alkaline earth hexaborides, SrB_6 and CaB_6 nanowires have been produced using a low-pressure CVD apparatus previously used to grown boron nanoribbons.[83-84]

(3) There are fewer 3D nanostructures of the metal hexaborides reported in the literature. One example is nanocubes of CeB_6, PrB_6 and NdB_6 that have been produced via a solid state reaction.[85] In this Mg-assisted co-reduction reaction, B_2O_3, a hydrated lanthanide chloride salt and Mg powder were reacted in an autoclave at 500 °C to produce pure, highly crystalline nanocubes with sizes ranging between 100 and 300 nm.

Research Approaches

Two-dimensional morphologies can give industrial adaptability to the hexaborides, since they are solution-processable, tend to lay flat and can form uniform coatings. Previously, complex techniques such pulsed laser deposition and arc plasma methods needed to be utilized to form thin films of the hexaborides.[86] Such approaches, however, require a substrate and give very little control over the thickness and uniformity of the layers. Synthetic approaches to produce free-standing 2D hexaborides have only recently begun to emerge.

There are a few reasons behind the difficult 2D nanostructuring of MB_6. On one hand, bottom up approaches may not be feasible since borides form at very high temperatures. Top-down methods, on the other hand, encounter issues in the challenging disassembly of the strongly bonded M-B framework. Thus, methods like mechanical exfoliation and sonication prove unfruitful and different strategies need to be employed. One top-down method, that has been successfully used to exfoliate layered van der Waals materials, is Li^+ intercalation. During this process, lithium ions are incorporated into a bulk material and then water in added to the modified material. The reaction with the solvent is very vigorous and leads to the disassembly of 3D structure of the compound and the formation of nanosheets. This methodology has been adapted successfully for MoS_2 and Bi_2Te_3.[87-88] More importantly, it was tested with metal borides as well – different borides were modified in either a solvated electron Li-NH_3(l) solution

or *n*-butyllithium solution and then reacted with water (aqueous exfoliation) or iodomethane (non-aqueous exfoliation) to form the nanoproduct.[89] The incorporation is hypothesized to occur in one of three ways: an ion exchange with either the metal or the boron in the metal boride or the metal ion can occupy the interstitial spaces (Figure 1.5). Additionally, once exfoliated the nanosheets are theorized to form either along the (001) plane or (111) plane.

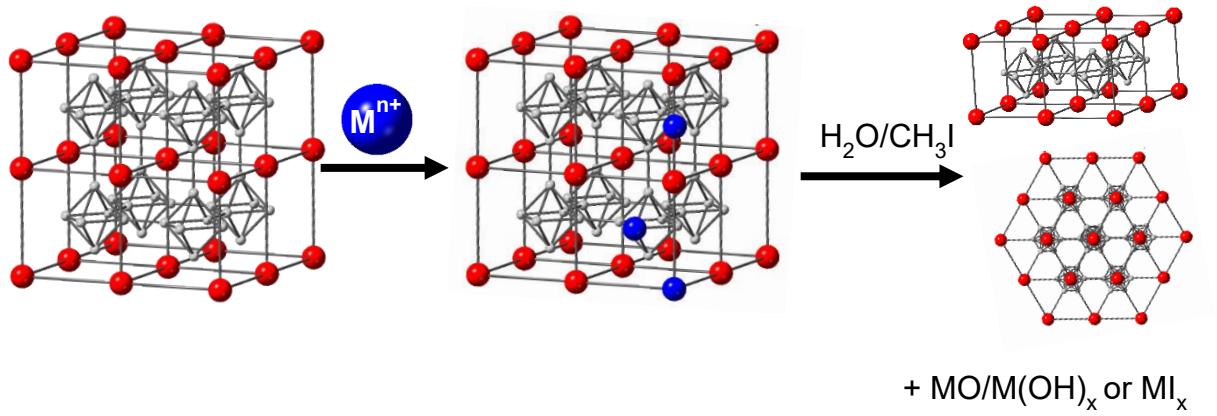

Figure 1.5. Metal incorporation and exfoliation strategy for the modification of MB_6

Several important key discoveries were made during the studies of metal boride modification with Li^+. Firstly, while studying LaB_6, it was found that the boride can produce nanosheets with thickness of 1-4 nm and lateral dimensions of 0.5-1 µm. ^{11}B and ^{139}La solid state NMR confirmed the presence of Li in the modified structure and showed a change in La environment after lithiation. No change was recorded in the B environment. Secondly, using the same conditions on CaB_6 produced much thicker platelets and nanosheets were formed only after a 3-month long reaction with *n*-butyllithium. Powder x-ray diffraction (PXRD) of the modified boride show the presence of additional peaks, which were matched to a LiB_9 compound. The formation of this species during lithiation sheds some light on the chemistry occurring during the modification of the boride. And finally, a reaction of SrB_6 with n-butyllithium at 80 °C yielded an unexpected morphology – nanoparticles were produced during the reaction of the modified

SrB_6 with water. A Li-B species was detected during these experiments as well, but PXRD and selected area electron diffraction (SAED) confirmed it was Li_2B_6 instead. This lithium boride species has a cubic crystal structure similar to that of the metal hexaborides used in these reactions. The difference in structure lies in the position of the metal atoms – in borides like SrB_6, the metal is in the corner of each cubic until cell, while in the Li_2B_6 case, the Li is positioned in the interstitial sites. This result indicates that the Li^+ occupies these spaces as the SrB_6 is modified. Overall, the results obtained from these three borides were the first steps to produce free standing 2D nanomorphologies of the metal hexaborides and produced invaluable information on their modification and chemistry.

In this work, we propose an alteration of the Li^+ incorporation method using Mg^{2+} to achieve the following research goals:

(1) Explore the chemical modification of MB_6 further.

(2) Expand on the exfoliation of metal hexaborides using Mg reagents.

(3) Determine differences and similarities between Mg and Li reactions.

(4) Find optimal conditions that yield nanosheets using the magnesiation method.

In our exploration of the chemistry of metal borides, we chose Mg^{2+} for several key reasons. The Mg^{2+} has a size similar to that of Li^+ (72 pm vs. 76 pm respectively) and is smaller than the metal ions in the borides we are studying. By using an ion with such dimensions, we hypothesize that size is not going to be an issue during the modification of the boride and the ion will be more easily incorporated as opposed to a bulkier alternative. Next, the presence magnesium can be detected by more easily available methods such as energy dispersive spectroscopy (EDS), which makes their characterization significantly less difficult. Finally, we

wanted to explore the effect of an ion from the same group as some of the metals in the borides. For example, we theorized that using Mg^{2+} might be able to reduce to total reaction time that is required to produce CaB_6 nanosheets.

In Chapters 2, 3 and 4, we explore the modification of LaB_6 and the three alkaline earth metal borides, i.e. CaB_6, SrB_6 and BaB_6. We use di-*n*-butylmagnesium as the Mg^{2+} source and we vary a range of parameters such as reaction time, temperature and bulk particle size in order to discover their effect on the magnesiated and exfoliated products. Finally, we use both aqueous and non-aqueous exfoliation techniques to compare the final nanomorphologies and expand on the adaptability of this technique, particularly in light of certain borides' instability in water.

Metal Phosphates

$LiMPO_4$ (M=Fe, Mn, Co or Ni) or LMPs are olivine-structured lithium transition-metal orthophosphates. They have attracted significant interest in the scientific community due to their potential application as cathode materials in energy storage devices such as lithium ion batteries (LIBs) and supercapacitors. While so far only $LiFePO_4$ has been successfully commercialized,[90] much effort has been dedicated to researching and adapting the other three group members.[33, 91]

Structure, Synthesis and Properties

LMPs have an orthorhombic crystal structure and belong to the *Pnma* space group. The unit cell is composed of PO_4 polyhedra with M^{2+} on the corner-sharing octahedral positions and Li^+ on the edge-sharing ones; the Li^+ and M^{2+} octahedra run parallel to the c axis and propagate along the b axis (Figure 1.6).[92] Thus, PO_4^{3-} tetrahedra constrain the Li^+, which form 1D conduction channels along the [010] direction. Stability is in one of the main advantages of LMPs. Firstly, the strong covalent bonds in the phosphate polyanion stabilize the oxygen,

making LMPs a stable and safe cathode material.[93] Additionally, work on $LiCoPO_4$ shows that when the lithium ions are removed from the material during charging, the $CoPO_4$ phase has the same olivine structure as the LMP and relatively small lattice volume changes occur.[94] So major volume fluctuations during the charge-discharge process can be prevented.

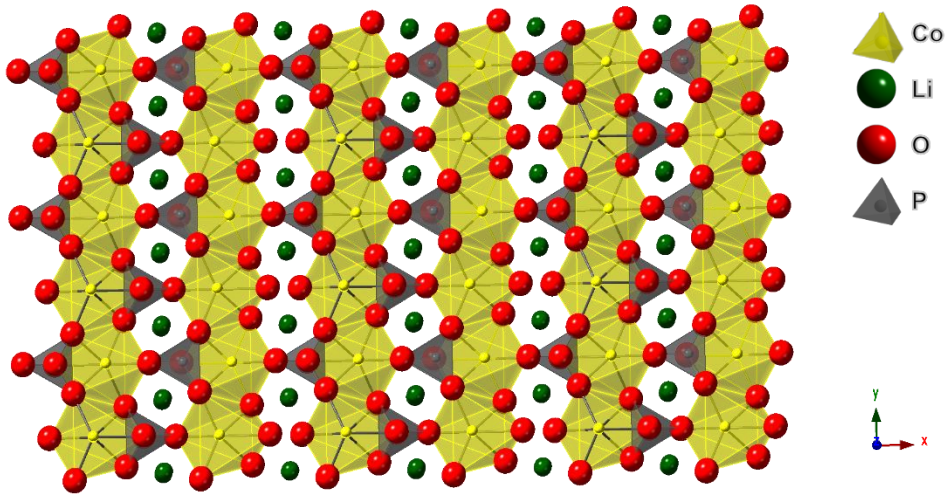

Figure 1.6. Crystal structure of $LiMPO_4$

There's been a variety synthetic approaches to produce LMPs. Their high energy density, thermal stability and relatively law materials cost have made them an active target to be produced on the nanoscale in order to optimize their application in energy storage devices. [95] Particularly, nanostructuring where facet-controlled growth can be tuned has become the leading trend in an effort to shorten Li^+ diffusion path lengths and improve battery performance.

(1) Solid state reactions used to produce LMPs typically require a Li salt such as Li_2CO_3 or $LiCH_3COO$, a metal source like $M(CH_3COO)_2$ or M_3O_4 and a phosphate source such as $(NH_4)_2HPO_4$. They typically involve high temperatures (300-700 °C), multiple rounds grinding and calcination to produce the final product, which often leads to agglomeration.[96] For this reason, often times growth inhibitors such as carbonates are added to the reaction in order to

obtain the desired nanoparticles.[97] While nanoparticles appear to be the predominant product of solid state reactions, other morphologies such as nanorods have been grown through these methods.[98]

(2) Sol-gel methods typically require longer reaction times but have the advantage of creating products with high purity and homogeneity. During a sol-gel reaction, the starting materials are first dissolved and then gradually a gel-like network forms, which is subsequently calcined to form the final product.[99] The precursors are often similar to those of the solid state reactions described above and water is the most commonly used solvent. However, organic solvents like ethanol can also be employed as well.[100] The morphology can vary vastly depending on the chelating agent: for example, $LiMnPO_4$ had a spherical microparticle morphology when made with tributyl phosphate as the chelator [101] vs petal-like one when citric acid is used in the same role.[102]

(3) Hydrothermal and solvothermal reactions offer the advantage of doing reactions at lower temperature and controlling the size and morphology of the final product with precision. These advantages make them a popular synthetic route to produce LMPs. Additionally, these methods often produce pure, highly crystalline solids; this minimizes the chance of blocking the 1D channels, in which the Li^+ travels, by ensuring the minimization of defects and impurities.[92] In hydrothermal/solvothermal reactions, the solvent and the added surfactants play a crucial part in the formation of the final products. Compounds like PVP, citric acid or ethylene glycol have been used to synthesize LMPs and direct their growth. Spherical particles, hexagonal platelets, nanocubes and nanorods are some of the example nanomorphologies produced through these versatile methods.[103-106]

Research approaches

Two-dimensional LMPs offer morphological and size advantages over other nanostructures when it comes to their application in energy storage. They offer high contact area with the electrolyte and fast lithium transport due to their constraint to two dimensions. Particularly, nanosheets with exposed (010) facets are highly desirable to improve the Li diffusion in and out of the material.[95] Moreover, it is important to be able to produce nanosheets using scalable methods in order to improve their industry processability.

To this end, out research goals are:

(1) Synthesize $LiCoPO_4$ using a facile solvothermal method.

(2) Investigate the influence of reaction conditions and precursors on the nanosheet morphology of $LiCoPO_4$ and its crystal orientation.

(3) Explore the variation in lateral dimensions on $LiMnPO_4$ nanosheets using dry and wet ball-milling.

In Chapter 5, we explore two materials from the Co and Mn compounds of the LMP group. First, we explore the synthesis of $LiCoPO_4$ nanosheets using a facile solvothermal method with a $Co_3(PO_4)_2 \cdot 4H_2O$ nanosheet precursor. Previously, nanosheets of this material have been synthesized using hydrothermal/solvothermal methods with various amount of success. Issues such as uniformity, size, thickness or crystal facets have been encountered.[33, 95, 105] Utilizing a polyol as co-solvent to water aims to provide control over particle size, morphology and crystal orientation.[107] Furthermore, we study the variation of lateral dimensions of micron-sized $LiMnPO_4$ nanosheets. The 2D material, which was previously synthesized through a similar solvothermal method,[108] has shown promising battery performance. However, we theorize that

having control over the size of the nanosheets, while still maintaining their dimensionality, could improve their electrochemical performance significantly.[107] Thus, we utilize dry and wet ball-milling in order to control the lateral dimensions of the $LiMnPO_4$ nanosheets.

References

1. Novoselov, K. S.; Geim, A. K.; Morozov, S. V.; Jiang, D.; Zhang, Y.; Dubonos, S. V.; Grigorieva, I. V.; Firsov, A. A., Electric Field Effect in Atomically Thin Carbon Films. *Science* **2004,** *306* (5696), 666.

2. Zhang, K.; Feng, Y.; Wang, F.; Yang, Z.; Wang, J., Two dimensional hexagonal boron nitride (2D-hBN): synthesis, properties and applications. *Journal of Materials Chemistry C* **2017,** *5* (46), 11992-12022.

3. Osada, M.; Sasaki, T., Exfoliated oxide nanosheets: new solution to nanoelectronics. *Journal of Materials Chemistry* **2009,** *19* (17), 2503-2511.

4. Ma, R.; Liu, Z.; Li, L.; Iyi, N.; Sasaki, T., Exfoliating layered double hydroxides in formamide: a method to obtain positively charged nanosheets. *Journal of Materials Chemistry* **2006,** *16* (39), 3809-3813.

5. Anasori, B.; Xie, Y.; Beidaghi, M.; Lu, J.; Hosler, B. C.; Hultman, L.; Kent, P. R. C.; Gogotsi, Y.; Barsoum, M. W., Two-Dimesionlal, Ordered, Double Transition Metal Carbides *ACS Nano* **2015,** *9* (10), 9507-9516.

6. Zhang, X.; Li, W.; Ling, Z.; Zhang, Y.; Xu, J.; Wang, H.; Chen, G.; Wei, B., Facile synthesis of solution-processed MoS_2 nanosheets and their application in high-performance ultraviolet organic light-emitting diodes. *Journal of Materials Chemistry C* **2019,** *7* (4), 926-936.

7. Duong, D. L.; Yun, S. J.; Lee, Y. H., van der Waals Layered Materials: Opportunities and Challenges. *ACS Nano* **2017,** *11* (12), 11803-11830.

8. Wilson, J. A.; Yoffe, A. D., The transition metal dichalcogenides discussion and interpretation of the observed optical, electrical and structural properties. *Advances in Physics* **1969,** *18* (73), 193-335.

9. Parvez, K., Chapter 1 - Two-Dimensional Nanomaterials: Crystal Structure and Synthesis. In *Biomedical Applications of Graphene and 2D Nanomaterials*, Nurunnabi, M.; McCarthy, J. R., Eds. Elsevier: 2019; pp 1-25.

10. Goli, P.; Khan, J.; Wickramaratne, D.; Lake, R. K.; Balandin, A. A., Charge Density Waves in Exfoliated Films of van der Waals Materials: Evolution of Raman Spectrum in $TiSe_2$. *Nano Letters* **2012,** *12* (11), 5941-5945.

11. Costanzo, D.; Jo, S.; Berger, H.; Morpurgo, A. F., Gate-induced superconductivity in atomically thin MoS_2 crystals. *Nature Nanotechnology* **2016,** *11* (4), 339-344.

12. Wang, G.; Robert, C.; Suslu, A.; Chen, B.; Yang, S.; Alamdari, S.; Gerber, I. C.; Amand, T.; Marie, X.; Tongay, S.; Urbaszek, B., Spin-orbit engineering in transition metal dichalcogenide alloy monolayers. *Nature Communications* **2015,** *6* (1), 10110.

13. Kiran, V.; Mukherjee, D.; Jenjeti, R. N.; Sampath, S., Active guests in the MoS_2/$MoSe_2$ host lattice: efficient hydrogen evolution using few-layer alloys of $MoS_{2(1-x)}Se_{2x}$. *Nanoscale* **2014,** *6* (21), 12856-12863.

14. Yuan, H.; Nguyen, M.; Hammer, T.; Koster, G.; Rijnders, G.; ten Elshof, J. E., Synthesis of $KCa_2Nb_3O_{10}$ Crystals with Varying Grain Sizes and Their Nanosheet Monolayer Films As Seed Layers for PiezoMEMS Applications. *ACS Applied Materials & Interfaces* **2015,** *7* (49), 27473-27478.

15. Xue, L.; Savilov, S. V.; Lunin, V. V.; Xia, H., Self-Standing Porous $LiCoO_2$ Nanosheet Arrays as 3D Cathodes for Flexible Li-Ion Batteries. *Advanced Functional Materials* **2018,** *28* (7), 1705836.

16. Wang, J.; Li, L.; Tian, H.; Zhang, Y.; Che, X.; Li, G., Ultrathin $LiCoO_2$ Nanosheets: An Efficient Water-Oxidation Catalyst. *ACS Applied Materials & Interfaces* **2017,** *9* (8), 7100-7107.

17. Leggett, A. J., Cuprate Superconductivity: Dependence of T_c on the *c*-Axis Layering Structure. *Physical Review Letters* **1999,** *83* (2), 392-395.

18. McKinney, Robert W.; Gorai, P.; Manna, S.; Toberer, E.; Stevanović, V., Ionic vs. van der Waals layered materials: identification and comparison of elastic anisotropy. *Journal of Materials Chemistry A* **2018,** *6* (32), 15828-15838.

19. Zhang, Y.; Cui, Z.; Li, L.; Guo, L.; Yang, S., Two-dimensional structure Au nanosheets are super active for the catalytic reduction of 4-nitrophenol. *Physical Chemistry Chemical Physics* **2015,** *17* (22), 14656-14661.

20. He, C.; Tao, J.; Shen, P. K., Solid Synthesis of Ultrathin Palladium and Its Alloys' Nanosheets on RGO with High Catalytic Activity for Oxygen Reduction Reaction. *ACS Catalysis* **2018,** *8* (2), 910-919.

21. Kong, X.; Xu, K.; Zhang, C.; Dai, J.; Norooz Oliaee, S.; Li, L.; Zeng, X.; Wu, C.; Peng, Z., Free-Standing Two-Dimensional Ru Nanosheets with High Activity toward Water Splitting. *ACS Catalysis* **2016,** *6* (3), 1487-1492.

22. Wu, W.-Y.; Chakrabortty, S.; Guchhait, A.; Wong, G. Y. Z.; Dalapati, G. K.; Lin, M.; Chan, Y., Solution-Processed 2D PbS Nanoplates with Residual Cu_2S Exhibiting Low Resistivity and High Infrared Responsivity. *Chemistry of Materials* **2016,** *28* (24), 9132-9138.

23. Gerdes, F.; Navío, C.; Juárez, B. H.; Klinke, C., Size, Shape, and Phase Control in Ultrathin CdSe Nanosheets. *Nano Letters* **2017,** *17* (7), 4165-4171.

24. Wang, Q.; Wen, Y.; Yao, F.; Huang, Y.; Wang, Z.; Li, M.; Zhan, X.; Xu, K.; Wang, F.; Wang, F.; Li, J.; Liu, K.; Jiang, C.; Liu, F.; He, J., BN-Enabled Epitaxy of $Pb_{1-x}Sn_xSe$ Nanoplates on SiO_2/Si for High-Performance Mid-Infrared Detection. *Small* **2015,** *11* (40), 5388-5394.

25. Li, L.; Chen, Z.; Hu, Y.; Wang, X.; Zhang, T.; Chen, W.; Wang, Q., Single-Layer Single-Crystalline SnSe Nanosheets. *Journal of the American Chemical Society* **2013,** *135* (4), 1213-1216.

26. Yu, H.-D.; Regulacio, M. D.; Ye, E.; Han, M.-Y., Chemical routes to top-down nanofabrication. *Chemical Society Reviews* **2013,** *42* (14), 6006-6018.

27. Magda, G.; Pető, J.; Dobrik, G.; Hwang, C.; Biro, L.; Tapaszto, L., Exfoliation of large-area transition metal chalcogenide single layers. *Scientific Reports* **2015,** *5*, 14714.

28. Coleman, J. N.; Lotya, M.; O'Neill, A.; Bergin, S. D.; King, P. J.; Khan, U.; Young, K.; Gaucher, A.; De, S.; Smith, R. J.; Shvets, I. V.; Arora, S. K.; Stanton, G.; Kim, H.-Y.; Lee, K.; Kim, G. T.; Duesberg, G. S.; Hallam, T.; Boland, J. J.; Wang, J. J.; Donegan, J. F.; Grunlan, J. C.; Moriarty, G.; Shmeliov, A.; Nicholls, R. J.; Perkins, J. M.; Grieveson, E. M.; Theuwissen, K.; McComb, D. W.; Nellist, P. D.; Nicolosi, V., Two-Dimensional Nanosheets Produced by Liquid Exfoliation of Layered Materials. *Science* **2011,** *331* (6017), 568.

29. Ma, R.; Sasaki, T., Two-Dimensional Oxide and Hydroxide Nanosheets: Controllable High-Quality Exfoliation, Molecular Assembly, and Exploration of Functionality. *Accounts of Chemical Research* **2015,** *48* (1), 136-143.

30. Ebina, Y.; Sasaki, T.; Watanabe, M., Study on exfoliation of layered perovskite-type niobates. *Solid State Ionics* **2002,** *151* (1), 177-182.

31. Duan, H.; Yan, N.; Yu, R.; Chang, C.-R.; Zhou, G.; Hu, H.-S.; Rong, H.; Niu, Z.; Mao, J.; Asakura, H.; Tanaka, T.; Dyson, P. J.; Li, J.; Li, Y., Ultrathin rhodium nanosheets. *Nature Communications* **2014,** *5* (1), 3093.

32. Sun, Z.; Liao, T.; Dou, Y.; Hwang, S. M.; Park, M.-S.; Jiang, L.; Kim, J. H.; Dou, S. X., Generalized self-assembly of scalable two-dimensional transition metal oxide nanosheets. *Nature Communications* **2014,** *5* (1), 3813.

33. Brutti, S.; Manzi, J.; De Bonis, A.; Di Lecce, D.; Vitucci, F.; Paolone, A.; Trequattrini, F.; Panero, S., Controlled synthesis of $LiCoPO_4$ by a solvo-thermal method at 220°C. *Materials Letters* **2015,** *145*, 324-327.

34. Yang, Z.; Song, L. X.; Wang, Y. Q.; Ruan, M. M.; Teng, Y.; Xia, J.; Yang, J.; Chen, S. S.; Wang, F., Hexagonal nanoplates of high-quality γ-gallium oxide: controlled synthesis and good heterogeneous catalytic performance for thiophenes. *Journal of Materials Chemistry A* **2018,** *6* (7), 2914-2921.

35. Cheng, W.; He, J.; Yao, T.; Sun, Z.; Jiang, Y.; Liu, Q.; Jiang, S.; Hu, F.; Xie, Z.; He, B.; Yan, W.; Wei, S., Half-Unit-Cell alpha-Fe_2O_3 Semiconductor Nanosheets with Intrinsic and Robust Ferromagnetism. 2014; Vol. 136, pp 10393-10398.

36. Bi, W.; Zhou, M.; Ma, Z.; Zhang, H.; Yu, J.; Xie, Y., $CuInSe_2$ ultrathin nanoplatelets: novel self-sacrificial template-directed synthesis and application for flexible photodetectors. 2012, p 9162.

37. You, J.; Hossain, M. D.; Luo, Z., Synthesis of 2D transition metal dichalcogenides by chemical vapor deposition with controlled layer number and morphology. *Nano Convergence* **2018,** *5* (1), 26.

38. Lan, Y.-W.; Torres Jr., C. M.; Tsai, S.-H.; Zhu, X.; Shi, Y.; Li, M.-Y.; Li, L.-J.; Yeh, W.-K.; Wang, K. L., Atomic-Monolayer MoS_2 Band-to-Band Tunneling Field-Effect Transistor. *Small* **2016,** *12* (41), 5676-5683.

39. Jin, C.; Kim, J.; Suh, J.; Shi, Z.; Chen, B.; Fan, X.; Kam, M.; Watanabe, K.; Taniguchi, T.; Tongay, S.; Zettl, A.; Wu, J.; Wang, F., Interlayer electron–phonon coupling in WSe_2/hBN heterostructures. *Nature Physics* **2017,** *13* (2), 127-131.

40. Xiao, X.; Wang, H.; Urbankowski, P.; Gogotsi, Y., Topochemical synthesis of 2D materials. 2018; Vol. 47, pp 8744-8765.

41. Ramachandran, R.; Johnson-McDaniel, D.; Salguero, T., Formation and Scrolling Behavior of Metal Fluoride and Oxyfluoride Nanosheets. *Chemistry of Materials* **2016,** *28*.

42. Xiao, X.; Yu, H.; Jin, H.; Wu, M.; Fang, Y.; Sun, J.; Hu, Z.; Li, T.; Wu, J.; Huang, L.; Gogotsi, Y.; Zhou, J., Salt-Templated Synthesis of 2D Metallic MoN and Other Nitrides. *ACS Nano* **2017,** *11* (2), 2180-2186.

43. Li, X.; Yu, Z.; Xiong, X.; Li, T.; Gao, T.; Wang, R.; Huang, R.; Wu, Y., High-speed black phosphorus field-effect transistors approaching ballistic limit. *Science Advances* **2019,** *5* (6), eaau3194.

44. Zhu, W.; Yogeesh, M. N.; Yang, S.; Aldave, S. H.; Kim, J.-S.; Sonde, S.; Tao, L.; Lu, N.; Akinwande, D., Flexible Black Phosphorus Ambipolar Transistors, Circuits and AM Demodulator. *Nano Letters* **2015,** *15* (3), 1883-1890.

45. Late, D. J.; Huang, Y.-K.; Liu, B.; Acharya, J.; Shirodkar, S. N.; Luo, J.; Yan, A.; Charles, D.; Waghmare, U. V.; Dravid, V. P.; Rao, C. N. R., Sensing Behavior of Atomically Thin-Layered MoS_2 Transistors. *ACS Nano* **2013,** *7* (6), 4879-4891.

46. Perkins, F. K.; Friedman, A. L.; Cobas, E.; Campbell, P. M.; Jernigan, G. G.; Jonker, B. T., Chemical Vapor Sensing with Monolayer MoS_2. *Nano Letters* **2013,** *13* (2), 668-673.

47. Bernardi, M.; Palummo, M.; Grossman, J. C., Extraordinary Sunlight Absorption and One Nanometer Thick Photovoltaics Using Two-Dimensional Monolayer Materials. *Nano Letters* **2013,** *13* (8), 3664-3670.

48. Lopez-Sanchez, O.; Lembke, D.; Kayci, M.; Radenovic, A.; Kis, A., Ultrasensitive photodetectors based on monolayer MoS_2. *Nature Nanotechnology* **2013,** *8* (7), 497-501.

49. Zhang, W.; Chuu, C.-P.; Huang, J.-K.; Chen, C.-H.; Tsai, M.-L.; Chang, Y.-H.; Liang, C.-T.; Chen, Y.-Z.; Chueh, Y.-L.; He, J.-H.; Chou, M.-Y.; Li, L.-J., Ultrahigh-Gain Photodetectors Based on Atomically Thin Graphene-MoS_2 Heterostructures. *Scientific Reports* **2014,** *4* (1), 3826.

50. Yang, X.; Cheng, C.; Wang, Y.; Qiu, L.; Li, D., Liquid-Mediated Dense Integration of Graphene Materials for Compact Capacitive Energy Storage. *Science* **2013,** *341* (6145), 534-537.

51. Li, Y.; Wang, J.; Li, X.; Geng, D.; Banis, M. N.; Li, R.; Sun, X., Nitrogen-doped graphene nanosheets as cathode materials with excellent electrocatalytic activity for high capacity lithium-oxygen batteries. *Electrochemistry Communications* **2012,** *18*, 12-15.

52. Tong, H.; Bai, W.; Yue, S.; Gao, Z.; Lu, L.; Shen, L.; Dong, S.; Zhu, J.; He, J.; Zhang, X., Zinc cobalt sulfide nanosheets grown on nitrogendoped graphene/carbon nanotube film as a highperformance electrode for supercapacitors. *Journal of Materials Chemistry A* **2016,** *4*, 11256–11263.

53. Li, Y.; Yao, J.; Uchaker, E.; Yang, J.; Huang, Y.; Zhang, M.; Cao, G., Leaf-Like V_2O_5 Nanosheets Fabricated by a Facile Green Approach as High Energy Cathode Material for Lithium-Ion Batteries. *Advanced Energy Materials* **2013,** *3* (9), 1171-1175.

54. Reis, F.; Li, G.; Dudy, L.; Bauernfeind, M.; Glass, S.; Hanke, W.; Thomale, R.; Schäfer, J.; Claessen, R., Bismuthene on a SiC substrate: A candidate for a high-temperature quantum spin Hall material. *Science* **2017,** *357* (6348), 287-290.

55. Fatemi, V.; Wu, S.; Cao, Y.; Bretheau, L.; Gibson, Q. D.; Watanabe, K.; Taniguchi, T.; Cava, R. J.; Jarillo-Herrero, P., Electrically tunable low-density superconductivity in a monolayer topological insulator. *Science* **2018,** *362* (6417), 926-929.

56. Serebryakova, T., Classification of borides. *Journal of the Less Common Metals* **1979,** *67* (2), 499-503.

57. Wang, X.; Tai, G.; Wu, Z.; Hu, T.; Wang, R., Ultrathin molybdenum boride films for highly efficient catalysis of the hydrogen evolution reaction. *Journal of Materials Chemistry A* **2017,** *5* (45), 23471-23475.

58. Rodriguez, G.; Campos-Silva, I.; Chávez-Gutiérrez, E.; Martínez-Trinidad, J.; Hernandez-Sanchez, E.; Torres-Hernández, A., Mechanical properties of FeB and Fe_2B layers estimated by Berkovich nanoindentation on tool borided steel. *Surface and Coatings Technology* **2013,** *215*, 291–299.

59. Etourneau, J.; Mercurio, J.-P.; Hagenmuller, P., Compounds Based on Octahedral B_6 Units: Hexaborides and Tetraborides. In *Boron and Refractory Borides*, Matkovich, V. I., Ed. Springer Berlin Heidelberg: Berlin, Heidelberg, 1977; pp 115-138.

60. Johnson, R. W.; Daane, A. H., Electron Requirements of Bonds in Metal Borides. *The Journal of Chemical Physics* **1963,** *38* (2), 425-432.

61. Bai, L.; Ma, N.; Liu, F., Structure and chemical bond characteristics of LaB_6. *Physica B: Condensed Matter* **2009,** *404* (21), 4086-4089.

62. Moissan, H.; Williams, P., *Sur la préparation et les propriétés des borures de calcium, de strontium et de baryum*. Gauthier-Villars: Paris, 1897.

63. Grechnev, G. E.; Baranovskiy, A. E.; Fil, V. D.; Ignatova, T. V.; Kolobov, I. G.; Logosha, A. V.; Shitsevalova, N. Y.; Filippov, V. B.; Eriksson, O., Electronic structure and bulk properties of MB_6 and MB_{12} borides. *Low Temperature Physics* **2008,** *34* (11), 921-929.

64. Serebryakova, T. I.; Marek, É. V., Conditions of preparation of calcium and barium hexaboride powders. *Soviet Powder Metallurgy and Metal Ceramics* **1969,** *8* (8), 608-612.

65. Muranaka, S.; Kawai, S., Crystal growth of alkaline earth hexaborides. *Journal of Crystal Growth* **1974,** *26*, 165-168.

66. Dou, Z.-h.; Zhang, T.-a.; Zhang, Z.-q.; Zhang, H.-b.; He, J.-c., Preparation and characterization of LaB_6 ultra fine powder by combustion synthesis. *Transactions of Nonferrous Metals Society of China* **2011,** *21* (8), 1790-1794.

67. Lafferty, J. M., Boride Cathodes. *Journal of Applied Physics* **1951,** *22* (3), 299-309.

68. Vandenberg, J. M.; Matthias, B. T.; Corenzwit, E.; Barz, H., Superconductivity of some binary and ternary transition-metal borides. *Materials Research Bulletin* **1975,** *10* (9), 889-894.

69. Swanson, L. W.; Gesley, M. A.; Davis, P. R., Crystallographic dependence of the work function and volatility of LaB_6. *Surface Science* **1981,** *107* (1), 263-289.

70. Takeda, M.; Terui, M.; Takahashi, N.; Ueda, N., Improvement of thermoelectric properties of alkaline-earth hexaborides. *Journal of Solid State Chemistry* **2006,** *179* (9), 2823-2826.

71. Cameron, A. S.; Friemel, G.; Inosov, D. S., Multipolar phases and magnetically hidden order: review of the heavy-fermion compound $Ce_{1-x}La_xB_6$. *Reports on Progress in Physics* **2016,** *79* (6), 066502.

72. Kuneš, J.; Pickett, W. E., Kondo and anti-Kondo coupling to local moments in EuB_6. *Physical Review B* **2004,** *69* (16), 165111.

73. Cao, J. X.; Zhu, Y.; Yang, Z. Q.; Wu, R. Q., Origin of the magnetism in CaB_6: A first-principles study. *Physical Review B* **2009,** *79* (13), 132404.

74. Mattox, T. M.; Agrawa, A.; Milliron, D. J., Low Temperature Synthesis and Surface Plasmon Resonance of Colloidal Lanthanum Hexaboride (LaB_6) Nanocrystals. *Chemistry of Materials* **2015,** *27* (19), 6620-6624.

75. Yu, Y.; Wang, S.; Li, W.; Chen, Z., Low temperature synthesis of LaB_6 nanoparticles by a molten salt route. *Powder Technology* **2018,** *323*, 203-207.

76. Pan, W. Y.; Bao, Q. W.; Mao, Y. J.; Liu, B. H.; Li, Z. P., Low-temperature synthesis of nanosized metal borides through reaction of lithium borohydride with metal hydroxides or oxides. *Journal of Alloys and Compounds* **2015,** *651*, 666-672.

77. Torabi, O.; Naghibi, S.; Golabgir, M.-H.; Jamshidi, A., Mechanochemical Synthesis of High Crystalline Cerium Hexaboride Nanoparticles from CeO2-B2O3-Mg Ternary System. *Journal of the Chinese Chemical Society* **2016,** *63* (4), 379-384.

78. Zhang, H.; Tang, J.; Zhang, Q.; Zhao, G. P.; Yang, G.; Zhang, J.; Zhou, O.; Qin, L. C., Field emission of electrons from single LaB_6 nanowires. 2006; Vol. 18, pp 87-91.

79. Xu, J.; Zhao, Y.; Zou, C., Self-catalyst growth of LaB_6 nanowires and nanotubes. 2006, p 138.

80. Brewer, J. R.; Deo, N.; Wang, M.; Cheung, C. L., Lanthanum Hexaboride Nanoobelisks. *Chemistry of Materials* **2007,** *19* (26), 6379-6381.

81. Zhang, Q. Y.; Xu, J. Q.; Zhao, Y. M.; Ji, X. H.; Lau, S. P., Fabrication of Large-Scale Single-Crystalline PrB_6 Nanorods and Their Temperature-Dependent Electron Field Emission. 2009, p 742.

82. Xu, J.; Chen, X.; Zhao, Y.; Zou, C.; Ding, Q., Single-crystalline PrB_6 nanowires and their field-emission properties. 2007; Vol. 18.

83. Jash, P.; Nicholls, A. W.; Ruoff, R. S.; Trenary, M., Synthesis and Characterization of Single-Crystal Strontium Hexaboride Nanowires. *Nano Letters* **2008,** *8* (11), 3794-3798.

84. Xu, T.; Zheng, J.-G.; Nicholls, A.; Stankovich, S.; Piner, R.; Ruoff, R., Single-Crystal Calcium Hexaboride Nanowires: Synthesis and Characterization. *Nano Letters* **2004,** *4*.

85. Zhang, M.; Wang, X.; Zhang, X.; Wang, P.; Xiong, S.; Shi, L.; Qian, Y., Direct low-temperature synthesis of RB_6 (R=Ce, Pr, Nd) nanocubes and nanoparticles. *Journal of Solid State Chemistry* **2009,** *182* (11), 3098-3104.

86. Late, D. J.; More, M. A.; Sinha, S.; Dasgupta, K.; Misra, P.; Singh, B. N.; Kukreja, L. M.; Bhoraskar, S. V.; Joag, D. S., Synthesis and characterization of LaB_6 thin films on tungsten, rhenium, silicon and other substrates and their investigations as field emitters. 2011, p 677.

87. Ding, Z.; Bux, S. K.; King, D. J.; Chang, F. L.; Chen, T.-H.; Huang, S.-C.; Kaner, R. B., Lithium intercalation and exfoliation of layered bismuth selenide and bismuth telluride. *Journal of Materials Chemistry* **2009,** *19* (17), 2588-2592.

88. Eda, G.; Yamaguchi, H.; Voiry, D.; Fujita, T.; Chen, M.; Chhowalla, M., Photoluminescence from Chemically Exfoliated MoS_2. *Nano Letters* **2011,** *11* (12), 5111-5116.

89. Ramachandran, R. Nanostructured metal borides and metal fluorides. University of Georgia, Athens, Georgia, 2017.

90. Bi, Z.; Zhang, X.; He, W.; Min, D.; Zhang, W., Recent advances in $LiFePO_4$ nanoparticles with different morphology for high-performance lithium-ion batteries. *RSC Advances* **2013,** *3* (43), 19744-19751.

91. Gong, Z.; Yang, Y., Recent advances in the research of polyanion-type cathode materials for Li-ion batteries. 2011, p 3223.

92. Fisher, C. A. J.; Prieto, V. M. H.; Islam, M. S., Lithium battery materials $LiMPO_4$ (M = Mn, Fe, Co, and Ni): Insights into defect association, transport mechanisms, and doping behavior. 2008; Vol. 20, pp 5907-5915.

93. Wang, J.; Sun, X., Understanding and recent development of carbon coating on $LiFePO_4$ cathode materials for lithium-ion batteries. *Energy & Environmental Science* **2012,** *5* (1), 5163-5185.

94. Ikuhara, Y. H.; Gao, X.; Fisher, C. A. J.; Kuwabara, A.; Moriwake, H.; Kohama, K.; Iba, H.; Ikuhara, Y., Atomic level changes during capacity fade in highly oriented thin films of cathode material $LiCoPO_4$. *Journal of Materials Chemistry A* **2017,** *5* (19), 9329-9338.

95. Rui, X.; Zhao, X.; Lu, Z.; Tan, H.; Sim, D.; Hng, H. H.; Yazami, R.; Lim, T. M.; Yan, Q., Olivine-Type Nanosheets for Lithium Ion Battery Cathodes. *ACS Nano* **2013,** *7* (6), 5637-5646.

96. Gim, J.; Song, J.; Nguyen, D.; Hilmy Alfaruqi, M.; Kim, S.; Kang, J.; Rai, A. K.; Mathew, V.; Kim, J., A two-step solid state synthesis of $LiFePO_4$/C cathode with varying carbon contents for Li-ion batteries. *Ceramics International* **2014,** *40* (1, Part B), 1561-1567.

97. Konishi, S.; Murayama, D.; Itadani, A.; Uematsu, K.; Toda, K.; Sato, M.; Arimitsu, N.; Aoki, T.; Yamaguchi, T., Improvement in Electrochemical Performance of $LiCoPO_4$/C Using Furnace Blacks with High Surface Areas as a Carbon-based Composite Material. *Electrochemistry* **2017,** *85* (10), 643-646.

98. Gangulibabu; Nallathamby, K.; Meyrick, D.; Minakshi, M., Carbonate anion controlled growth of $LiCoPO_4$/C nanorods and its improved electrochemical behavior. *Electrochimica Acta* **2013,** *101*, 18-26.

99. Poovizhi, P. N.; Selladurai, S., Study of pristine and carbon-coated $LiCoPO_4$ olivine material synthesized by modified sol–gel method. *Ionics* **2011,** *17* (1), 13-19.

100. Choi, D.; Kumta, P. N., Surfactant based sol–gel approach to nanostructured $LiFePO_4$ for high rate Li-ion batteries. *Journal of Power Sources* **2007,** *163* (2), 1064-1069.

101. Wang, Y.-M.; Wang, F.; Wang, G.-J., Sol-Gel Synthesis and Electrochemical Performance of $LiMnPO_4$/C Cathode Material. 2013; Vol. 28, pp 415-419.

102. Zhong, S.-k.; Wang, Y.; Liu, J.-q.; Wang, J., Synthesis of $LiMnPO_4$/C composite material for lithium ion batteries by sol-gel method. *Transactions of Nonferrous Metals Society of China* **2012,** *22* (10), 2535-2540.

103. Vadivel Murugan, A.; Muraliganth, T.; Manthiram, A., One-Pot Microwave-Hydrothermal Synthesis and Characterization of Carbon-Coated $LiMPO_4$ (M=Mn, Fe, and Co) Cathodes. *Journal of The Electrochemical Society* **2009,** *156* (2), A79.

104. Wang, J.; Niu, Y.; Fu, Y.; Yang, Y.; Hojamberdiev, M., Urea and Ethylene Glycol-Assisted Solvothermal Synthesis of Spheroidal $LiFePO_4$/C Nanoparticles as a Cathode Material for Lithium-ion Batteries. *ChemistrySelect* **2018,** *3* (19), 5471-5479.

105. Ludwig, J.; Haering, D.; Doeff, M. M.; Nilges, T., Particle size-controllable microwave-assisted solvothermal synthesis of the high-voltage cathode material $LiCoPO_4$ using water/ethylene glycol solvent blends. *Solid State Sciences* **2017,** *65*, 100-109.

106. Zhao, Y.; Wang, S.; Zhao, C.; Xia, D., Synthesis and electrochemical performance of $LiCoPO_4$ micron-rods by dispersant-aided hydrothermal method for lithium ion batteries. *Rare Metals* **2009,** *28* (2), 117-121.

107. Ludwig, J.; Marino, C.; Haering, D.; Stinner, C.; Gasteiger, H. A.; Nilges, T., Morphology-controlled microwave-assisted solvothermal synthesis of high-performance LiCoPO4 as a high-voltage cathode material for Li-ion batteries. *Journal of Power Sources* **2017,** *342*, 214-223.

108. Neher, G. R.; Salguero, T., *Two-dimensional metal phosphate nanomaterials for energy storage applications*. University of Georgia: 2018.

CHAPTER 2

MAGNESIATION AND EXFOLIATION OF LANTHANUM HEXABORIDE

Milkovska, M. and Salguero, T.T. To be submitted to *Chemistry of Materials*

Abstract

Bulk lanthanum hexaboride is converted into nanosheets using a top-down approach. The boride is modified using incorporation of Mg^{2+} into the structure and characterized using powder X-ray diffraction, scanning electron microscopy, energy dispersive spectroscopy, multinuclear solid state nuclear magnetic resonance and Raman spectroscopy. Mg_xLaB_6 is reacted with deionized water to dissemble the boron-metal framework and yield nanostructured material. The product consists of nanosheets with lateral dimensions of approximately 200-500 nm. The nanomaterial is characterized using powder X-ray diffraction and Raman spectroscopy. Additionally, transmission electron microscopy and selected area electron diffraction are utilized to study their morphology and confirm their composition. The characteristics of the final product are studied as a function of reaction time, temperature and additional magnesiation. I compare the results to a similar methodology involving Li^+, revealing that the use of Mg^{2+} could be complementary to Li^+.

Introduction

Metal hexaborides, a subset of the broader class of metal borides, display an array of exciting electronic properties. These features can be attributed to the bonding of the hexaborides, in which the metal atom is confined by a covalently bonded boron network. In such structures, the metal can donate electrons to the electron deficient boron lattice, which makes divalent hexaborides semiconductors and trivalent hexaborides metallic.[1-2]

Within the hexaboride subgroup, lanthanum hexaboride (LaB_6) has been studied comprehensively. Many years of scientific exploration have demonstrated that LaB_6 possesses high melting point (~2210 °C) as well as excellent hardness, electrical conductivity, thermal and chemical stability.[3-4] Furthermore, its high current density (~ 29 A cm^{-2}), low work function and good resistance to poisoning in vacuum make LaB_6 the ideal material for cathodes in many industrial applications, such as electron microscopes, optical coatings, and electron beam welders.[4-6]

Nanostructuring of LaB_6 has been explored previously: nanoparticles,[7] nanoobelisks,[8] nanowires,[9] nanorods[10] have been reported. In part, the nanostructuring of LaB_6 aims to drastically improve its industrial processability, particularly for the formation of uniform coatings. In line with this application, a novel top-down chemical route was developed recently in this group to convert bulk LaB_6 into nanosheets, achieving results beyond sonication and mechanical cleavage.[11] In this method, Li^+ is incorporated into LaB_6 to modify its structure using either a solvated electron system (Li in liquid ammonia) or *n*-butyllithium. The lithiated LaB_6 then reacts with H_2O to exfoliate and generate LaB_6 nanosheets.

In this chapter, I describe a variation of this technique using Mg^{2+} in place of Li^{+}. A comparison between the two chemistries demonstrates the overall versality of the approach and provides further information about the mechanism of ion incorporation.

Experimental

Materials: Lanthanum hexaboride (powder, Office of Naval Research, USA), 1 M di-*n*-butylmagnesium in heptane (Sigma-Aldrich), hexanes (98.5%, Fisher).

Reaction of Lanthanum Hexaboride with Di-*n*-Butylmagnesium: In a typical reaction, 0.204 g of LaB_6 powder (1 mmol) was added to a 30 mL glass vial together with a 12.7x3 mm Teflon stir bar. All of the following steps were completed inside an argon filled glove box with levels of O_2 < 5 ppm and H_2O < 0.1 ppm. After transferring the vial to the glovebox, 3–7 mmol of 1M di-*n*-butylmagnesium in heptane were added using a syringe. The vial was capped with a Teflon lined cap and sealed with Parafilm® M. The reactants were stirred in the glove box for durations ranging from 5 days to 4 weeks. For high temperature reactions, the vial was put in an aluminum bead bath on a hotplate set at 80 °C. After the reaction was finished, the magnesiated material was separated from the excess di-*n*-butylmagnesium using vacuum filtration and washed thoroughly with hexane. The resulting product was scraped off from the filter paper and left to finish drying overnight in a clean vial. Approximately 0.175 g of purple powder was retrieved (85.8% yield).

Exfoliation of Lanthanum Hexaboride in Water: 0.125 g of the magnesiated material was removed from the glovebox and dispersed in 20 mL DI H_2O in a conical centrifuge tube. The mixture was then centrifuged at 10,000 rpm for 30 minutes to separate the hexaboride from the water and any soluble byproducts. After decanting the initial volume of water, another 20 mL of DI water was added to the centrifuge tube and the dispersion was probe sonicated at 50 amplitude for 1 hour. Approximately 100-200 µL of the sonicated dispersion was used to study the material by TEM/SAED. The remaining nanomaterial was dried in a vacuum oven overnight at 40 °C, providing 0.0779 g of exfoliated material (62.3% yield).

Remagnesiation of Lanthanum Hexaboride: The exfoliated LaB_6 powder was used for a second magnesiation reaction. For this reaction, 0.05 g of exfoliated material and 5 mL of di-*n*-butylmagnesium was used. The other conditions of a standard magnesiation reaction at 80 °C remained unchanged. The experiment yielded 0.044 g of material (88% yield).

Control Reaction of Lanthanum Hexaboride with Hexane: 0.204 g (1 mmol) of LaB_6 was put in a 30 mL vial with a Teflon stir bar. In an Argon glovebox, 5 mL of hexane was added, and the vial was capped. After sealing the vial with Parafilm® M, its contents were stirred at room temperature for 4 weeks. Next, the mixture was filtered using vacuum filtration and washed with hexane. The product was left to dry fully overnight in the glovebox.

Characterization: The composition of the bulk, magnesiated and exfoliated materials was confirmed using a Bruker D8-Advance powder X-ray diffractometer (Co-Kα radiation, λ=1.7889 Å) operated at 35 mA and 40 kV. The scans were executed over the 2θ range of 5−70° with a scanning rate of 0.2 sec per step. The morphology and elemental composition of the magnesiated materials were examined using a FEI Teneo field emission gun scanning electron microscope (FEG-SEM) equipped with an Oxford energy dispersive spectroscopy (EDS) system operated at 5-20 keV. SEM sample preparation consisted of depositing the magnesiated powders onto carbon sticky tape. The morphology of the exfoliated nanoproducts were characterized using a FEI Tecnai 20 (200 kV) transmission electron microscope (TEM) in conjunction with selected area electron diffraction (SAED) which was used to confirm the identity of the material. TEM samples were drop cast onto Formvar grids and allowed to dry in ambient conditions. Solid-state NMR data were collected with a Bruker Advance III 400 spectrometer operating at 10 MHz. Raman spectra were collected using a Renishaw InVia Laser spectrometer with a diode laser operating at 785 nm.

Results and Discussion

The study of modification of lanthanum hexaboride started with lithiation reactions that used *n*-butyllithium as the metal ion source. Thus, it is logical to utilize the magnesium equivalent from the same organometallic group. Scientists have previously shown that di-*n*-butylmagnesium was successfully used as the Mg^{2+} source in a variety of solid hosts such as chalcogenides and oxides.[12] It is commercially available as a 1M solution, which makes is relatively straightforward to work with, and the reactant stoichiometries could be easily varied.

Room Temperature Reactions

Bulk lanthanum hexaboride powder was treated with various amounts of 1M di-*n*-butylmagnesium at room temperature and the stoichiometry of the hexaboride: magnesiation reagent was varied from 1:3 to 1:7. This set of early experiments showed that, within the specified range, the stoichiometry between the two reactants didn't influence the morphology of the isolated material and suggested the possibility that a much higher concentration of Mg^{2+} is required to affect exfoliation (e.g., more concentrated di-*n*-butylmagnesium or Mg^{2+} solvated in liquid ammonia). Thus, a 1:5 stoichiometric ratio was chosen to represent a typical reaction at room temperature and was used in all subsequent reactions. Powder X-ray was performed on the magnesiated and exfoliated materials to observe structural changes (Figure 2.1). Overall, both the magnesiated and exfoliated material match the bulk boride and no additional peaks belonging to other species were detected. It is important to note that a second set of peaks to the left (lower 2θ) of the peaks corresponding to LaB_6 are, in fact, an artifact of the diffractometer. This was confirmed with an internal Si standard (Standard Reference Material 640b, National Bureau of Standards). In this control experiment, PXRD on the Si standard showed no additional peaks.

However, once the standard material was added to a LaB_6 sample, its pattern exhibited the second set of peaks as well.

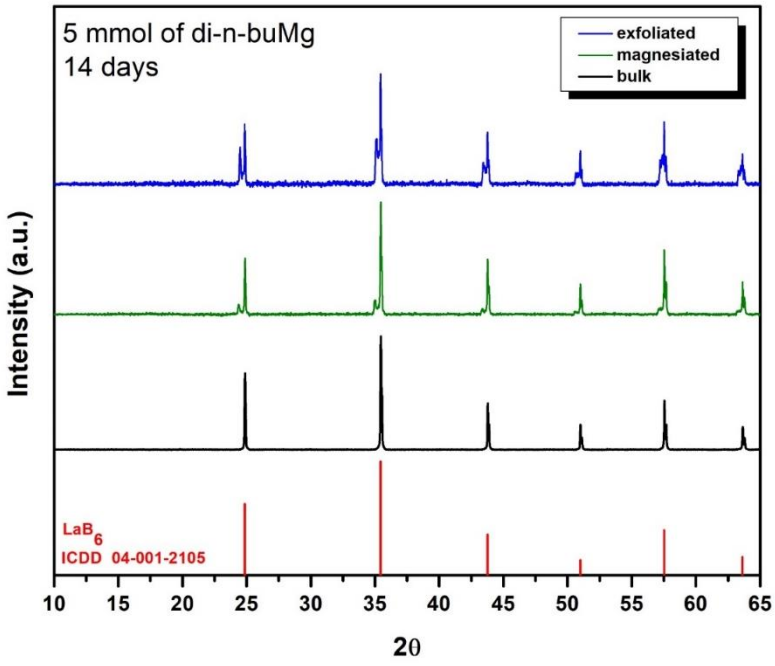

Figure 2.1. PXRD of bulk, magnesiated and exfoliated LaB6 from a 14-day reaction with 1:5 molar ratio of LaB_6: di-*n*-butylmagnesium

SEM-EDS provided information about the morphology and composition of the magnesiated product. A comparison of bulk (Figure 2.2 A) and magnesiated LaB_6 (Figure 2.2 B) established that the crystal morphology and size (approximately 5-15 µm) and overall smooth texture was retained. Similar results were observed for lithiated LaB_6 using similar methodology where no change in morphology was observed as well when the LaB_6 was modified with Li^+.[11] Additionally, elemental mapping provided compositional information for the magnesiated LaB_6 (Fig. 2.2 C-F). La, B, O and Mg were present in the sample. EDS at varying accelerating voltage determined that Mg is not only present on the surface of the samples, but deeper into the hexaboride crystals, indicating that the metal was indeed incorporated into the sample. The presence of oxygen is due the boride's protective oxide coating[13] and potentially the reaction of the incorporated Mg in ambient conditions to form Mg oxides and hydroxides.

Once the magnesiated sample was reacted with H_2O, the products were observed by TEM. The morphologies and brightfield contrast of the product particles (representative example shown in Figure. 2.3) are consistent with platelets, not nanosheets. Therefore, we concluded that different reaction parameters were needed to lead the reaction to completion.

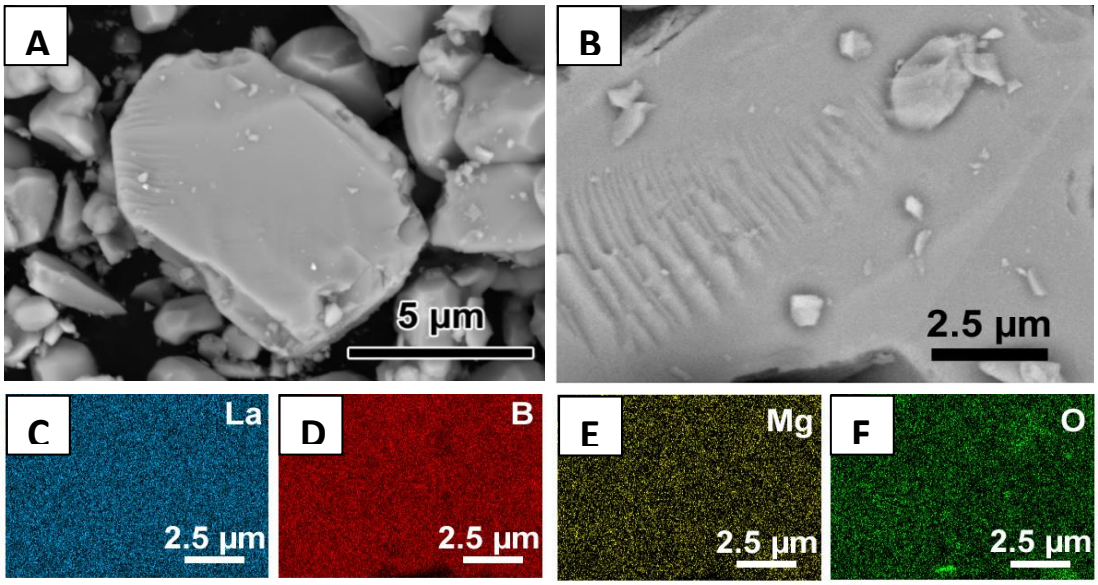

Figure 2.2. SEM image of bulk (A) and magnesiated LaB_6 (B). EDS of magnesiated LaB_6 showing lanthanum (C), boron (D), magnesium (E) and oxygen (F) mapping

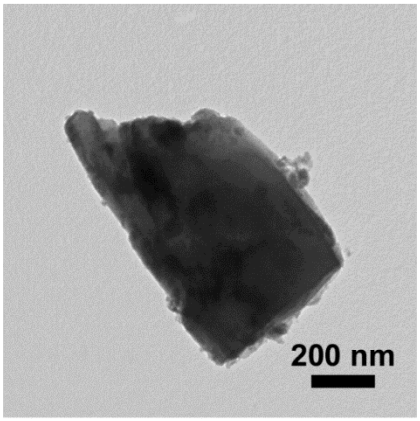

Figure 2.3. TEM of exfoliated LaB_6 at room temperature

Longer reaction times at room temperature were tested in an effort to produce nanosheets. However, both 30-day as well as 90-day reactions did not lead to reaction completion or improved exfoliation. In addition, MgO particles were observed by SEM-EDS in the sample magnesiated for 3 months; as shown in Figure 2.4, the back-scattered SEM image indicates that there are two types of compounds based on the differences in contrast, and elemental mapping reveals areas with significant presence of La/B or Mg/O. This suggests that the di-*n*-butylmagnesium likely has degraded over time to produce highly reactive MgH_2, which forms MgO once exposed to air. The formation of a white precipitate at the end of the reaction (mixed in with the dark purple LaB_6) is consistent with this observation. These results indicated that long reaction times are not the best option to achieve high levels of magnesiation in this system, and thus different reaction parameters should be examined instead.

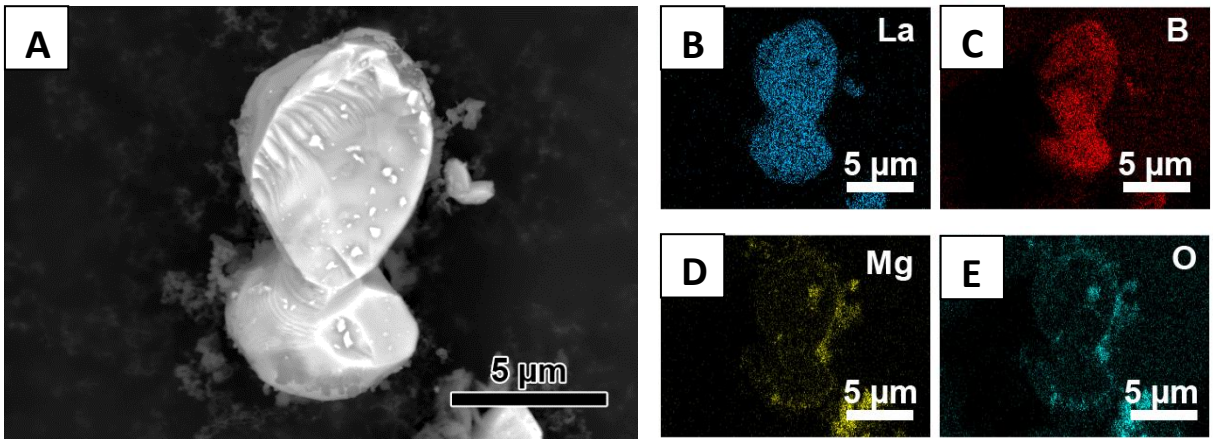

Figure 2.4. SEM of magnesiated LaB_6 at room temperature for 90 days (A) with corresponding EDS (B-E)

Reactions at 80 °C

To explore in the influence of temperature on reaction outcome, I performed a 5-day reaction at 80 °C. The PXRD pattern of the reaction product was similar to that of the room temperature experiment and didn't reveal any new information. SEM-EDS data also appeared similar, with Mg detected in the magnesiated LaB_6. However, TEM imaging showed that the exfoliated product consisted of thinner, more uniform sheets (Figure 2.5A). In fact, the thickness of the sheets was appropriate for SAED to confirm their identity, and the pattern was indexed to the (001) lattice plane of cubic LaB_6 (Figure 2.5B). This result suggested that increasing the reaction temperature led to more complete magnesiation over an expedited time.

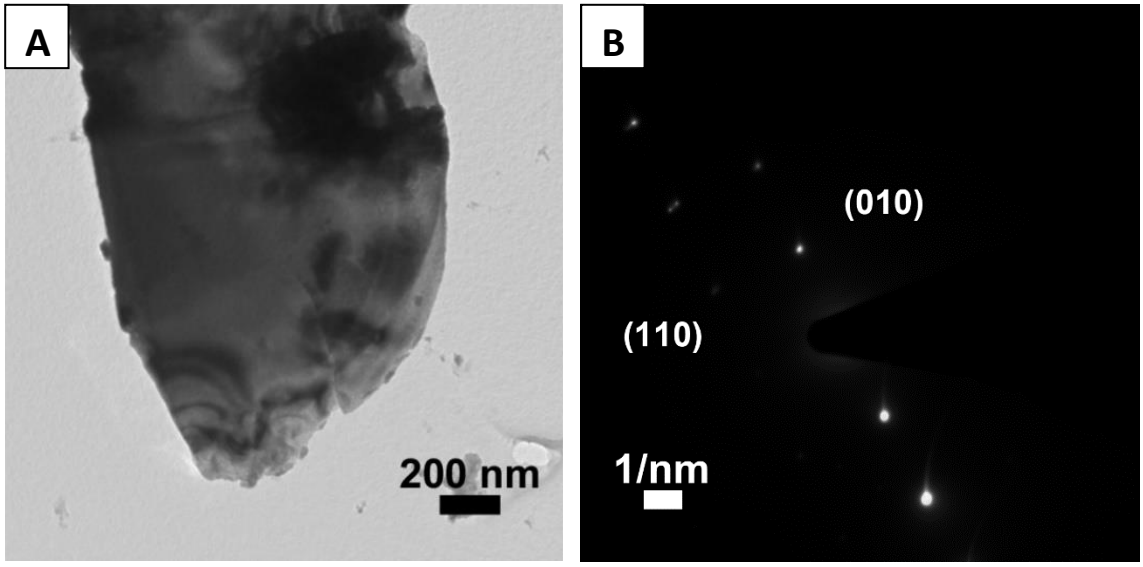

Figure 2.5. TEM of exfoliated LaB_6 from a 5-day reaction at elevated temperature (A) with corresponding SAED pattern (B)

Additional characterization was performed to clarify the nature of the La and B chemical environments and how they are impacted by Mg incorporation and subsequent extraction. First, multinuclear solid-state NMR was performed on the magnesiated sample and compared to that of bulk LaB_6 (Figure 2.6). For ^{11}B NMR, the main isotopic peak shifts from 0.3 to 0.1 ppm which

might be due to slight changes in the boron environment; however, because of the broadness of these peaks and their spinning sidebands, the upfield movement could also be ascribed to statistical error. In the case of ^{139}La NMR, on the other hand, the shift of the main peak is much more prominent: bulk LaB_6 exhibits a sharp peak at –108 ppm whereas the peak for magnesiated LaB_6 occurs at –115 ppm. Such a significant shift indicates that magnesiation causes a definite change in the La environment, and furthermore, this change corroborates that Mg^{2+} does, in fact, become incorporated into the structure. These trends are consistent with those observed for lithiated LaB_6.[11] SSNMR of ^{25}Mg was not performed on the samples as the nucleus is shown to be challenging to study due to sensitivity and resolution problems yielding very broad peaks and requiring high magnetic fields.[14]

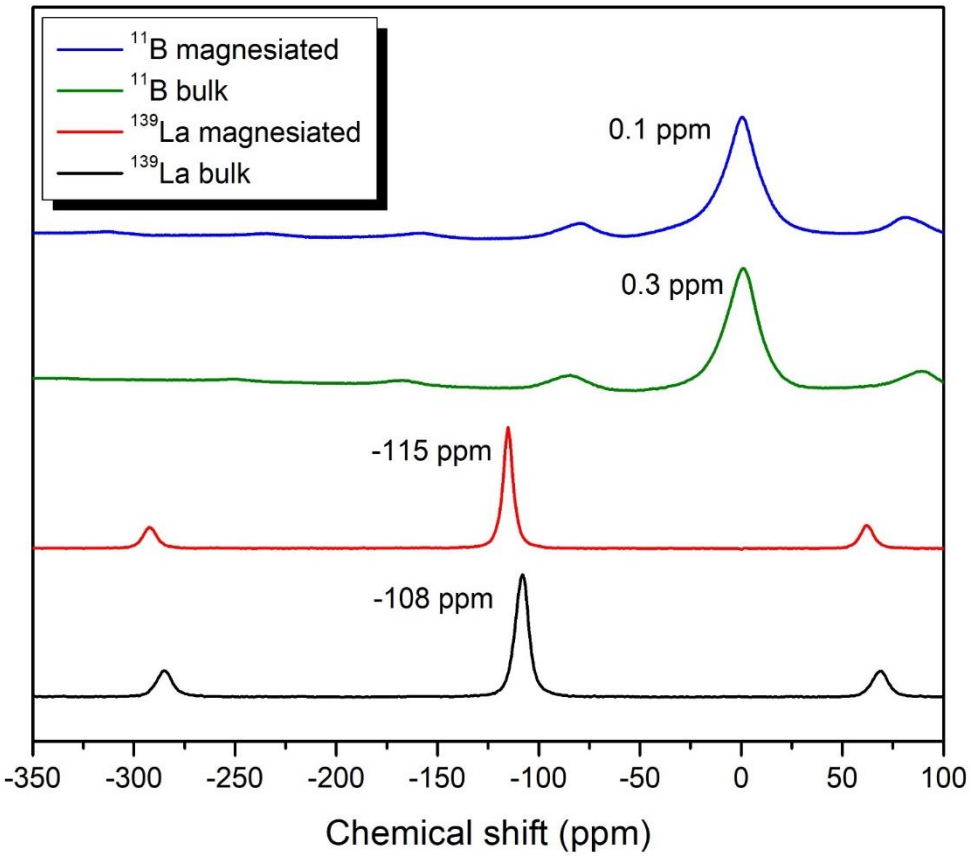

Figure 2.6. ^{11}B and ^{139}La solid state NMR of bulk and magnesiated LaB_6

Raman spectroscopy was used to further characterize changes in LaB_6 structure upon magnesiation; prior work has demonstrated that strain and the introduction of other species into the structure of various materials can lead to shifting of Raman active peaks.[15-17] In particular, a study of LaB_6 nanocrystals demonstrated that defects within the hexaboride structure can have a significant influence on their vibrational properties[18]; specifically, Raman active peaks of LaB_6 became red shifted as the boron content of the nanocrystals decreased. In our study of Mg^{2+} incorporation in LaB_6, Raman spectroscopy was used to survey the chemically modified samples and compare them to bulk. Figure 2.7 shows the Raman spectra of all three samples and Table 2.1 lists the peak positions. The peaks at 111.5 and 205.9 cm^{-1}, corresponding to the lanthanum vibration within the boron cage (rattling mode) or its movement (T_{1u}) respectively, did not change. The peaks at 680.2 cm^{-1} (boron bending vibration, T_{2g}) and 1104.8 and 1255.3 cm^{-1} (stretching vibrations, E_g and A_{1g}), however, experience a shift as the sample is modified with Mg^{2+}, suggesting that the boron content is different in the magnesiated and exfoliated samples compared to bulk LaB_6. Although the variation in peak position is not as great as that reported for LaB_6 nanocrystals (at most 5 cm^{-1} for our materials vs 10 cm^{-1} for the nanocrystals),[18] another important factor is the size of the LaB_6 crystals. In the study of nanocrystals, as the size of the nanoparticles is varied, a shift in Raman active peaks is observed. As our experiments are conducted with bulk powder with varying particle size, our results might be affected.

Table 2.1. Peak position of Raman active peaks for bulk, magnesiated and exfoliated LaB_6

Sample	Raman Shift (cm^{-1})				
bulk LaB_6	111.5	205.9	680.2	1104.8	1255.3
magnesiated LaB_6	111.6	205.8	682.5	1108.3	1258.7
Δ (Raman Shift)	0.1	0.1	2.3	3.5	3.4
exfoliated LaB_6	111.4	205.8	683.5	1110.2	1258.7

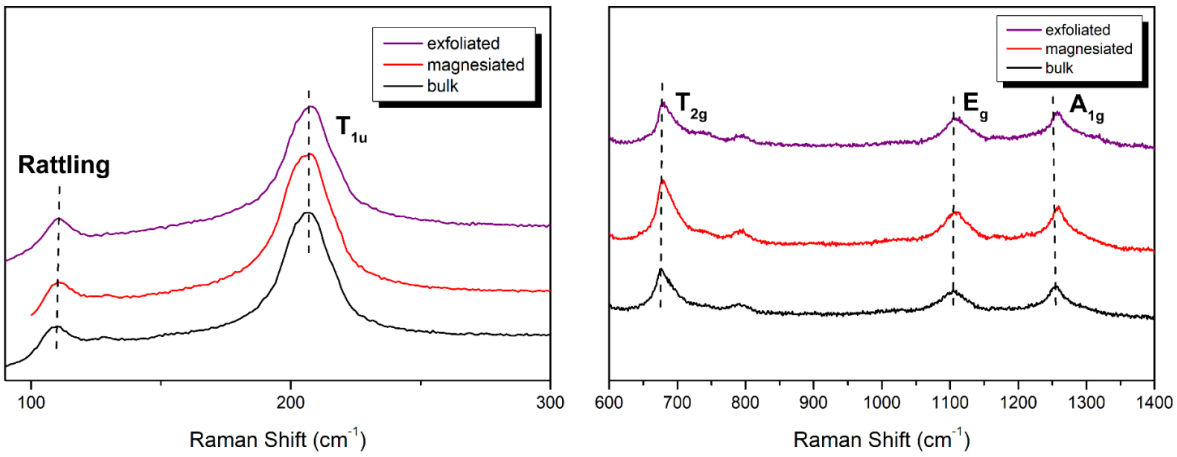

Figure 2.7. Raman spectra of bulk, magnesiated and exfoliated LaB_6

Re-Magnesiation Reactions

To further maximize the extent and effects of LaB_6 magnesiation, I re-magnesiated an exfoliated sample of LaB_6 at 80 °C for 5 days. PXRD of this product sample shows significant peak broadening compared to the bulk LaB_6 (Figure 2.8). This phenomenon could be explained by the incorporation of the Mg^{2+} into the hexaboride lattice, which can introduce significant distortion. Peak broadening was expected with the successful incorporation of sufficient Mg^{2+}

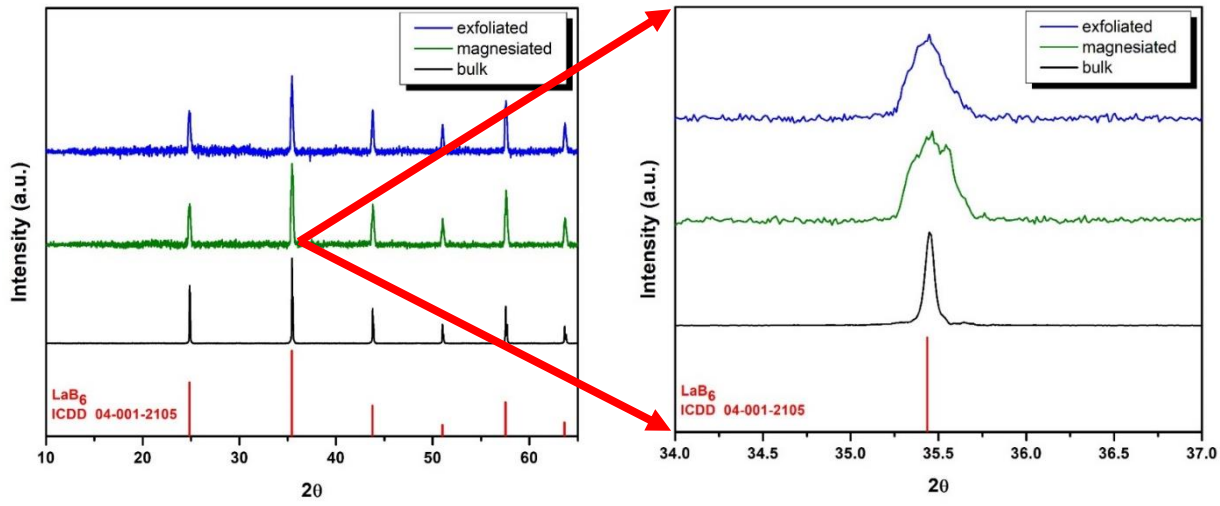

Figure 2.8. PXRD of bulk, re-magnesiated and exfoliated LaB_6

and was observed in LaB_6 lithiation experiments.[11] The PXRD pattern of re-magnesiated and exfoliated LaB_6 retains broadened peaks, whereas lithiated LaB_6 exhibits broadened peaks but exfoliated LaB_6 does not (becoming sharp again). We conclude that the extent of structural modification during magnesiation is significant enough to permanently alter the hexaboride lattice.

Electron microscopy methods were applied to study the re-magnesiated and re-exfoliated materials. SEM of the re-magnesiated LaB_6 revealed the presence of micron-sized hexaboride crystals as well some nanomaterial, which was due to the fact that the material was already magnesiated and exfoliated once prior this this experiment (Figure 2.9 A). Once the material was exfoliated with DI H_2O for a second time, TEM showed that the final morphology was 200-500 nm sized nanosheets that appeared thin and uniform based on the contrast (Figure 2.9 B). Their identity was confirmed by SAED where a polycrystalline diffraction pattern was observed due to the stacking of multiple sheets. The diffraction rings were indexed to the (112) and (011) crystal planes of LaB_6.

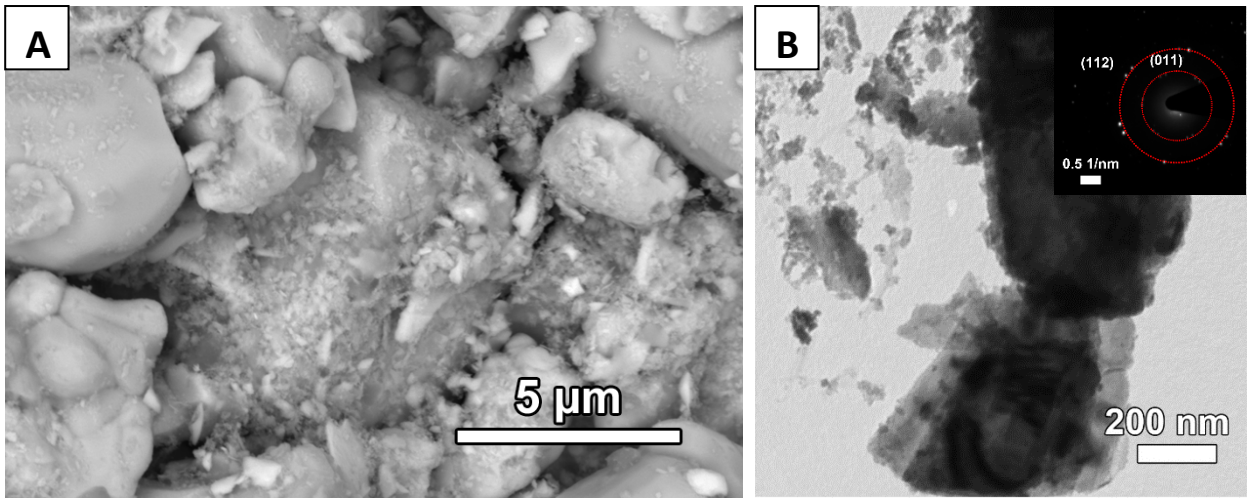

Figure 2.9. SEM of re-magnesiated (A) and exfoliated (B) LaB_6 with corresponding SAED

Control Reaction

The control reaction helped confirm that any nanosheet formation was due to the intended chemistry, as opposed to mechanical exfoliation from agitation for prolonged times. Bulk LaB_6 was stirred for 4 weeks in hexane and underwent the typical work-up involved in a standard magnesiation reaction – vacuum filtration, wash with hexane, addition of DI water, centrifugation, redispersion in DI water and probe sonication for 1 hour at 50 amplitude. PXRD (Figure 2.10) confirmed that no change in structure occurred and TEM showed the presence of uneven, thick crystals (Figure 2.11), likely due to the sonication-induced fragmentation. No nanosheets were observed in the recovered material.

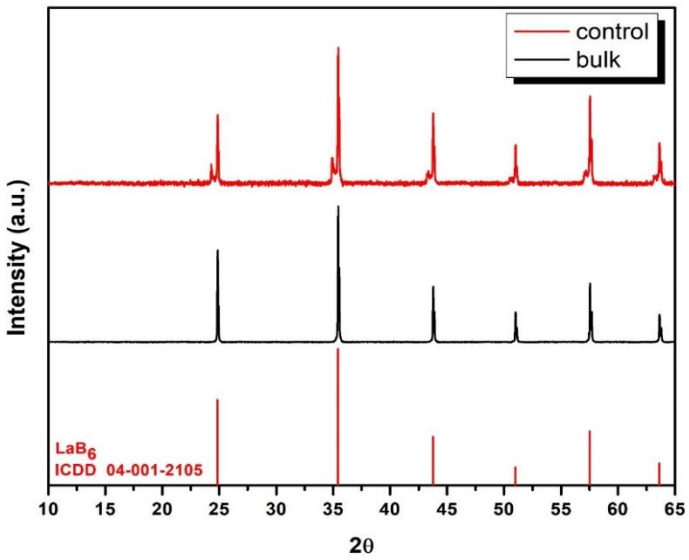

Figure 2.10. PXRD of bulk LaB_6 and control reaction

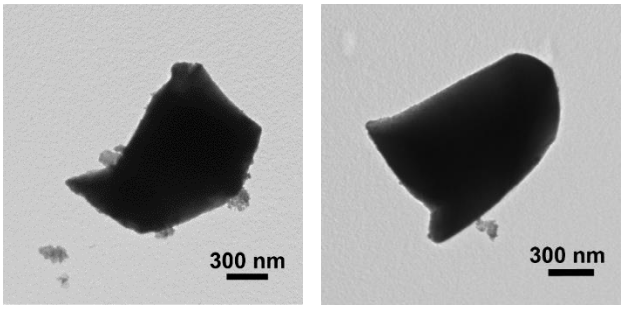

Figure 2.11 TEM of LaB_6 from control reaction

Conclusion

Lanthanum hexaboride was magnesiated using di-*n*-butylmagnesium and the resulting material was exfoliated using DI H_2O. The effects of time, temperature and re-magnesiation were investigated to study the modification of the boride species, compare it to known lithiation techniques, and ultimately find the optimum conditions to produce nanosheets. We discovered that Mg^{2+} is incorporated into LaB_6 crystal structure at both room and elevated temperatures. During the magnesiation process a change in La environment was demonstrated by solid state NMR, but unlike with lithiation methods of LaB_6 where Li-B species was observed, no evidence was found of the formation of Mg-B compounds of any kind. Our results also differ from what was previously observed with SrB_6, i.e., nanoparticles were formed instead of nanosheets and the presence of Li_2B_6 was confirmed.[19]

The exfoliation of LaB_6 was more successful using material magnesiated at higher temperature for shorter duration than material magnesiated for longer times at room temperature. Ultimately, the re-magnesiation method produced the most uniform nanosheets. These results suggest that we were successful in forming the desired nanosheet product but the use di-*n*-butylmagnesium is somewhat limited due to its low concentration or other factors. It seems that alternative magnesiation techniques should be developed to avoid the need for multiple magnesiation cycles.

The successful magnesiation and exfoliation of LaB_6 opens a new chapter in the chemistry involving direct modification of metal hexaborides. It constitutes additional proof that the metal ion incorporation methodology can be expanded to multiple metal ion species. This can be particularly useful as magnesium species are often easier to work with than lithium reagents, which is an important consideration for commercial applications of this chemistry.

References

1. Lafferty, J. M., Boride Cathodes. *Journal of Applied Physics* **1951,** *22* (3), 299-309.

2. Etourneau, J.; Mercurio, J.-P.; Hagenmuller, P., Compounds Based on Octahedral B_6 Units: Hexaborides and Tetraborides. In *Boron and Refractory Borides*, Matkovich, V. I., Ed. Springer Berlin Heidelberg: Berlin, Heidelberg, 1977; pp 115-138.

3. Ivashchenko, V. I.; Turchi, P. E. A.; Shevchenko, V. I.; Medukh, N. R.; Leszczynski, J.; Gorb, L., Electronic, Thermodynamics and Mechanical Properties of LaB_6 from First Principles. *Physica B: Condensed Matter* **2018,** *531*, 216-222.

4. Bao, K.; Liu, C.; Damavandi, B. Y.; Zhang, S., Low-Temperature Preparation of Lanthanum Hexaboride Fine Powder via Magnesiothermic Reduction in Molten Salt. *Journal of Ceramic Science and Technology* **2016,** *7*, 403-408.

5. Buckingham, J. D., Thermionic Emission Properties of a Lanthanum Hexaboride/Rhenium Cathode. *British Journal of Applied Physics* **1965,** *16*, 1821.

6. Goebela, D. M.; Watkins, R. M., Compact Lanthanum Hexaboride Hollow Cathode. *Review of Scientific Instruments* **2010,** *81*, 083504.

7. Mattox, T. M.; Agrawa, A.; Milliron, D. J., Low Temperature Synthesis and Surface Plasmon Resonance of Colloidal Lanthanum Hexaboride (LaB_6) Nanocrystals. *Chemistry of Materials* **2015,** *27* (19), 6620-6624.

8. Brewer, J. R.; Deo, N.; Wang, M.; Cheung, C. L., Lanthanum Hexaboride Nanoobelisks. *Chemistry of Materials* **2007,** *19* (26), 6379-6381.

9. Zhang, H.; Tang, J.; Yuan, J.; Ma, J.; Shinya, N.; Nakajima, K.; Murakami, H.; Ohkubo, T.; Qin, L.-C., Nanostructured LaB_6 Field Emitter with Lowest Apical Work Function. *Nano Letters* **2010,** *10* (9), 3539-3544.

10. Jhaa, M.; Patrab, R.; Ghoshb, S.; Ganguli, A. K., Vertically Aligned Nanorods of Lanthanum Hexaboride with Efficient Field Emission Properties. *Solid State Communications* **2013,** *153* (1), 35-39.

11. Ramachandran, R. Nanostructured Metal borides and Metal Fluorides. University of Georgia, Athens, Georgia, 2017.

12. Bruce, P. G.; Krok, F.; Nowinski, J.; Gibson, V. C.; Tavakkoli, K., Chemical Intercalation of Magnesium into Solid Hosts 1991; Vol. 1, pp 705-706.

13. Jacobson, N. S.; Opila, E. J., Oxidation and Corrosion of Non-oxide Ceramics. In *Reference Module in Materials Science and Materials Engineering*, Elsevier Inc.: 2015.

14. Pallister, P. J.; Moudrakovski, I. L.; Ripmeester, J. A., Mg-25 Ultra-High Field Solid State NMR Spectroscopy and First Principles Calculations of Magnesium Compounds. *Physical Chemistry Chemical Physics* **2009,** *11* (48), 11487-11500.

15. Mueller, N. S.; Heeg, S.; Alvarez, M. P.; Kusch, P.; Wasserroth, S.; Clark, N.; Schedin, F.; Parthenios, J.; Papagelis, K.; Galiotis, C., Evaluating Arbitrary Strain Configurations and Doping in Graphene with Raman Spectroscopy. *2D Materials* **2017,** *5* (1).

16. Das, A.; Pisana, S.; Chakraborty, B.; Piscanec, S.; Saha, S. K.; Waghmare, U. V.; Novoselov, K. S.; Krishnamurthy, H. R.; Geim, A. K.; Ferrari, A. C.; Sood, A. K., Monitoring dopants by Raman Scattering in An Electrochemically Top-Gated Graphene Transistor. *Nature Nanotechnology* **2008,** *3*, 210-215.

17. Urena-Begara, F.; Vayrette, R.; Bhaskar, U. K.; Raskin, J.-P., Raman Analysis of Strain in P-Type Doped Silicon Nanostructure. *Journal of Applied Physics* **2018,** *124*, 095102.

18. Groome, C.; Roh, I.; Mattox, T. M.; Urban, J. J., Effects of Size and Structural Defects on the Vibrational Properties of Lanthanum Hexaboride Nanocrystals. *ACS Omega* **2017,** *2* (5), 2248-2254.

19. Ramachandran, R.; Salguero, T. T., Nanostructuring of Strontium Hexaboride via Lithiation. *Inorganic Chemistry* **2018,** *57* (1), 4-7.

CHAPTER 3

MAGNESIATION AND EXFOLIATION OF CALCIUM HEXABORIDE

Milkovska, M. and Salguero, T.T. To be submitted to *Chemistry of Materials*

Abstract

Calcium hexaboride bulk powder is modified with di-*n*-butylmagnesium and then exfoliated with water or iodomethane to produce nanosheets. The effects of bulk particle size, reaction time and reaction temperature are studied to determine their effect on both the magnesiated and the exfoliated products. The presence of Mg as well as the morphology of the modified hexaboride are examined via SEM-EDS, while PXRD is used to monitor for any changes in the boride crystal structure. Once exfoliated, the nanoproducts are investigated by TEM and STEM to determine their morphology. AFM is used to establish the thickness of the nanosheets. We compare these results to those from Li^+ incorporation techniques and conclude that using Mg^{2+} as the incorporating ion produces the target nanomaterial much faster. Additionally, we demonstrate results of the potential presence of a Mg-B species, which indicates that the magnesiation and lithiation methodologies involve similar boride modification chemistry.

Introduction

Divalent alkaline-earth hexaborides, i.e. CaB_6, SrB_6 and BaB_6, are known for their high melting points and hardness, low thermal expansion coefficient and overall superior chemical stability.[1-2] They also have been studied due to their electric and thermoemissive properties[3] and more recently due to their ferromagnetism[4] and optical properties.[5] Because of these features, the group II hexaborides have found various potential applications in high temperature insulation[1] and power generation,[6] as cathode matherials[5] and wear-resistant materials.[7]

CaB_6 is a semiconductor from the alkaline-earth hexaboride group that has been mostly used as a deoxidant, neutron absorbent and wear-resistant material.[2, 7] As with other borides, nanostructuring of CaB_6 has been achieved in various morphologies; for example, nanowires[8] and nanoparticles[9] have been reported previously. Additionally, the first steps towards making nanosheets of CaB_6 have been successfully executed using Li^+ incorporation techniques.[10] The reaction times of those experiments, however, span months to obtained the desired <10 nm nanosheet morphology. Here we test a modification of the metal incorporation method to increase the efficient production of CaB_6 nanosheets.

In this work, we use a two-step, top down methodology with a Mg^{2+} incorporation reaction followed by an exfoliation step. In using Mg^{2+} instead of Li^+, we hypothesize that having a metal ion of the same group as the metal in the hexaboride potentially could aid its incorporation and subsequently produce more nanosheets with shorter reaction times. In addition, we aim to explore the influence of non-aqueous exfoliation techniques and how they compare to the already established aqueous exfoliation protocol. Finally, we seek to gain further understanding of the metal boride modification chemistry.

Experimental

Materials: Calcium hexaboride (powder, Office of Naval Research, USA), 1 M di-*n*-butylmagnesium in heptane (Sigma-Aldrich), iodomethane (purum, ≥99.0%, Sigma-Aldrich), hexanes (98.5%, Fisher).

Reaction of Calcium Hexaboride with Di-*n*-Butylmagnesium: In a typical reaction, 0.210 g of CaB_6 (2 mmol) was added to a glass vial followed by a Teflon stir bar and the vial was transferred to an argon filled glovebox with levels of O_2 < 5 ppm and H_2O < 0.1 ppm. For reactions in which ground boride was used, the CaB_6 was ground in an agate mortar and pestle for 30 minutes before adding to the vial. Next, 5 mmol of 1 M di-*n*-butylmagnesium in heptane was added to the vial using a syringe and the vial was capped with a Teflon lined cap and sealed with Parafilm® M. The mixture was stirred in the glovebox for 1-4 weeks. For high temperature reaction, the vial was put in an aluminum bead bath on a hotplate at 80 °C. After the reaction was completed, the magnesiated CaB_6 was isolated from the excess magnesiation reagent via vacuum filtration and washed thoroughly with hexane. The product was scraped from the filter paper and left to finish drying overnight in a clean vial. 0.189 g of magnesiated material was retrieved (90% yield).

Exfoliation of Calcium Hexaboride in Water: For the aqueous exfoliation method, 0.09 g of magnesiated CaB_6 was removed from the glovebox and added to a conical centrifuge tube. Next, 20 mL of DI water was transferred into the tube and the dispersion was centrifuged at 10,000 rpm for 30 minutes. Once the hexaboride was separated from the water and any soluble byproducts, the solvent was decanted and another 20 mL of it were added. The mixture was probe sonicated at 50 amplitude for 1 hour. Approximately 100-200 µL of the dispersion was

used to examine the nanoproduct via TEM/SAED. The remaining hexaboride was dried under vacuum overnight at 40 °C. 0.078 g of exfoliated material was recovered (87% yield).

Exfoliation of Calcium Hexaboride in Iodomethane: To exfoliate CaB_6 in non-aqueous conditions, 0.09 g of CaB_6 was transferred to a conical centrifuge tube. Next, 10 mL of iodomethane was added and the tube was capped and sealed with Parafilm® M. The container was then removed from the glovebox and centrifuged for 30 minutes at 10,000 rpm. The material was brought back into the glovebox and the iodomethane was decanted. Next, 15 mL of hexane was added to remove any leftover iodomethane. The tube was resealed and centrifuged under the same conditions as the iodomethane mixture. The solid material was separated from the hexane and the washing process was repeated 2 more times. After the final wash, another 15 mL of hexane was poured into the centrifuge tube and after capping it and sealing it with Parafilm once again, the CaB_6 was bath sonicated for 2 hours. Approximately 100-200 µL of the mixture was used to examine the nanoproduct via TEM/SAED and the rest was left suspended in hexane in the glovebox.

Control Reaction: In a control reaction, 0.210 g of CaB_6 (2 mmol) was added together with a stir bar into a vial. Next, in an argon filled glovebox, 5 mL of hexane were transferred into the vial and the vial was capped and sealed with Parafilm Parafilm® M. The reaction was left stirring for 4 weeks, after which the hexaboride was separated from the hexane via vacuum filtration and washed with excess hexane. The material was left in the glovebox to dry overnight.

Characterization: The composition of the bulk, magnesiated and exfoliated materials was confirmed using a Bruker D8-Advance powder X-ray diffractometer (Co-Kα radiation, λ=1.7889 Å) operated at 35 mA and 40 kV. The scans were performed with a scanning rate of 0.2 sec per step over the 2θ range of 5−70°. The morphology and elemental composition of the

magnesiated materials were examined using a FEI Teneo field emission gun scanning electron microscope (FEG-SEM) in conjunction with an Oxford energy dispersive spectroscopy (EDS) system operated at 5-20 keV. SEM sample preparation consisted of depositing the magnesiated powders onto carbon sticky tape. Scanning transmission electron microscopy (STEM) at 30kV was performed on the same instrument to examine the morphology of the exfoliated nanoproducts. Additional characterization was executed using a FEI Tecnai 20 (200 kV) transmission electron microscope (TEM) equipped with selected area electron diffraction (SAED) in order to confirm the identity of the nanomaterial. STEM/TEM samples were drop cast onto Formvar grids and allowed to dry in ambient conditions for the samples exfoliated in water and in inert conditions for samples exfoliated in iodomethane. To determine the thickness of the nanosheets atomic force microscopy (AFM) on a Bruker Dimension Icon with ScanAsyst in tapping mode was utilized and the AFM data was analyzed using Nanoscope Analysis Software. AFM samples were prepared by dipping a clean Si wafer into a dilute dispersion of nanosheets in water.

Results and Discussion

In these experiments, CaB_6 was modified using di-*n*-butylmagnesium and then reacted with DI H_2O or iodomethane (aqueous vs. non-aqueous exfoliation respectively). First, a time study between 1 and 4 weeks was conducted to determine the influence of reaction time on the magnesiated and exfoliated products. Next, we explored reduction of bulk particle size in order to increase surface area and ultimately achieve higher level of magnesiation and exfoliation. Reactions at elevated temperature were examined with respect to total reaction times. Exfoliation media were varied to explore the versatility of the method, particularly for potential application to borides susceptible to oxidation in aqueous conditions.

Time Study

A time study documented the progress of the magnesiation/exfoliation reactions. Magnesiation reaction time was varied between 1 and 4 weeks and PXRD, SEM-EDS and STEM were performed to characterize the products of each step. All four magnesiation reactions yielded CaB_6 with similar morphology to that of the bulk: crystals with lateral dimensions 10-50 μm and a smooth surface (Figure 3.1 A-D). Corresponding EDS showed the presence of Ca and B as expected. Additionally, Mg was present evenly throughout the material and EDS at 20 kV confirmed that its incorporation was successful. Oxygen, which is typically present in the bulk, can be observed evenly on the surface of the hexaboride and in some concentrated areas, suggesting the incorporated Mg might have started forming oxide/hydroxide species once removed from the glovebox and exposed to atmospheric conditions.

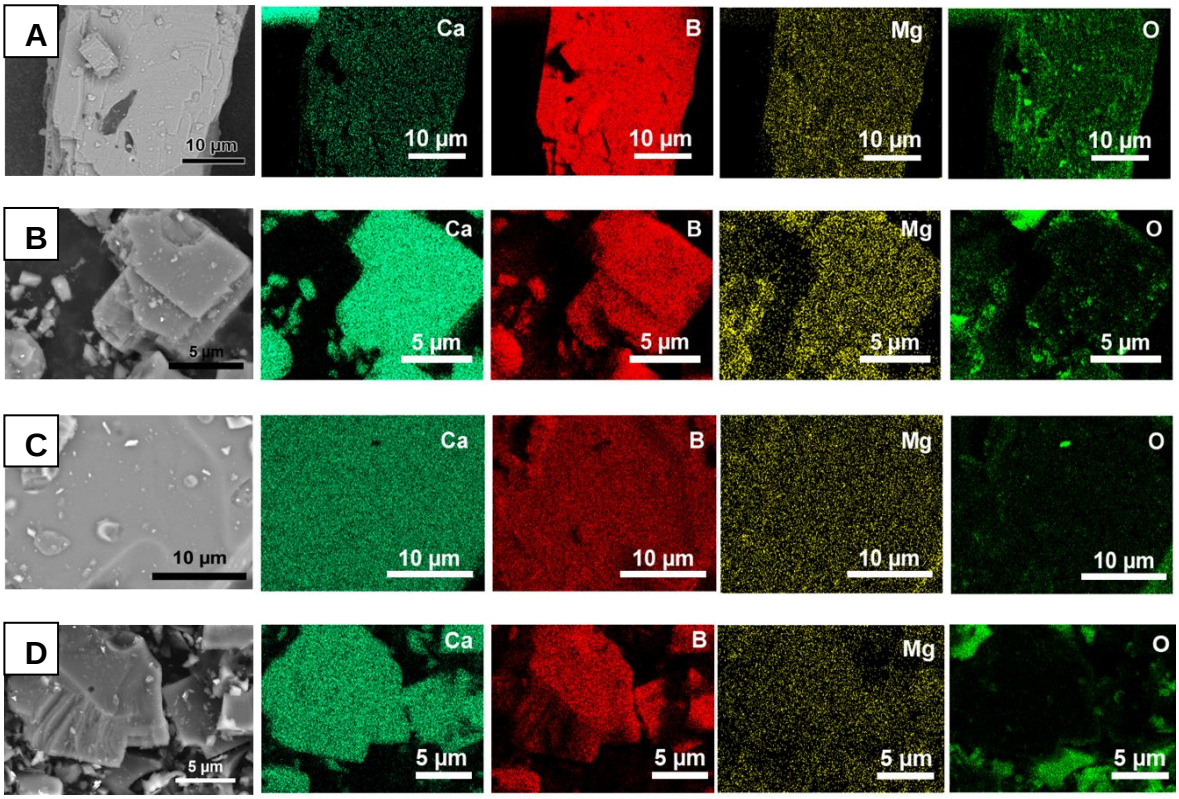

Figure 3.1. SEM of 1 (A), 2 (B), 3 (C) and 4-week (D) reaction with corresponding Ca, B, Mg and O elemental mapping

Powder XRD showed some interesting features. 1- to 3-week reactions yielded diffraction patterns matching to that of bulk CaB_6, but the 4-week reaction showed two additional peaks at ~21 and 53 2θ in magnesiated material and exfoliated products (using both aqueous and non-aqueous conditions) (Figure 3.2). Previous work with the lithiation of CaB_6 revealed the potential formation of LiB_9, and the two peaks observed here have a similar position.[10] An equivalent "MgB_9" compound is not known and other Mg-B species do not appear to match the observed new peaks, but we propose that MgB_9 could form under these conditions (albeit be unstable). Other common byproducts, such as MgO and $Mg(OH)_2$, were ruled out as potential matches.

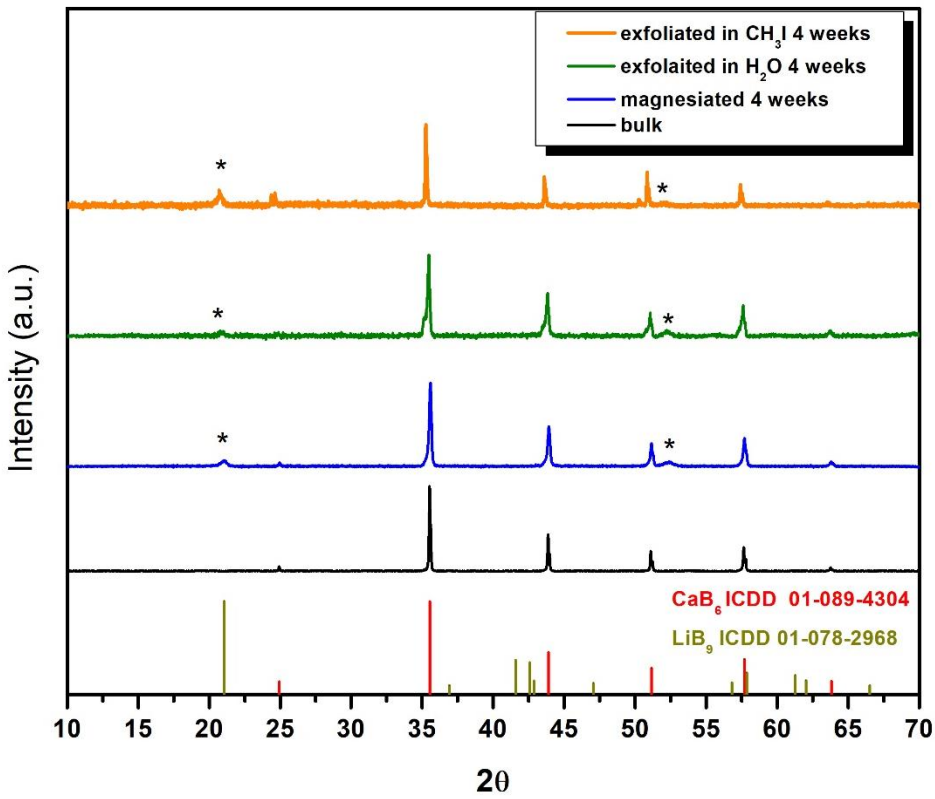

Figure 3.2. PXRD of bulk, magnesiated, exfoliated in H_2O and in iodomethane CaB_6 from a 4-week reaction. Asterisks denote the presence of additional species.

Once the magnesiated materials were exfoliated, TEM and STEM-EDS were performed to observe their morphology and composition. The 1-week reaction showed some uneven crystals with jagged edges, most likely due to the sonication process rather than successful exfoliation (Figure. 3.3A). This result indicated that longer reaction times were required to achieve the desired nanomorphology. As reaction time was increased, the nanoproduct appeared to become thinner and more uniform based on the bright field contrast of the respective imaging technique. Finally, at 4 weeks, nanoplatelets were observed in both the aqueous and non-aqueous exfoliation media. Their elemental mapping showed the presences of both Ca and B, consistent with calcium boride (Figure 3.3 B and C insets). With these results, we conclude that increasing the reaction time had a significant effect on the final product that was much more noticeable than in the magnesiation/exfoliation of LaB_6 (See Chapter 2). More importantly, the morphology

appeared to be comparable to that produced using lithiation techniques, signaling that changing the metal ion is a viable alternative in the modification of CaB_6. Finally, both aqueous and non-aqueous exfoliation media yielded similar nanoproducts, verifying that solvents other than water could be used for the exfoliation step if needed.

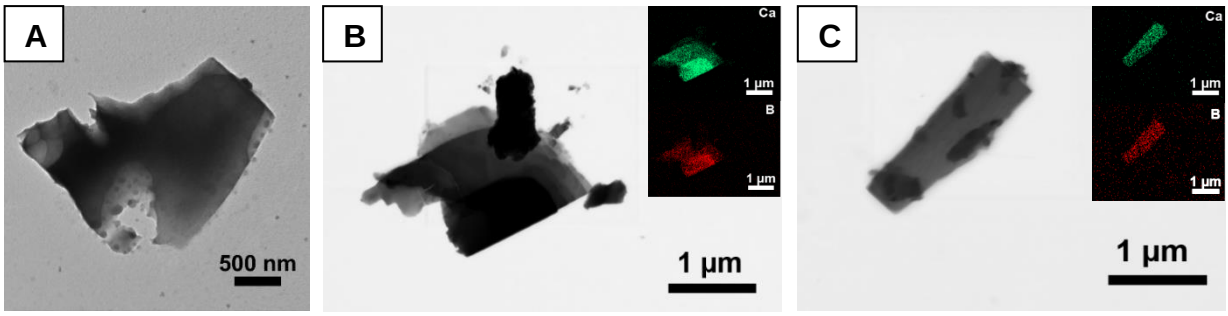

Figure 3.3. TEM of CaB_6 exfoliated in H_2O from a 1-week reaction (A). STEM of CaB_6 from a 4-week reaction exfoliated in H_2O (B) and in CH_3I (C) with corresponding EDS (insets).

Reducing Bulk Particle Size

In an effort to increase the surface area of the CaB_6 crystals, mortar and pestle grinding was utilized to decrease the bulk particles size. After grinding the bulk for 30 minutes, SEM was performed to evaluate the size of the hexaboride particles. Before the grinding process, the majority of the crystals had lateral dimensions 30-50 µm with some smaller ones around 10 µm (Figure 3.4 A). Following grinding, the majority of the crystals were 10-20 µm (Figure 3.4 B), with little change in overall morphology.

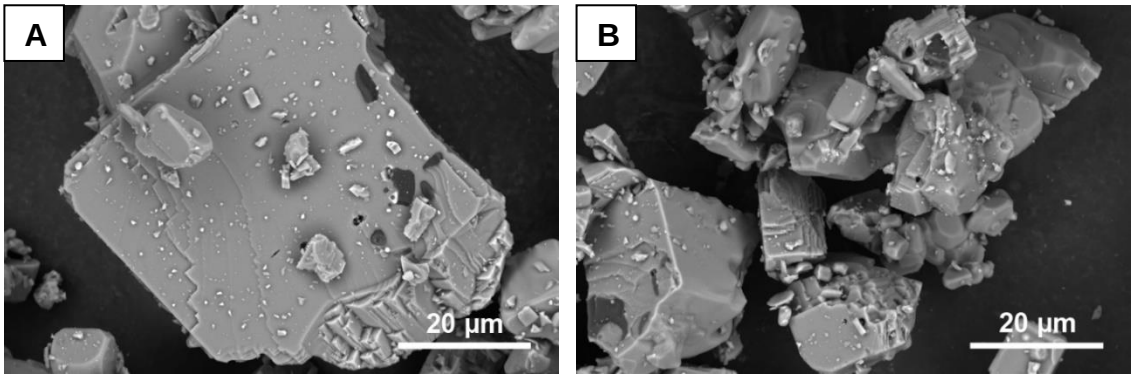

Figure 3.4. SEM of bulk CaB_6 (A) and ground bulk CaB_6

After successfully reducing the bulk particle size, magnesiation reactions were performed to evaluate its effect on the final nanoproduct. A 2-week reaction at room temperature was compared to that of the same reaction without the grinding step. PXRD showed no observable changes between bulk, magnesiated and exfoliated (similarly to the non-ground reaction). SEM-EDS was performed to evaluate the magnesiated material. The crystals appeared to have retained their morphology, and the layered nature of CaB_6 was visible at the fractured edges of most particles (Figure 3.5 A). Further, elemental mapping showed the presence of all expected elements: Ca, B, Mg and O (Figure 3.5 B-E). It's interesting to note that while magnesium was found evenly distributed onto the surface of crystals, there appear to be some more concentrated areas at the edges as demonstrated by the darker yellow color on the left side of the Mg mapping (Figure 3.5 D). This suggests that those are the areas where the magnesium ions get incorporated to a higher extent which would aid the delamination process significantly.

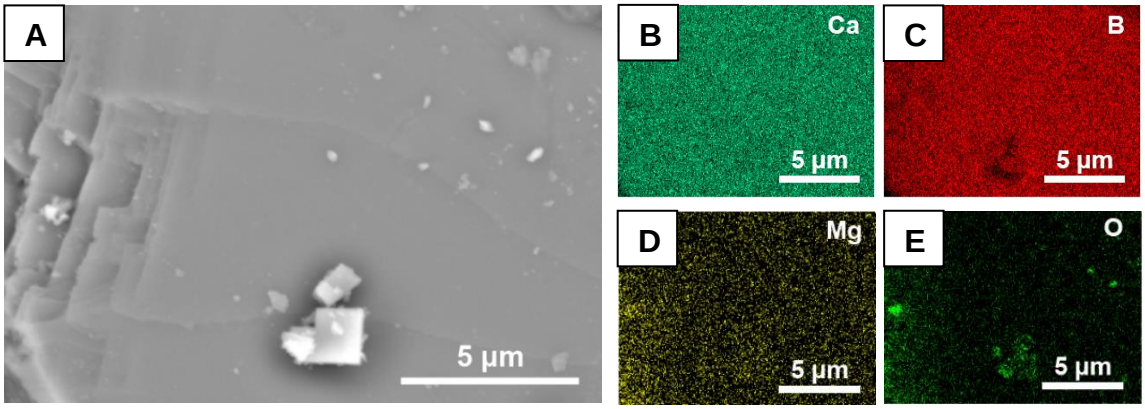

Figure 3.5. SEM of magnesiated CaB_6 from 2-week reaction after bulk particle size reduction (A) with corresponding elemental mapping (B-E)

Aqueous exfoliation of this magnesiated product yielded uniform nanosheets with straight edges and lateral dimensions of ~500-600 nm, as observed by TEM (Figure 3.6). Their SAED showed the cubic diffraction pattern along the (001) plane with d-spacings indexed to CaB_6 (Figure 3.6 A inset). Some nanoparticles, whose SAED was indexed to CaB6, were also formed (Figure 3.6B), suggesting that the grinding step requires optimization. For example, planetary ball milling could be used in future experiments because the applied force can be better controlled and reproduced. These results contrasted with those from the 2-week reaction performed without CaB_6 grinding; here much thicker nanomorphologies were observed, confirming the need for particle size reduction.

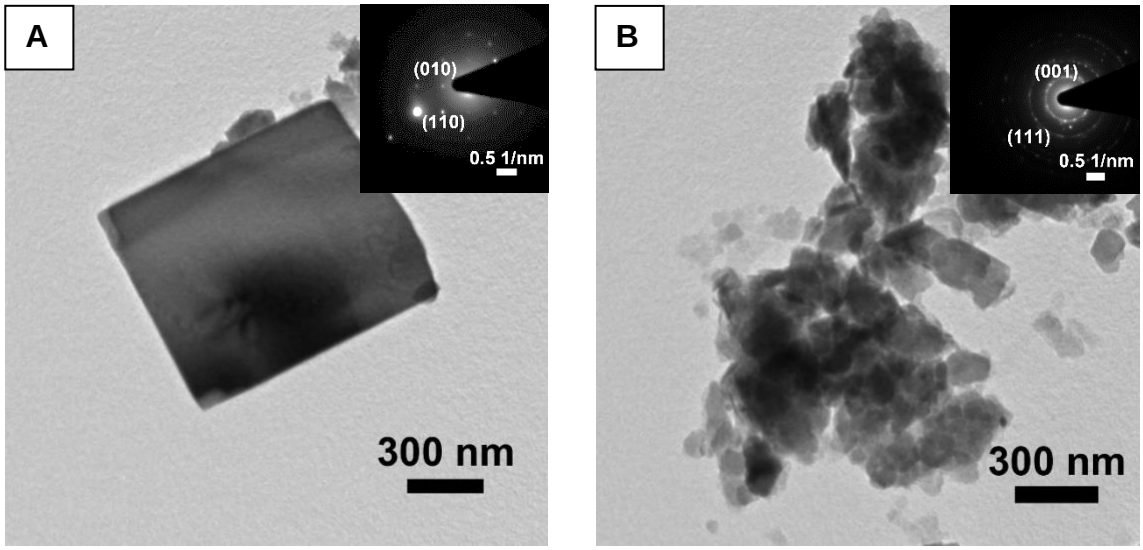

Figure 3.6. TEM of exfoliated CaB_6 from 2-week reaction after bulk particle size reduction showing nanosheets (A) and nanoparticles (B)

Longer reaction times of one and three months also were evaluated with ground CaB_6. While studying the 1-month reaction, we determined that the PXRD patterns of both magnesiated and aqueous exfoliated products fit the expected CaB_6 pattern, and similarly to the reaction with un-ground hexaboride, the patterns displayed the 2 extra peaks at ~21 and 53 2θ. This result confirms that this new species forms only during experiments with reaction times ≥ 1 month. Once the material was exfoliated, nanosheets of similar morphology to the 2-week reaction were observed, indicating that reaction times longer than 2 weeks don't necessarily yield much improved results. AFM of the nanoproduct showed that the sheets were ~15 nm in thickness, which corresponds to approximately 35 monolayers of CaB_6 plus surface hydration layers (Figure 3.7).

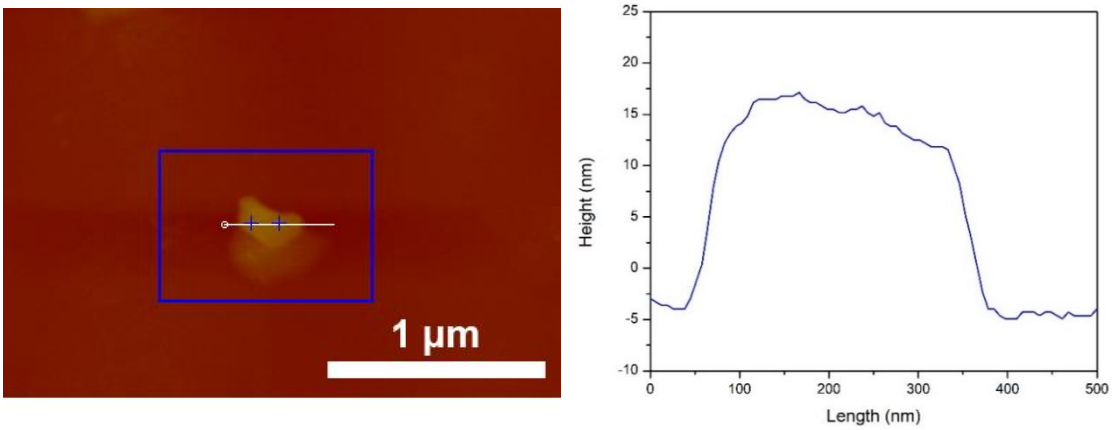

Figure 3.7. AFM image of exfoliated CaB_6 with the corresponding height profile

The longest magnesiation reaction allowed CaB_6 to stir with di-*n*-butylmagnesium for 3 months. The purpose of this experiment was to maximize the peak intensities of the new, unknown species so it could be identified. Regrettably, the magnesiated product was extremely unstable and caught on fire once exposed to ambient conditions, rendering it difficult to characterize. It is likely that the pyrophoric nature of the magnesiated material was due a significant amount of MgH_2, which was observed as white particles mixed in with the grey-

colored boride. PXRD of the magnesiated material under inert conditions was attempted to avoid exposing the magnesiated product to air. The modified CaB_6 was deposited onto a welled glass slide and covered with Kapton tape and PXRD was re-attempted. However, the overall pattern was much noisier due to the amorphous nature of the tape covering the hexaboride; this made the data unreliable, especially in light of the low intensity of the peaks corresponding to the unknown species. Advanced characterization of these materials, such as synchrotron diffraction, might prove useful to obtain better data.

High Temperature Reactions at 80 °C

Reactions at elevated temperatures were performed with the aim to decrease the overall reaction time. Ground bulk was used for these reactions in order to achieve optimal results, and it was determined that a 14-day reaction at 80 °C yielded the best nanoproduct. The PXRD patterns of the magnesiated and aqueous exfoliated products matched to those of bulk CaB_6, similar to the room temperature reactions, and no additional peaks were detected. Additionally, SEM-EDS of the magnesiated product confirmed the presence of Mg in the sample as well as the preservation of the original morphology of the crystals.

Once exfoliated in water, TEM-SAED was performed to evaluate the nanoproduct. The microscopy images showed two types of morphologies. First, uniform rectangular nanosheets were observed (Figure 3.8 A) that appeared thinner (based on contrast) than previously synthesized products using Mg^{2+} incorporation. When compared with lithiation techniques, the reaction time of the ion incorporation reaction step is significantly decreased for Mg^{2+} (14 days) than for Li^{+} (3 months). These results support our hypothesis that using a metal ion from the same group as that of the metal in the boride should lead to improved ion incorporation and consequently greater nanosheet formation. The second morphology observed was small

nanoparticles on the sheets (Figure 3.8 B). Their polycrystalline diffraction pattern was indexed to MgO, which indicates that exposure to elevated temperature leads to the decomposition of di-*n*-butylmagnesium to MgH_2, which in turn forms MgO once exposed to aqueous conditions. Thus reactions longer than 2 weeks at elevated temperatures will be most likely ineffective.

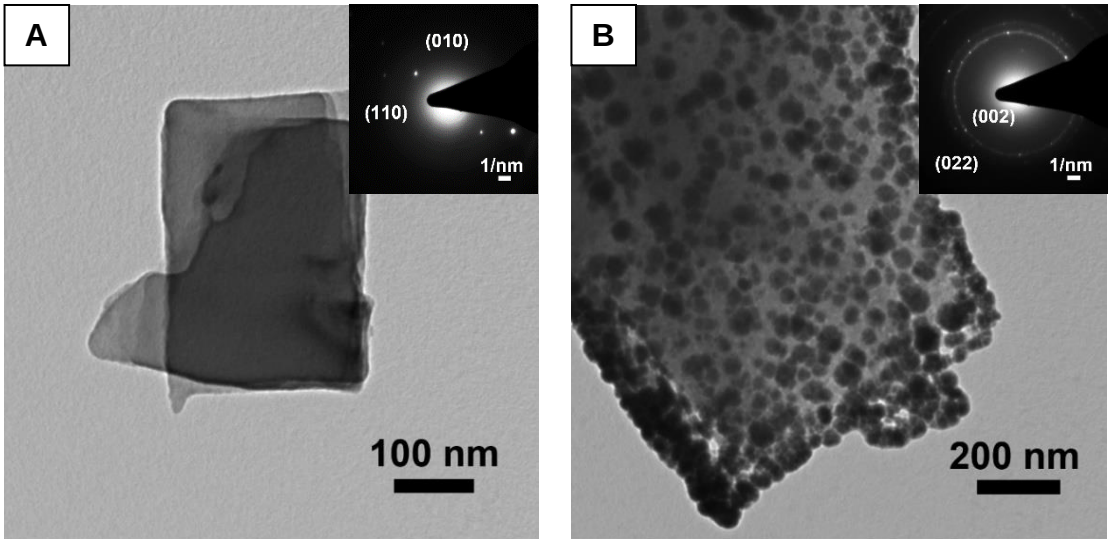

Figure 3.8. TEM images with corresponding SAED (inset) of exfoliated CaB_6 nanosheets (A) and MgO nanoparticles (B) from a 14-day reaction at 80 °C

Control Reactions

Control reactions with hexane were executed with both ground and as-received bulk CaB_6 to verify that any nanosheet formation resulted from our methodology. Both control reactions produced products with PXRD patterns matching the bulk. Once the CaB_6 was probe sonicated, the final morphology was evaluated and compared to that of the magnesiation-exfoliation reactions. TEM of the product derived from as-received bulk (Figure 3.9 A) and STEM of the product derived from ground bulk (Figure 3.9 B) both showed thick, uneven crystals, indicating that no exfoliation occurred due to the stirring and handling processes alone.

This piece of data validates that nanosheet products are due to the ion incorporation/exfoliation chemistry.

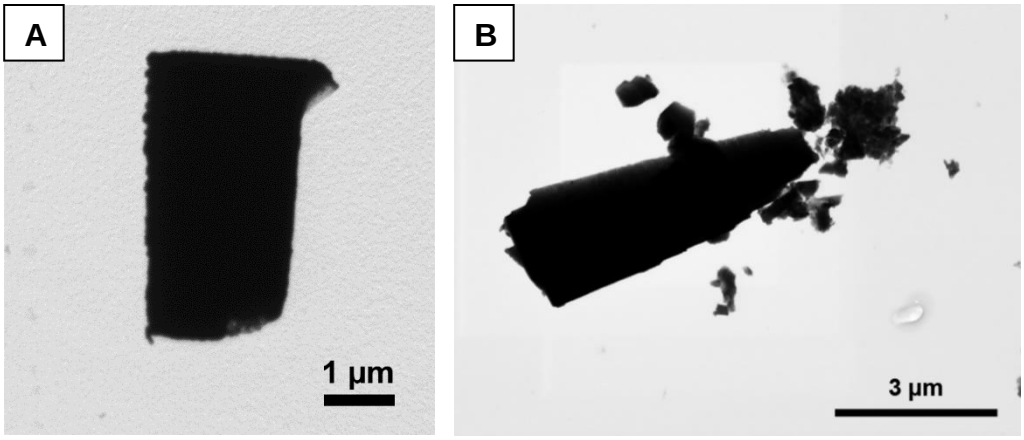

Figure 3.9. TEM image of a control reaction with unground CaB_6 and STEM of a control reaction with ground CaB_6

Conclusion

Calcium hexaboride was magnesiated successfully using di-*n*-butylmagnesium, and the presence of magnesium was confirmed using elemental mapping. There's some preliminary evidence that Mg is likely to incorporate at the edges of the crystals, which makes it possible for incorporation to occur more rapidly and the exfoliation to happen more easily. Additionally, reaction times ≥ 4 weeks yielded products whose PXRD patterns showed the presence of an additional species. This new compound can be hypothesized to be a Mg-B species based on previous work with lithiation techniques, but additional characterization needs to be conducted to confirm its identity.

Nanosheets with a variety of thicknesses were obtained depending on the reaction conditions used. We determined several key factors for getting the optimal results. Firstly, it was important to obtain use bulk material with particle size, so the bulk CaB_6 was ground using a mortar and pestle. A technique like planetary ball milling could be utilized in future experiments in order to achieve a more uniform reduction of the bulk particle size and avoid the formation of boride nanoparticles. Next, increasing the magnesiation time led to progressively improved results. However, reaction time longer than 4 weeks proved ineffective. Finally, elevated temperature produced optimum results, leading to the isolation of thin, uniform CaB_6 nanosheets.

The successful magnesiation and exfoliation of CaB_6 is a significant improvement in the formation of CaB_6 nanosheets because lithiation methods require long reaction times. It also verifies the versatility of the ion incorporation method by application to an alkaline-earth metal hexaboride and the successful demonstration of non-aqueous media for exfoliation. Finally, it provides new evidence for the potential formation of previously unknown Mg-B species *in situ*.

References

1. Amin, S. S.; Li, S.-y.; Roth, J. R.; Xu, T. T., Single crystalline alkaline-earth metal hexaboride one-dimensional (1D) nanostructures: synthesis and characterization. *Chemistry of Materials* **2009,** *21* (4), 763-770.

2. Matkovich, V. I., *Boron and Refractory Borides*. Springer, Berlin, Heidelberg: 1977.

3. Muranaka, S.; Kawai, S., Crystal growth of alkaline earth hexaborides. *Journal of Crystal Growth* **1974,** *26*, 165-168.

4. Ott, H. R.; LGavilano, J.; Ambrosini, B.; Vonlanthen, P.; Felder, E.; Degiorgi, L.; Young, D. P.; Fisk, Z.; Zyslerc, R., Unusual magnetism of hexaborides. **200,** *281*, 423-427.

5. Bao, L.; Qi, X.; Tana; Chao, L.; Tegus, O., Synthesis, and magnetic and optical properties of nanocrystalline alkaline-earth hexaborides. *CrystEngComm* **2016,** *18* (7), 1223-1229.

6. Takeda, M.; Terui, M.; Takahashi, N.; Ueda, N., Improvement of thermoelectric properties of alkaline-earth hexaborides. *Journal of Solid State Chemistry* **2006,** *179* (9), 2823-2826.

7. Yin, H.; Tang, D.; Mao, X.; Xiao, W.; Wang, D., Electrolytic Calcium Hexaboride for High Capacity Anode of Aqueous Primary Batteries. *Journal of Materials Chemistry A* **2015,** *3* (29), 15184-15189.

8. Xu, J.; Zhao, Y.; Zou, C.; Ding, Q., Self-catalyst growth of single-crystalline CaB_6 nanostructures. *Journal of Solid State Chemistry* **2007,** *180* (9), 2577-2580.

9. Bao, K.; Lin, L.; Chang, H.; Zhang, S., Low-temperature synthesis of calcium hexaboride nanoparticles via magnesiothermic reduction in molten salt. *Journal of the Ceramic Society of Japan* **2017,** *125* (12), 866-871.

10. Ramachandran, R. Nanostructured Metal borides and Metal Fluorides. University of Georgia, Athens, Georgia, 2017.

CHAPTER 4

MAGNESIATION AND EXFOLIATION OF STRONTIUM AND BARIUM HEXABORIDE

Milkovska, M. and Salguero, T.T. To be submitted to *Chemistry of Materials*

Abstract

Strontium and barium hexaboride, SrB_6 and BaB_6, are modified using di-*n*-butylmagnesium and exfoliated in DI H_2O. The magnesiated products are characterized and the presence of Mg is confirmed using EDS. No morphological changes were observed in either modified boride, contrasting previous data obtained from lithiation methods. PXRD is utilized to track any structural changes as the borides were magnesiated and exfoliated. SrB_6 doesn't show any indication of the presence of additional species, while BaB_6 provides some evidence of the potential formation of a Mg-B, which was previously observed in CaB_6 experiments. Reactions of both modified borides with water lead to the successful delamination of the materials and the generation of two-dimensional nanoplatelets with lateral dimensions between 0.2-1 μm.

Introduction

Strontium and barium hexaborides (SrB_6 and BaB_6) belong to a subgroup of the metal hexaborides named the alkaline earth hexaborides. Throughout the years, many synthetic approaches have been discovered to synthesize these materials including a variety solid state methods,[1-3] vapor deposition techniques[4-5] and combustion synthesis.[6] Their unique properties have been studied in the bulk and more recently their alloying[7-8] and nanostructuring[5, 9] have risen to the forefront on their investigation.

Nanostructuring of SrB_6 and BaB_6 has been focused primarily on bottom-up approaches yielding nanoparticles[10-11] and nanowires.[5, 9] Top-down methodologies, however, haven't been studied extensively mainly due to the difficult disassembly the strongly bonded metal-boron framework. One such study utilizes the incorporation of a small metal ion (Li^+) into the bulk SrB_6 followed by a reaction with water to yield uniform nanoparticles.[12] The same approach has also been utilized to form nanosheets of a rare earth hexaborides (LaB_6, CeB_6 and SmB_6).[13] Thus, we aim to apply this methodology with some modifications to explore the chemistry of BaB_6 and SrB_6.

In this chapter, we use Mg^{2+} for the metal ion incorporation step. Previously, we have successfully magnesiated and exfoliated another alkaline earth boride, CaB_6 (see Chapter 3). CaB_6 modification was recorded to proceed similarly in both lithiation and magnesiation approaches and while the reactions yielded nanosheets in both cases, the magnesiation route provided much shorter reaction times to do so. Thus, our objective is to provide an analogous comparison with SrB_6, particularly in light of the unusual nanoproduct that it forms upon lithiation. Additionally, we provide a further comparison with the modification of the last boride from the alkaline earth boride group, i.e. BaB_6.

Experimental

Materials: Strontium hexaboride (powder, Office of Naval Research, USA), barium hexaboride (powder, Office of Naval Research, USA), 1 M di-n-butylmagnesium in heptane (Sigma-Aldrich), hexanes (98.5%, Fisher).

Reaction of SrB_6 with Di-*n*-Butylmagnesium: In a typical magnesiation experiment, 0.152 g (1 mmol) of bulk SrB_6 powder was deposited into a glass vial together with a Teflon stir bar. Next, the vial was transferred to an argon-filled glovebox with levels of $O_2 < 5$ ppm and $H_2O < 0.1$ ppm. Inside the box, 5 mL of 1M di-*n*-butylmagnesium was added to the vial via a syringe and the vial was capped and sealed with Parafilm® M. The reaction was stirred for 5-30 days at room temperature. For elevated temperature reactions, the vial with the boride/ magnesiation reagent mixture was put in an aluminum bead bath for even heating and a hot plate set at 80 °C was utilized. After the reaction was finished, the magnesiated boride was separated from the rest of the mixture using vacuum filtration. The product was then extensively washed with hexane and allowed to dry in a clean vial overnight. 0.134 g of magnesiated hexaboride was recovered (88% yield).

Exfoliation of SrB_6 in Water: For the exfoliation step, 0.080 g of magnesiated SrB_6 was removed from the glovebox and added to a centrifuge tube. Next, 20 mL of DI H_2O were added and the mixture was centrifuged at 10,000 rpm for 30 min. The solvent and soluble byproducts were decanted and another 20 mL of DI H_2O were added to the centrifuge tube containing the boride. The dispersion was then probe sonicated at 50 amplitude for 1 hour. Approximately 100-200 µl of the mixture were used to examine the material via TEM/SAED. The remaining nanoproduct was dried in a vacuum overnight at 40 °C. 0.061 g of exfoliated product was retrieved (76% yield).

Reaction of BaB_6 with Di-*n*-Butylmagnesium: A total of 0.202 g (1 mmol) of BaB_6 powder was used for the reaction with di-*n*-butylmagnesium. The magnesiation reactions were executed in the same manner as the reactions with SrB_6, except that the bulk was ground for 15 minutes using an agate mortar and pestle prior to the addition of the magnesiation reagent. The reaction produced 0.182 g of product (90% yield).

Exfoliation of BaB_6 in Water: The reactions of magnesiated BaB_6 with DI H_2O were executed similarly to those with the strontium equivalent. 0.100 g of modified BaB_6 was used for the exfoliation step and 0.083 g was retrieved (83% yield).

Characterization: The composition of the bulk, magnesiated and exfoliated materials was confirmed using a Bruker D8-Advance powder X-ray diffractometer (Co-Kα radiation, λ=1.7889 Å) operated at 35 mA/40 kV and with a scanning rate of 0.2 sec per step over the 2θ range of 5−70°. A FEI Teneo field emission gun scanning electron microscope (FEG-SEM) in conjunction with an Oxford energy dispersive spectroscopy (EDS) system operated at 5-10 keV was used to determine the morphology and elemental composition of the magnesiated material. SEM sample preparation consisted of depositing the magnesiated powders onto carbon sticky tape. The same instrument operated at 30 kV was utilized to perform scanning transmission electron microscopy (STEM) in order to study the morphology of the exfoliated products. Further characterization was done using a FEI Tecnai 20 (200 kV) transmission electron microscope (TEM) equipped with selected area electron diffraction (SAED), which was used to confirm the identity of the nanomaterial. STEM/TEM samples were drop cast onto Formvar grids and allowed to dry in air.

Results and Discussion

Reactions of SrB_6 with di-*n*-butylmagnesium were performed at room temperature and 80 °C. The magnesiated and exfoliated materials at different reactions times were compared to determine the optimal conditions for the formation of nanosheets. Results were also evaluated against those obtained by lithiation techniques. BaB_6 underwent similar experiment to provide an additional set of comparison.

Reactions of SrB_6 with Di-n-Butylmagnesium at Room Temperature

Strontium hexaboride was magnesiated for different amounts of time between 5 and 30 days. The PXRD patterns from these reactions remained similar as the reaction time was varied. It was observed that magnesiated and exfoliated products both match the bulk pattern well (Figure 4.1). One difference that was observed was that a slight peak broadening in the pattern of the magnesiated boride which transformed into a peak on the left of the main boride peak (lower

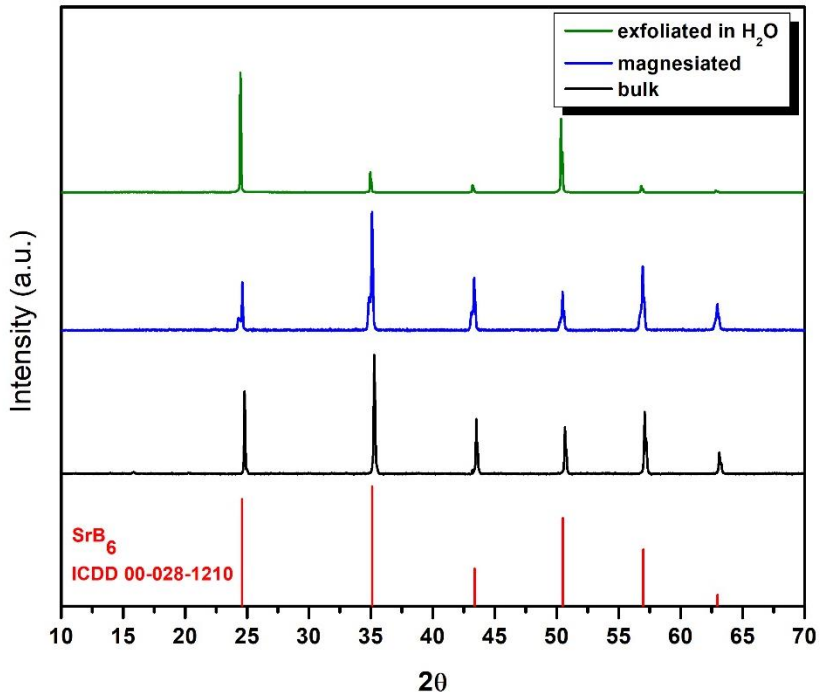

Figure 4.1. PXRD of bulk, magnesiated and exfoliated SrB_6 from a 14-day

2θ). This difference was determined to be an artifact of the diffractometer and can be disregarded (See Chapter 2 for details). Additionally, a change in the relative peak intensity was seen in the exfoliated product and the peaks ~ 24.5 and 50.5 2θ were significantly more intense that the rest of the peaks. The two peaks correspond to the (h00) set of crystal planes and their increased intensity was due to the fact that the exfoliated samples were drop-casted onto a glass slide and then dried in order to examine them, which allowed the crystals to express one set of crystal planes as the water evaporated. When the samples were dried under vacuum to produce a nanopowder and then underwent PXRD, the relative intensity of all peaks was retained.

The morphology of the magnesiated products was examined via SEM/EDS and compared to the bulk boride. The bulk crystals consisted of particles that are ~10-30 μm in size and were composed of multiple platelets (Figure 4.2 A). Once magnesiated, the boride retained its original morphology and the only a slight rounding of the edges was observed which was most likely due to the stirring process (Figure 4.2 B). The elemental mapping showed the presence of the

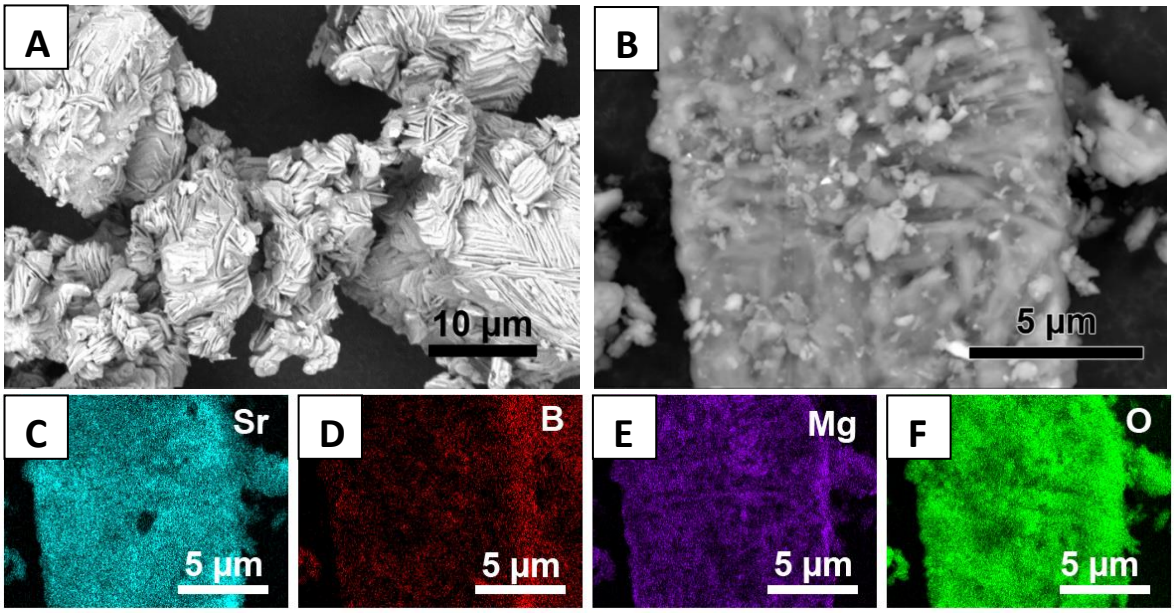

Figure 4.2. SEM images of bulk (A) and magnesiated (B) SrB_6 with corresponding Sr (C), B (D), Mg (E) and O (F) elemental mapping

expected elements (Sr, B and O) as well as Mg which indicated that the magnesiation was successful (Figure 4.2 C-F).

Once characterized, the magnesiated materials from the varying reaction times were reacted with DI H_2O to produce the final product. While shorter reaction times didn't lead to successful delamination and the formation of desired nanomorphology, around 14 days nanoplatelets began to form (Figure. 4.3). The observed platelets were 200-500 nm in lateral dimensions and appeared to be uniform in thickness suggesting they were formed due to the exfoliation process, not the prolonged stirring. Increasing the reaction time up to 4 weeks demonstrated similar results and thus it was concluded that additional modification of our methodology needed to be done in order to achieve thinner, more sheet-like final product.

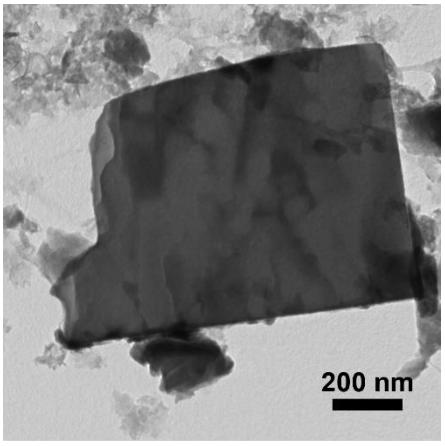

Figure 4.3. TEM of a typical SrB_6 nanoplatelet from a 14-day reaction

Reactions of SrB_6 with Di-n-Butylmagnesium at 80 °C

Elevated temperature reaction at 80 °C were performed in order to observe the influence of temperature on the final product. Previously, lithiation techniques at an elevated temperature produced three unique findings – (1) modified SrB_6 showed a drastic change in morphology compared to the bulk, (2) nanoparticles were formed instead of nanosheets during the reaction

with water and (3) the reaction proceeded through the formation of a Li_2B_6 species whose structure is similar to that of the hexaborides.[12] While a direct Mg-B equivalent has yet to be discovered as of the writing of this work, there's been some evidence of the existence of a MgB_6 structure instead.[14] Thus, it's essential to draw a comparison between the two modification techniques in order to understand their chemistry better.

Strontium hexaboride was magnesiated at 80 °C with reaction times between 5 days and 3 weeks and then exfoliated in water. Throughout the reaction time study, no structural changes or formation of additional species was observed via PXRD. As the Li-B species was observed as early as 11 days during lithiation of SrB_6, our results indicate that if any Mg-B species was formed, it was either in too small of amounts that it couldn't be detected with our techniques or it is unstable in air similarly to Li_2B_6. Additional characterization is required to confirm its presence. An example of a typical PXRD pattern for elevated temperature reactions is given in Figure 4.4.

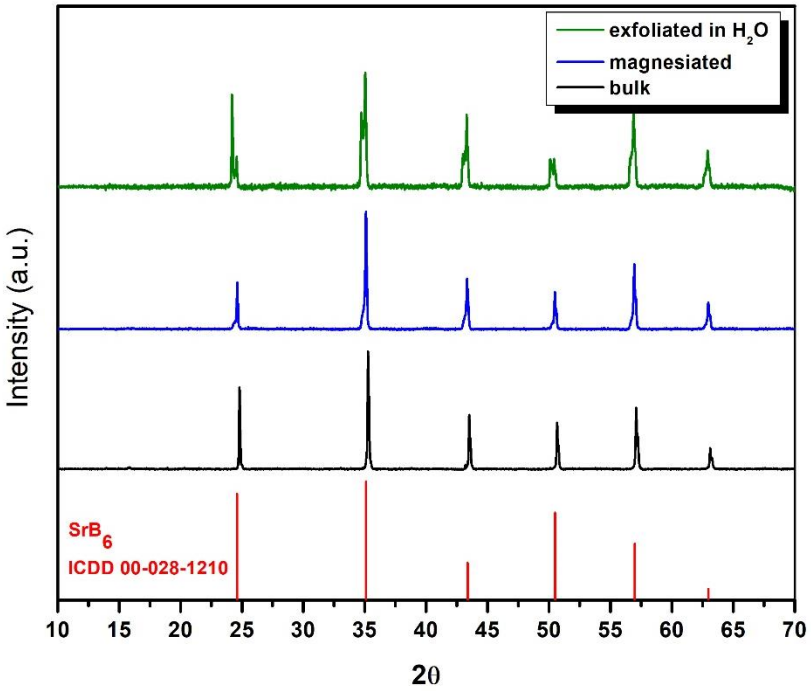

Figure 4.4. PXRD of bulk, magnesiated and exfoliated SrB_6 from a 5-day reaction at 80 °C

The morphology of the bulk SrB_6 was retained after magnesiation at high temperature similarly to the room temperature reactions. This contrasts vastly with the lithiated boride which shows significantly different modified morphology from the bulk[12]. Such lack of morphological changes paired with the PXRD data presented above suggest that perhaps the magnesiation process occurs differently than that of the lithiation equivalent. This conclusion is also supported by the morphology of the exfoliated product. TEM images of the material after reaction with water shows the presence of plate-like SrB_6 similarly to the room temperature reactions (Figure 4.5 A). Its respective SAED and matched d-spacings confirm its structure with certainty. Additionally, it's worth noting that while the magnesiation-exfoliation methodology can be applied to SrB_6 successfully, our work shows that CaB_6 produces much more uniform final product than SrB_6 with much shorter reaction times (see Chapter 3). Finally, some MgO was also formed during these reactions which suggests that di-*n*-butylmagnesium is decomposing to MgH_2 due to the elevated temperature, which in turn converts to MgO in aqueous conditions. This phenomenon was also observed in the CaB_6 reactions at 80 °C, where MgO nanoparticles were formed on the smooth surface of the hexaboride. In the strontium boride case, the MgO

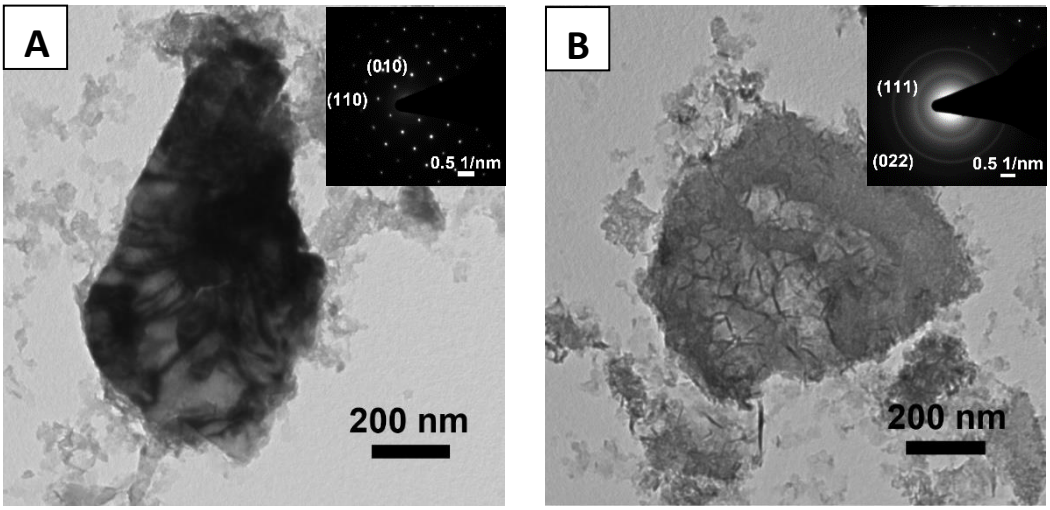

Figure 4.5. TEM of exfoliated SrB_6 from a 3-week reaction at elevated temperature (A) and MgO from the same reaction (B) with respective SAED (insets)

grows similarly to the flaky structure of the SrB_6 bulk, which is possibly why we observe a MgO with almost sheet-like morphology as opposed to nanoparticles (Figure 4.5 B). The respective SAED (inset) reveals the presence of both polycrystalline diffraction pattern of the magnesium biproduct and the cubic single crystalline pattern of the hexaboride. Thus, we concluded that prolonged reactions at elevated temperatures are inefficient to produce thinner, more uniform nanosheets and additional adjustments to the methodology might be needed to achieve that.

Reactions of BaB_6 with Di-n-Butylmagnesium at Room Temperature

Before proceeding with the magnesiation reaction, BaB_6 bulk required 15 minutes of grinding with a mortar and pestle as the bulk boride crystals were enveloped in platelets of an additional species. While we couldn't eliminate the extra material completely (Figure 4.6), the grinding process allowed us to simply remove it from the surface of the boride in order to allow the boride to be in direct contact with the magnesiation reagent during the subsequent reactions. The additional material was determined to be BaB_2O_4 based on EDS and SAED data, which is a known transition phase of the synthesis of BaB_6.[15]

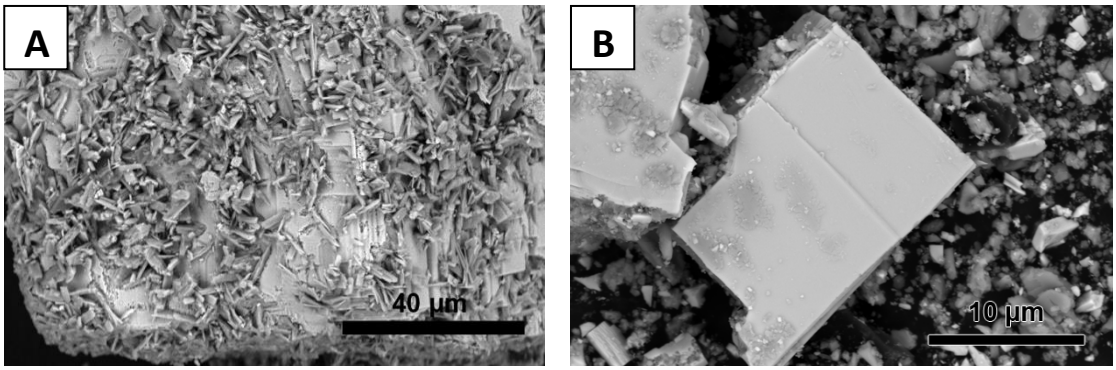

Figure 4.6. SEM of BaB_6 bulk before (A) and after (B) grinding

After grinding, the hexaboride was magnesiated at room temperature with reaction times between 1-4 weeks. PXRD patterns of BaB_6 magnesiated and exfoliated in H_2O for almost all reactions matched the bulk well and not structural changes were observed. When the reaction

time reached 4 weeks, a less intense peak around ~22 2θ was observed (Figure 4.7). While such peak wasn't observed in the month-long magnesiation of SrB_6, a similar peak was seen previously with CaB_6 under the same reaction conditions and was hypothesized to be from a Mg-B species (see Chapter 3). This piece of data indicates that both BaB_6 and CaB_6 magnesiation reactions possibly proceed though the formation of the same intermediates, which can only be observed at reaction times ≥ 4 weeks.

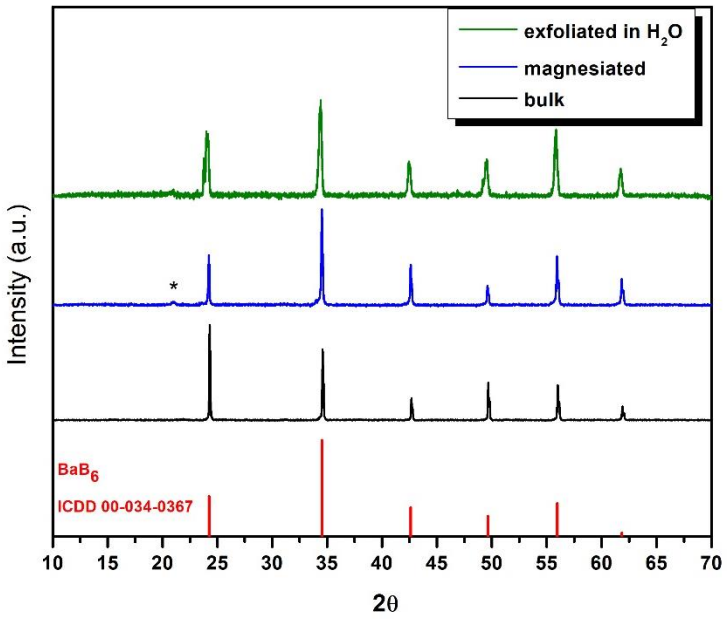

Figure 4.7. PXRD of BaB_6 bulk, magnesiated and exfoliated in H_2O from a 4-week reaction. Asterisk denotes an additional species

The magnesiated BaB_6 was characterized via SEM-EDS. Similarly to SrB_6 and CaB_6, the barium equivalent didn't undergo any morphological changes during the magnesiation process. The crystals' surface remained smooth and some of the layers of the material began showing at the edges (Figure 4.8 A). EDS mapping was executed to confirm the elemental composition of the modified material. Barium, boron and oxygen were present as expected; magnesium was also detected uniformly on the crystals indicating that the metal ion incorporation has proceeded

successfully. Some Mg- and O-rich areas were detected indicating some formation of MgO has already occurred most likely due to exposure to the ambient conditions outside of the glovebox.

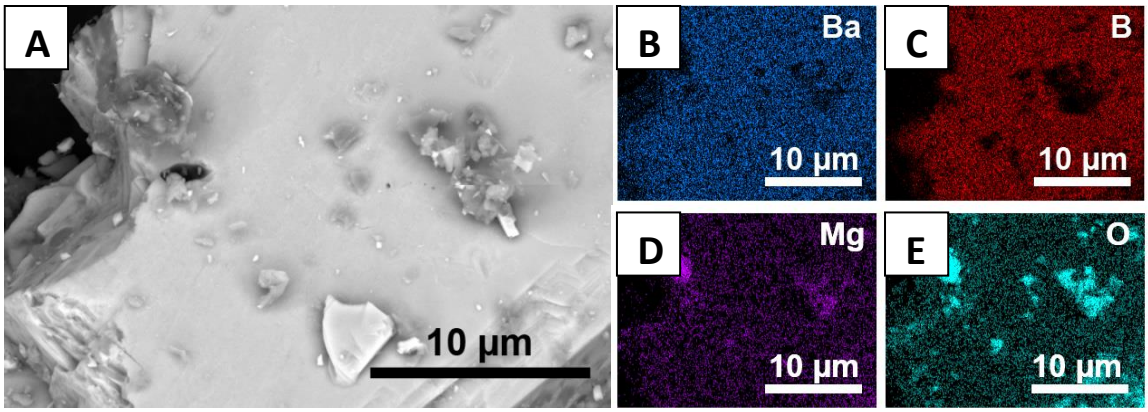

Figure 4.8. SEM image of magnesiated BaB_6 (A) with corresponding Ba (B), B (C), Mg (D) and O (E) mapping

When exfoliated in DI water, BaB_6 produced platelets with dimension of 0.5-1 µm. The product appeared to be uniform, but thick based on the bright field contrast in the 1-to-2-week reactions (Figure 4.9 A). In experiments with reaction times ≥ 2 weeks, thinner platelets began forming (Figure 4.9 B) and their composition was confirmed with elemental mapping (Figure 4.9 C-D). Additional characterization with SAED confirmed that the observed morphology was indeed the hexaboride by indexing its crystal planes to cubic BaB_6. While reaction with longer times were not performed, it can be inferred based on previous work with other hexaborides that longer reaction times will be ineffective.

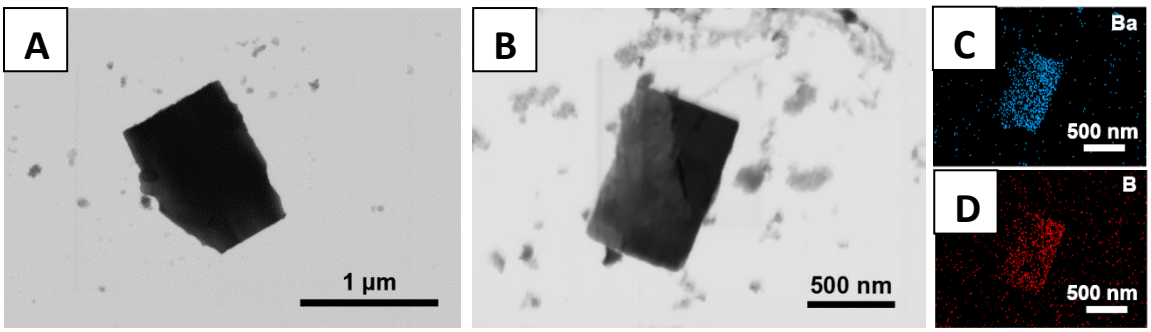

Figure 4.9. STEM image of exfoliated BaB_6 from a 1-week reaction(A) and a 4-week reaction (B) with corresponding Ba (C) and B (D) mapping

Reactions of BaB_6 with Di-n-Butylmagnesium at 80 °C

Preliminary reactions of BaB_6 with di-*n*-butylmagnesium at 80 °C were performed. For these reactions, PXRD confirmed that, similarly to SrB_6, no observable structural changes have occurred due to the magnesiation at high temperature. Unlike the strontium equivalent, however, the exfoliated barium hexaboride didn't appear to benefit from the elevated temperature and the final product appeared to be more like the thicker platelets from the 1-week reaction at room temperature rather than the 2-to-4-week reactions (Figure 4.10). There are several possible explanations for what we observed. Firstly, as previously noted the magnesiation reagent degrades at above room temperature, so it's possible that over time the di-*n*-butylmagnesium (despite the proper storage) begins to slowly degrade before it is even added to the boride. This will make the magnesiation reagent much less effective especially when exposed to elevated temperatures. Secondly, the bulk powder contained some additional material mixed in with the BaB_6. While we attempted to mitigate its influence on the magnesiation process by grinding the bulk powder, we cannot say with certainty that its effect on the reaction progression was completely eradicated. Thus its presence could have either prevented the Mg ions to reach the

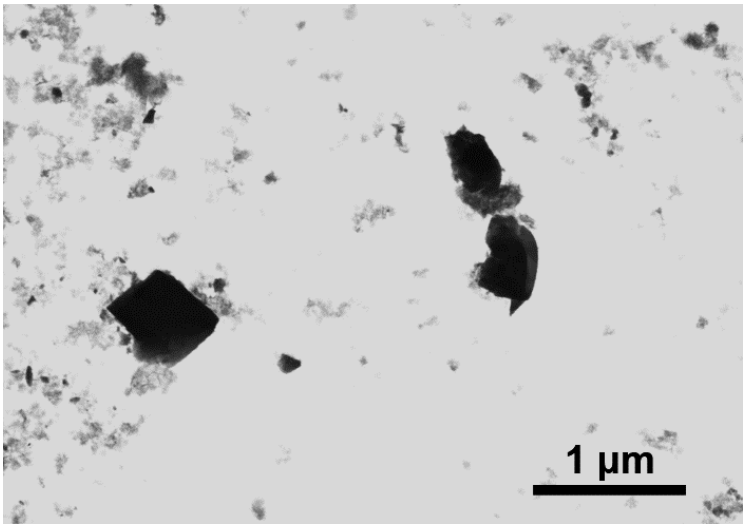

Figure 4.10. STEM image of exfoliated BaB_6 from a 1-week reaction at 80 °C

surface of the boride or the material itself could have been magnesiated to some extent, which would decrease the amount of Mg^{2+} available to be incorporated into the boride and lead to less than satisfactory results. And lastly, it was observed that the magnesiation/reaction with water methodology seems to achieve delamination will all three alkaline earth borides explored in this work, but there seems to be a trend when doing down the period. We've observed greatest results with the CaB_6 and the final nanoproduct of the following two borides appear to be a bit less satisfactory in SrB_6 and even less so in BaB_6. Such trend could be potentially attributed to the size of the Mg^{2+} – at 72 pm, it is much closer in size to the Ca ion (100 pm), than Sr ion (118 pm) or Ba ion (135 pm). Whatever position the Mg ions may occupy as they get incorporated, having a metal in the boride with similar features and chemistry can potentially ease the incorporation leading to improved final results. Additional experiments at high temperature may be required to provide additional evidence of this trend.

Conclusion

Strontium and barium hexaboride were successfully magnesiated and exfoliated in water. During the SrB_6 experiments, it was determined that the magnesiation and exfoliation proceed differently than previously explored lithiation approaches. Firstly, no evidence was found of the formation of Mg-B species equivalent of the Li_2B_6 seen in high temperature lithiation reactions. Additionally, the final product of both room temperature and 80 °C reactions had a two-dimensional morphology rather than the previously seen nanoparticles. Finally, though the magnesiation via di-*n*-butylmagnesium provided adequate results in the form of uniform SrB_6 platelets, reagents with higher Mg concentration might need to be explored to achieve the optimal nanosheet morphology.

Barium hexaboride also demonstrated some promising results. It was discovered that increasing the reaction time could lead to nanoplatelet formation, similar to the strontium equivalent, but increasing the temperature didn't prove as effective. In addition, PXRD of longer reaction times provided evidence of the potential formation of the Mg-B species also found in CaB_6 magnesiation reactions. Thus, it can be hypothesized that the chemical route for the modification of BaB_6 resembles that of the CaB_6, but the final product is much more similar to that of the Sr counterpart. Obtaining a pure BaB_6 bulk powder will be of great importance for future experiments in order to avoid interference during magnesiation.

The experimental results of the reactions with SrB_6 and BaB_6 established that even though the two compounds belong to the same group, their chemistry is not always identical. Having the comparison between the two as well as the comparison with lithiation reactions has broadened our understanding of the underlying processes that can occur during these

experiments. Thus, this approach can be now expanded to the rest of the vastly broad boride group making them much more industrially adaptable and easy to work with.

References

1. Aida, T.; Honda, Y.; Yamamoto, S.; Kawabe, U., Preparation, vapor pressure, and thermionic emission properties of BaB_6 powder. *Journal of Applied Physics* **1981,** *52* (2), 1022-1029.

2. Grechnev, G. E.; Baranovskiy, A. E.; Fil, V. D.; Ignatova, T. V.; Kolobov, I. G.; Logosha, A. V.; Shitsevalova, N. Y.; Filippov, V. B.; Eriksson, O., Electronic structure and bulk properties of MB_6 and MB_{12} borides. *Low Temperature Physics* **2008,** *34* (11), 921-929.

3. Min, G.; Zheng, S.; Zou, Z.; Yu, H.; Han, J., Reaction synthesis and formation mechanism of barium hexaboride. *Materials Letters* **2003,** *57* (7), 1330-1333.

4. Amin, S. S.; Li, S.-y.; Roth, J. R.; Xu, T. T., Single crystalline alkaline-earth metal hexaboride one-dimensional (1D) nanostructures: synthesis and characterization. *Chemistry of Materials* **2009,** *21* (4), 763-770.

5. Wu, X.; Xu, T. T., Measurement of mechanical properties of alkaline-earth metal hexaboride one-dimensional nanostructures by nanoindentation. *Journal of Materials Research* **2012,** *27* (9), 1218-1229.

6. Cahill, J. T.; Alberga, M.; Bahena, J.; Pisano, C.; Borja-Urby, R.; Vasquez, V. R.; Edwards, D.; Misture, S. T.; Graeve, O. A., Phase Stability of Mixed-Cation Alkaline-Earth Hexaborides. *Crystal Growth & Design* **2017,** *17* (6), 3450-3461.

7. Koch, R.; Metz, P. C.; Jaime, O.; Vargas-Consuelos, C. I.; Borja-Urby, R.; Ko, J. Y. P.; Cahill, J. T.; Edwards, D.; Vasquez, V. R.; Graeve, O. A.; Misture, S. T., Nanodomains and local structure in ternary alkaline-earth hexaborides. *Journal of Applied Crystallography* **2018,** *51* (5), 1445-1454.

8. Takeda, M.; Terui, M.; Takahashi, N.; Ueda, N., Improvement of thermoelectric properties of alkaline-earth hexaborides. *Journal of Solid State Chemistry* **2006,** *179* (9), 2823-2826.

9. Jash, P.; Nicholls, A. W.; Ruoff, R. S.; Trenary, M., Synthesis and Characterization of Single-Crystal Strontium Hexaboride Nanowires. *Nano Letters* **2008,** *8* (11), 3794-3798.

10. Jalaly, M.; Khosroshahi, B. K.; Gotor, F. J.; Sayagués, M. J.; Yamini, S. A.; Failamani, F.; Mori, T., Mechanically induced combustion synthesis and thermoelectric properties of nanostructured strontium hexaboride (SrB_6). *Ceramics International* **2019,** *45* (11), 14426-14431.

11. Xiaohua Zhao; Guanghui Min; Lin Zhang; Limei Liang; Yu, H., Low Temperature Synthesis of BaB6 Nanometer Powders. *International Journal of Modern Physics B* **2012,** *23*.

12. Ramachandran, R.; Salguero, T. T., Nanostructuring of Strontium Hexaboride via Lithiation. *Inorganic Chemistry* **2018,** *57* (1), 4-7.

13. Ramachandran, R. Nanostructured metal borides and metal fluorides. University of Georgia, Athens, Georgia, 2017.

14. Angappan, S.; Kalaiselvi, N.; Sudha, R.; Visuvasam, A., Electrochemical Synthesis of Magnesium Hexaboride by Molten Salt Technique. *International Scholarly Research Notices* **2014,** *2014*, 1-6.

15. Ropp, R. C., Chapter 6 - Group 13 (B, Al, Ga, In and Tl) Alkaline Earth Compounds. In *Encyclopedia of the Alkaline Earth Compounds*, Ropp, R. C., Ed. Elsevier: Amsterdam, 2013; pp 481-635.

CHAPTER 5

NANOSTRUCTURING OF LITHIUM MANGANESE AND LITHIUM COBALT PHOSPHATES

Milkovska, M. and Salguero, T.T. To be submitted to *Chemistry of Materials*

Abstract

$LiCoPO_4$ nanosheets are synthesized using a $Co_3(PO_4)_2 \cdot 4H_2O$ nanosheet precursor in a H_2O/DEG or H_2O/EG mixture. The effects of time, solvent ratio, Li sources and reaction temperature are explored during the solvothermal synthesis to determine the best experimental parameters. Uniform nanosheets with lateral dimension of 5-10 μm are successfully synthesized at 250 °C, and we demonstrate that the reaction conditions play a crucial role in both the morphology and composition of the final products. Additionally, we demonstrate the use of planetary ball-milling as a tool to reduce lateral dimension of $LiMnPO_4$ nanosheets without the loss of dimensionality. Ball-milling in a liquid medium has shown the most promising results compared to dry ball-milling and H_2O provides the best reduction of size without the formation of nanoparticles.

Introduction

$LiMPO_4$ (M= Mn, Fe, Co, Ni) materials are olivine-structured orthophosphates that have been studied as an alternatives of oxides for battery cathodes.[1] Their popularity has increased due to their high energy density, thermal stability, and low raw materials cost.[2-4] While one of them, $LiFePO_4$, has been commercially adapted, considerable effort has been focused on overcoming the drawbacks of these materials to apply them to their full potential.

One main pathway to improve their processability and performance is nanostructuring. $LiCoPO_4$ has been synthesized in variety of nanostructures using solid state,[5-7] hydrothermal/ solvothermal[8-10] and sol-gel methods.[11-12] While most commonly nanoparticles are the final product, some nanosheets have been synthesized and shown promising battery performance.[2] In the hydrothermal/solvothermal category, often a mixture of H_2O with an organic solvent or a surfactant are used to direct the growth into the different morphologies.[13] For 2D materials that particularly important as specific exposed facets are important for speedy Li diffusion.[13-14]

Anisotropic $LiMnPO_4$ nanosheets have been previously synthesized in a H_2O:DEG mixture.[15] These nanosheets display the (200) crystal plane as opposed to the ideal (020) one, but their promising battery performance has gained an interest to study them from a Li^+ diffusion standpoint. As shown with multiple nanomaterials, the dimensions of the nanostructures has a profound effect on their battery capabilities, so optimizing the lateral dimensions of these micron-sized $LiMnPO_4$ nanosheets, while retaining their 2D nature, offer the possibility of improving their performance significantly.

In this chapter, we report a facile solvothermal synthesis of $LiCoPO_4$ nanosheets using a $Co_3(PO_4)_2 \cdot 4H_2O$ template using H_2O:DEG and H_2O:EG mixtures at 250 °C. We also study the

use of planetary ball-milling of $LiMnPO_4$ synthesized using the methodology described above. We attempt to reduce the nanosheets' lateral dimension using mechanical force with the aim of improving battery performance.

Experimental

Materials: $CoCl_2 \cdot 6H_2O$ (Acros Organics, 98%), H_3PO_4 (Sigma-Aldrich, 85 wt % in water), NaOH (Sigma-Aldrich, ≥97%, pellets), LiH_2PO_4 (Sigma-Aldrich, 99%), diethylene glycol (Sigma Aldrich, 99%), ethylene glycol (Sigma Aldrich ≥ 99%), $Mn(CH_3COO)_2 \cdot 4H_2O$ (Sigma-Aldrich ≥99%), $(NH_4)_2HPO_4$ (Sigma-Aldrich, ≥98%).

Preparation of $Co_3(PO_4)_2 \cdot 4H_2O$ Nanosheets: In a 500 mL round-bottom flask, 1.000 g (4.20 mmol) of $CoCl_2 \cdot 6H_2O$ was dissolved in 150 mL of DI H_2O. Then 0.405 mL (6.15 mmol) of 15.2 M H_3PO_4 was added and the mixture was stirred under reflux for 30 min. Next, 60.3 mL (12.06 mmol) of 0.2 M NaOH was added dropwise, and the reflux process was continued for 17 h. After the reaction was finished, the mixture was allowed to cool to room temperature, and the violet precipitate was isolated by centrifugation at 10,000 rpm for 30 min. The product was washed with 30 mL of DI H_2O 3× and dried under vacuum overnight at 40 °C. After drying, 0.508 g of violet colored powder was recovered (83% yield).

Preparation of $LiCoPO_4$ Nanosheets: 0.050 g (0.11 mmol) of $Co_3(PO_4)_2 \cdot 4H_2O$ nanosheets were stirred for 15 minutes with 5 mL of DI H_2O and 25 mL of diethylene glycol (DEG). Next, 0.409 mL (0.409 mmol) of 1 M LiH_2PO_4 was added and the mixture was stirred for additional 30 minutes. The mixture was then transferred to a 42 mL Teflon-lined stainless-steel autoclave and reacted at 250 °C for 17 hours. After letting the reaction cool to room temperature naturally, the fuchsia-colored product was separated from the H_2O/DEG mixture using centrifugation at 10,000 rpm for 30 min. The product was washed 3 times with 30 mL of ethanol and 3x with 30 mL of DI H_2O. The nanosheets were kept in solution for characterization. Reactions with ethylene glycol (EG) were prepared in the same manner.

Preparation of $Mn_3(PO_4)_2 \cdot 3H_2O$ Nanosheets: In a beaker, 1.000 g (4.08 mmol) of $Mn(CH_3COO)_2 \cdot 4H_2O$ was dissolved in 15 mL of DI H_2O. In a different beaker, 0.358 g of $(NH_4)_2HPO_4$ was dissolved in 15 mL of water and the solution was added to beaker containing the Mn solution. The mixture was stirred for 30 minutes and the white precipitate was isolated via centrifugation at 10,000 rpm for 15 min. The nanosheets were washed wit 30 mL of DI water and were kept in solution for further use.

Preparation of $LiMnPO_4$ Nanosheets: To prepare $LiMnPO_4$, an already established synthetic approach was used.[15] 5.0 mL (0.122 mmol) of a 0.010 mg/mL of $Mn_3(PO_4)_2 \cdot 3H_2O$ nanosheets were added to 25 mL of DEG. The mixture was stirred for 15 minutes and 0.369 mL (0.369 mmol) of 1M LiH_2PO_4 was added. After stirring for 30 minutes, the dispersion was transferred to a 42 mL Teflon-line stainless-steel autoclave and reacted at 250 °C for 6 hours. The autoclave was allowed to cool down to room temperature and the white precipitate was separated from the liquid component via centrifugation at 10,000 rpm for 30 minutes. The product was washed with 30 mL of ethanol 3 times, followed by 30 mL of DI water 3 times. The nanosheets were dried under vacuum overnight at 40 °C to produce 0.041g of white powder (71 % yield).

Ball-Milling of $LiMnPO_4$ Nanosheets: For dry ball-milling, 0.040g of $LiMnPO_4$ was added to a SiN ball-milling vessel and 8 SiN balls. The material was ball-milled for 30 minutes at 100-400 rpm in a Fritsch Planetary Miller. The nanosheets were removed from the vessel and balls with 15 mL of ethanol. The dispersion was bath sonicated for 15 minutes and then characterized.

For wet ball-milling, the equivalent amount of the nanosheets were added to the milling vessel together with the 8 balls and 0.1-0.5 mL of ethanol or DI H_2O. The subsequent steps were identical to the dry ball-milling procedure.

Characterization: The composition of the metal phosphates was examined using a Bruker D8-Advance powder X-ray diffractometer (PXRD) with Co-Kα radiation (λ= 1.7889 Å) operated at 35 mA/40 kV and with a scanning rate of 0.1 sec per step over the 2θ range of 5-70°. Samples were prepared as either powder mounts or drop cast onto a glass slide and dried. The morphologies of the nanoproducts were inspected with a FEI Teneo field emission gun scanning electron microscope (FEG-SEM) in either SEM (5-10 kV) and STEM mode (30 kV). Energy dispersive spectroscopy (EDS) was performed via an Oxford system on the same instrument to confirm elemental composition of the observed morphologies. SEM samples were either drop casted on a Si wafer or pressed into a pellet, while STEM samples were drop casted on either formvar or lacey carbon grids and both type of samples were allowed to air dry before characterization. Additionally, a transmission electron microscope (TEM) equipped with selected area electron diffraction (SAED) was used, the FEI Tecnai 20 (200 kV). High resolution TEM (HRTEM) was performed at Georgia Tech on a FEI G2 Tecnai F30 operated at 300 kV. TEM/HRTEM samples were prepared in the same manner as STEM samples described above.

Results and Discussion

$LiCoPO_4$ nanosheets were synthesized from a $Co_3(PO_4)_2 \cdot 4H_2O$ precursor in H_2O:DEG and H_2O:EG mixtures. Various reaction times, solvent ratios, temperatures and Li sources were explored to find the optimal conditions for nanosheet formation. Additionally, $LiMnPO_4$ nanosheets were ball-milled with and without solvent with the goal of decreasing their lateral dimensions while retain their 2D morphology, for the purpose achieving better battery performance.

Synthesis of $Co_3(PO_4)_2 \cdot 4H_2O$ Nanosheets

The cobalt phosphate nanosheet precursor was synthesized by a method utilized previously in the formation of hureaulite, i.e. $Mn_5(PO4)_2(PO_3OH)_2 \cdot 4H_2O$.[16] In the adapted synthesis, $CoCl_2 \cdot 6H_2O$ was used as the cobalt source and concentrated H_3PO_4 as the phosphate source. NaOH was added to the solution to decrease the pH and allow the cobalt phosphate to precipitate out of it. The mixture was allowed to reflux for 18 hours. After washing the violet precipitate, its PXRD pattern was matched to a cobalt phosphate hydrate, $Co_3(PO_4)_2 \cdot 4H_2O$ (ICDD# 00-034-0844) (black pattern in Figure 5.1). Additionally, the same reaction was attempted at room temperature and 60 °C, but both reactions yielded the pink-colored octahydrate instead (pink and green patterns in Figure 5.1) indicating that temperature is essential to produce the desired compound. Although the cobalt phosphate tetrahydrate is not as widely studied as the octahydrate derivative, it was prepared previously by suspending cobalt (II) hydrogen phosphate hydrates in DI water at 80-96 °C for 1 day.[17] Not much information was available about the exact structure until recently when Manyala and coworkers used a hydrothermal method to synthesize it. [18] Their published PXRD pattern resembles ours closely,

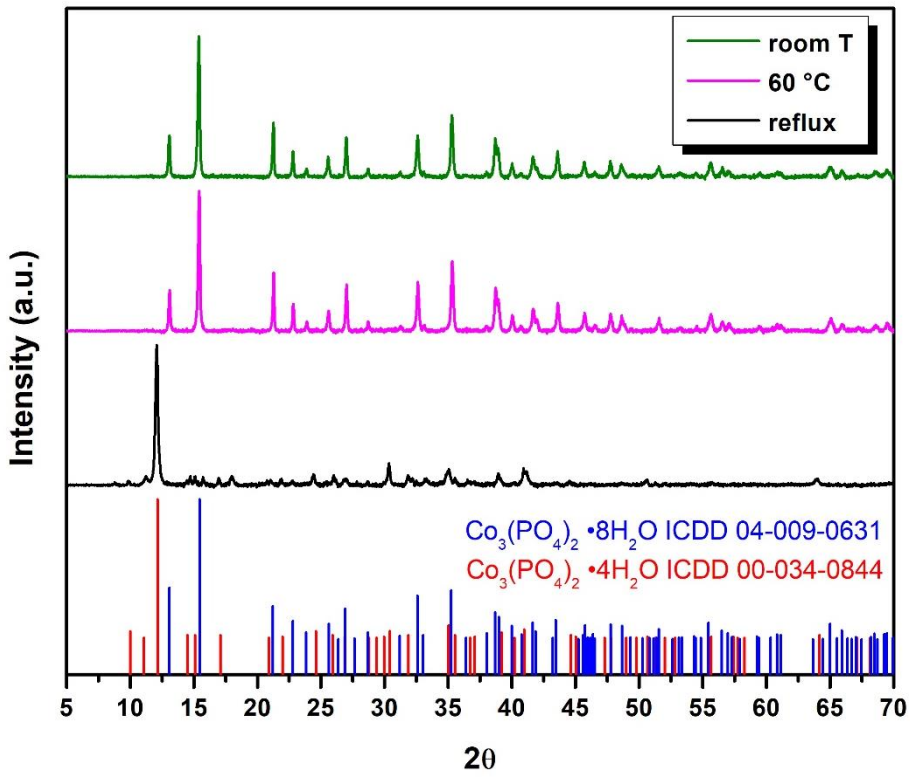

Figure 5.1. PXRD patterns of Co precursor nanosheets synthesized at different temperatures

but the two patterns are not identical, which implies that the two materials might have some structural differences. Additional characterization is required to determine them with certainty.

The morphologies and elemental compositions of our cobalt phosphates were evaluated by SEM-EDS and STEM. The reflux product was determined to be uniformly composed of rectangular nanosheets with lateral dimensions between 1-5 μm (Figure 5.2 A-B). The Co:P ratio was determined by EDS to be on average 1.47:1, corroborating the previously hypothesized

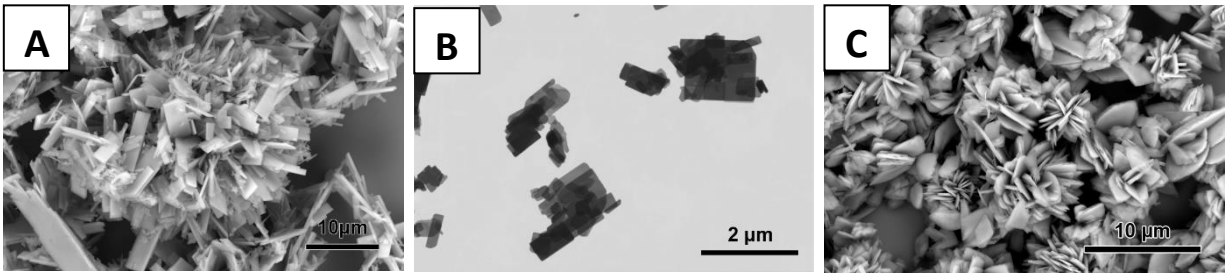

Figure 5.2. SEM (A) and STEM (B) images of $Co_3(PO_4)_2 \cdot 4H_2O$ nanosheets and SEM image of $Co_3(PO_4)_2 \cdot 8H_2O$ (C)

elemental composition of $Co_3(PO_4)_2 \cdot 4H_2O$. Furthermore, the octahydrates obtained from the room temperature and 60 °C reactions had a flower-like morphology composed of multiple petals with pointed corners (Figure 5.2 C).

Synthesis of $LiCoPO_4$ with DEG

Lithium cobalt phosphate was synthesized using stoichiometric amounts of $Co_3(PO_4)_2 \cdot 4H_2O$ nanosheets and lithium salts in a H_2O/DEG mixture. Several parameters of the reaction were varied in order to obtain a uniform nanosheet product. Firstly, reaction time was altered in the reaction of the cobalt phosphate nanosheets with LiH_2PO_4 in 5:25 H_2O:DEG solvent mixture at 250 °C. Notably, reactions at 180 °C were attempted but yielded only starting material, so all future reactions were executed at 250 °C. Reaction times of 3, 5 and 17 hours were tested, and PXRD was used to characterize the products. As shown in Figure 5.3, at 3 hours, $LiCoPO_4$ already begins forming, but some of the starting material is still present.

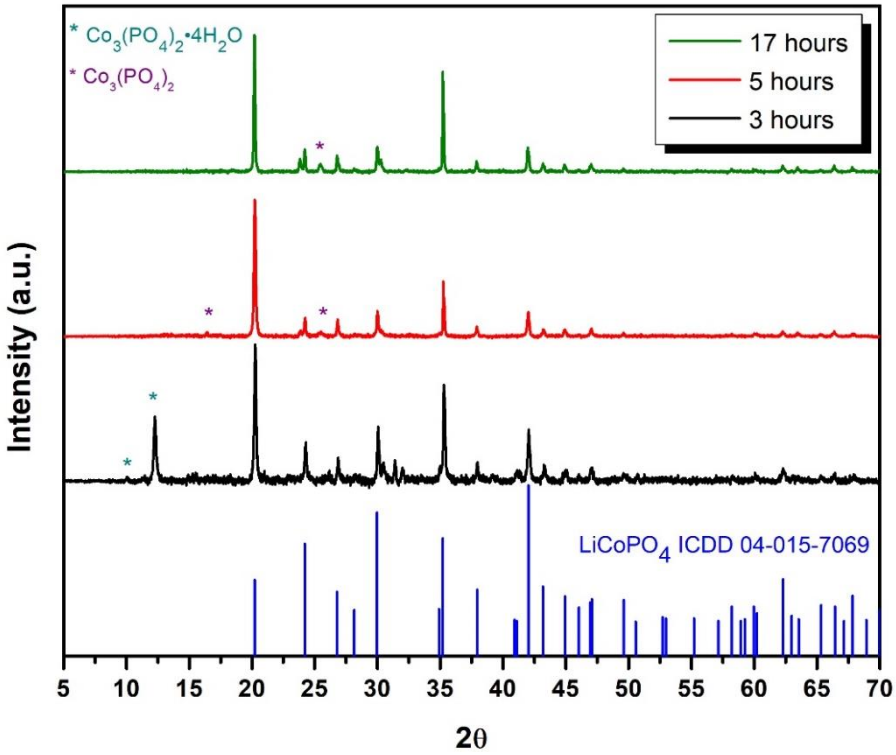

Figure 5.3. PXRD patterns for time study of the formation of $LiCoPO_4$

Increasing the time to 5 hours eliminates any precursor, but also leads to the formation of monoclinic $Co_3(PO_4)_2$. Allowing the reaction to proceed for 17 hours shows similar results to the 5-hour reaction, suggesting that perhaps not enough lithium is available to form more $LiCoPO_4$; instead, the remaining Co nanosheet precursor forms a different cobalt phosphate compound under the solvothermal conditions.

SEM and STEM were used in conjunction to evaluate the morphology of each reaction. At 3 hours, large thin sheets are seen growing out of the $Co_3(PO_4)_2 \cdot 4H_2O$ precursor material and a significant amount of the tetrahydrate nanosheets is still present (Figure 5.4 A). At 5 hours, the 5-20 µm sheets were becoming the predominant morphology (Figure 5.4B) and at 17 hours both large sheets and some thicker, 3-D crystals were observed (Figure 5.4 C). SAED of the nanosheets was indexed and compared to the simulated single crystal diffraction pattern verifying the identity of the nanosheets as $LiCoPO_4$ (Figure 5.4 E-F). It was also determined that

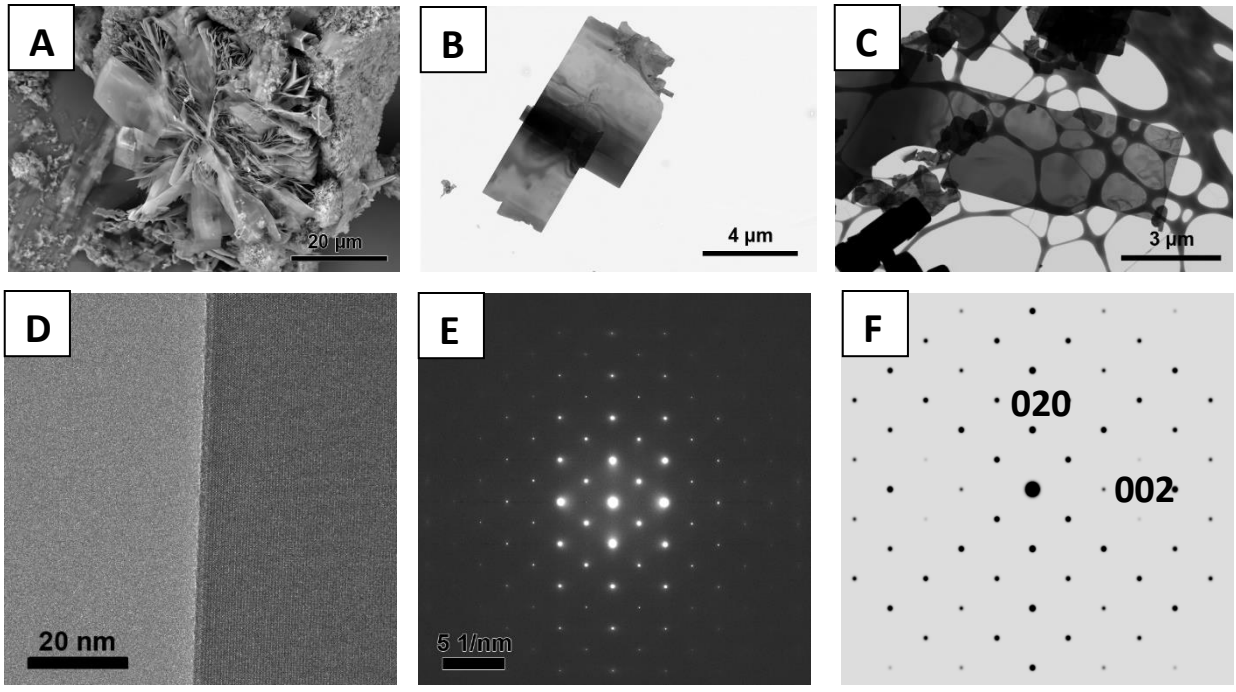

Figure 5.4. SEM image of a 3-hour reaction (A) and STEM images of a 5-hour (B) and 17-hour (C) reaction. HRTEM of a nanosheet from a 17-hour reaction (D) with the respective SAED (E) and simulated single crystal diffraction pattern (F)

the sheet grow along the (200) plane, which is also confirmed by the relative intensity of the (200) peak in the PXRD pattern.

Next, the importance of the ratio of H_2O:DEG in the reaction was evaluated in the reaction between $Co_3(PO_4)_2 \cdot 4H_2O$ and LiH_2PO_4. The volumetric ratio between the solvents was varied from 100% H_2O to 100% DEG and the final product was characterized with PXRD (Figure 5.5). In the H_2O and DEG only-containing reactions, various Co-containing compounds were formed: Co_3O_4, $H_2Co_3(PO_4)_2(OH)_2$, $Co_7H_4(PO_4)_6$ and $Co_3(PO_4)_2$ were found. Once DEG is added, in the 15:15 mL reaction, $CoHPO_4$ was formed as well as some $LiCoPO_4$ and $LiCoO_2$. Increasing the DEG amount further to 25 and 29 mL leads to the formation of primarily $LiCoPO_4$ with a small amount of $Co_3(PO_4)_2$. The only observable difference between the patterns of the two reactions was in the relative intensity of the peaks. It was shown that in the reaction with

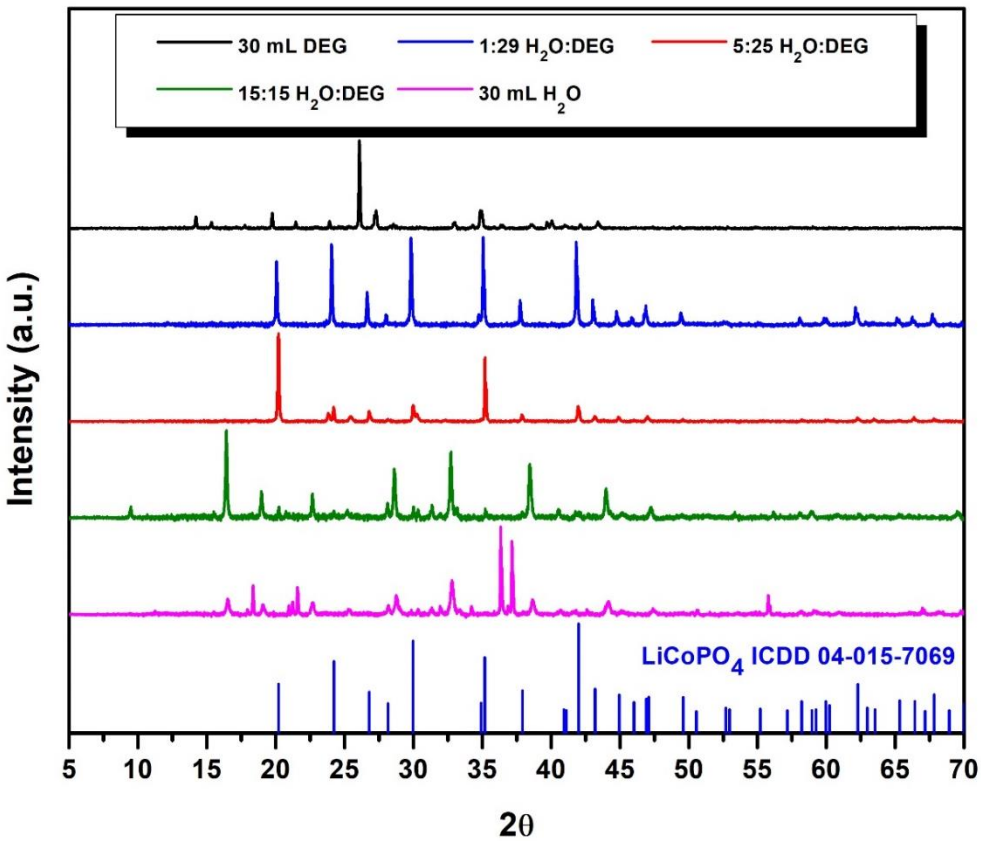

Figure 5.5. PXRD of H_2O:DEG solvent study

1:29 ratio of H_2O:DEG most of the peaks vary in intensity, while in the 5:25 displays an orientation effect common in 2D materials, which causes one or more peaks to be much more intense than the others. This suggest that although they are similar in composition, the morphology obtained from the two reactions is different. This was confirmed by SEM (Figure 5.6). The large 2D sheets seen in the 5:25 reaction were not present in the 1:29 reaction. Instead, smaller 3D crystal that were ~1 µm in size were observed (Figure 5.6). Polyols, such as DEG, can adsorb preferentially to certain crystal facets of the material during the crystal formation resulting in growth along specific crystal planes. Thus, it is not unlikely that having a higher volume of DEG present leads to adsorption to other crystal planes as well and the hindrance of the formation of large sheets. Such results indicate that the ratio between the solvents is of crucial importance in order to achieve the desired morphology.

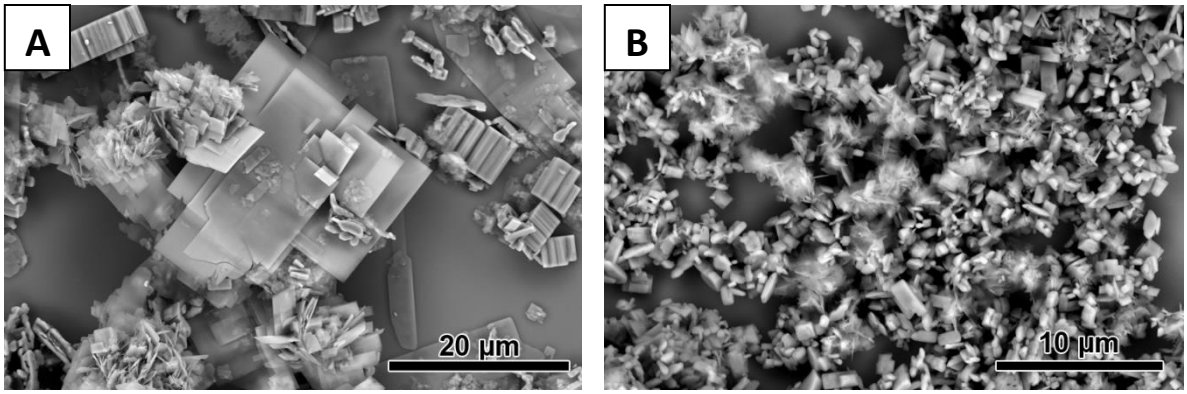

Figure 5.6. SEM images of 5:25 (A) and 1:29 (B) H_2O:DEG reaction

The solvothermal reaction was attempted with various different Li salts as well to evaluate if the method could be applied with carrying reagents. To this end, LiCl, $LiNO_3$ and Li_3PO_4 were substituted as the lithium source in a reaction with 5:25 mL H2O:DEG. The first two salts were added as 1M aqueous solution as previously done with LiH_2PO_4, while the Li_3PO_4 was added as a powder since it's insoluble in H_2O. The $LiNO_3$ reaction didn't yield any LiCoPO4 and instead showed only starting material. The other two salts formed the desired

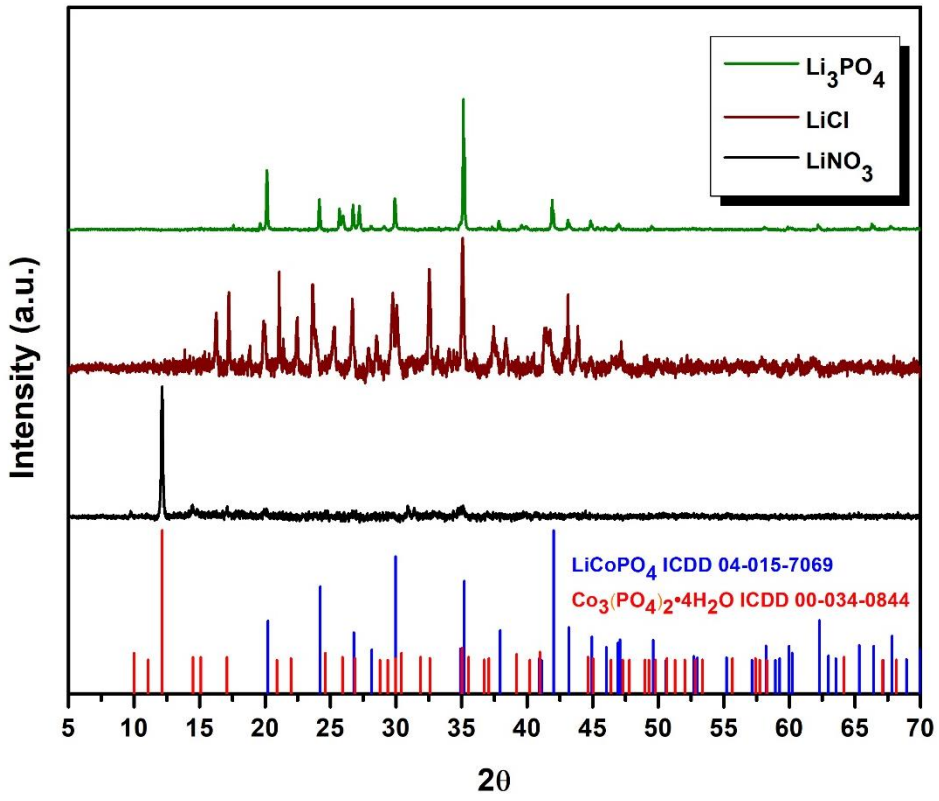

Figure 5.7. PXRD of Li salts study reactions

material, while also forming a significant amount of side product such as $Co_3(PO_4)_2$ and $Li_4P_2O_7$ (Figure 5.7). Though $LiCoPO_4$ was formed according to PXRD, SEM imaging determined that the morphologies were not the desired thin nanosheets and instead an assortment of thicker platelets, rods and 3D crystals. This suggests that the choice of Li source and more importantly the present anion impacts the formation of the final product, which has been previously observed with the $LiMnPO_4$ nanosheet synthesis in H_2O:DEG mixture.[15]

Synthesis of $LiCoPO_4$ with EG

Once the $LiCoPO_4$ nanosheets were successfully synthesized in H_2O:DEG, we attempted to expand the methodology to a similar solvent, i.e. ethylene glycol (EG). Reaction conditions were kept identical to the DEG reactions; temperature was kept at 250 °C, reaction time at 17

hours and stoichiometric ratio between the reactants remained unchanged. We varied the H_2O:EG ratio and characterized the products. First, PXRD revealed the products formed (Figure 5.8). As with DEG, 15:15 mL H_2O:EG reaction produced only small amount of $LiCoPO_4$ and another species was the predominant product, $H_4CO_{5.5}(PO_3)_4(OH)_3$. Once the EG concentration was increased to 5:25 and 1:29, $LiCoPO_4$ became the main product. The most intense peak observed in the PXRD pattern, however, was the one corresponding to (020) crystal plane. This was different from the DEG reaction where the nanosheets grew along the (200) plane suggesting that using different solvents lead to perhaps different crystal growth mechanism. SAED needs to be done to confirm that the observed sheets are growing along the (020) plane and not (200) one as previously seen. If that is the case, synthesis of $LiCoPO_4$ using EG might be particularly important as growing sheets along (0k0) crystal planes are desirable for fast lithium diffusion in battery materials.[2, 19]

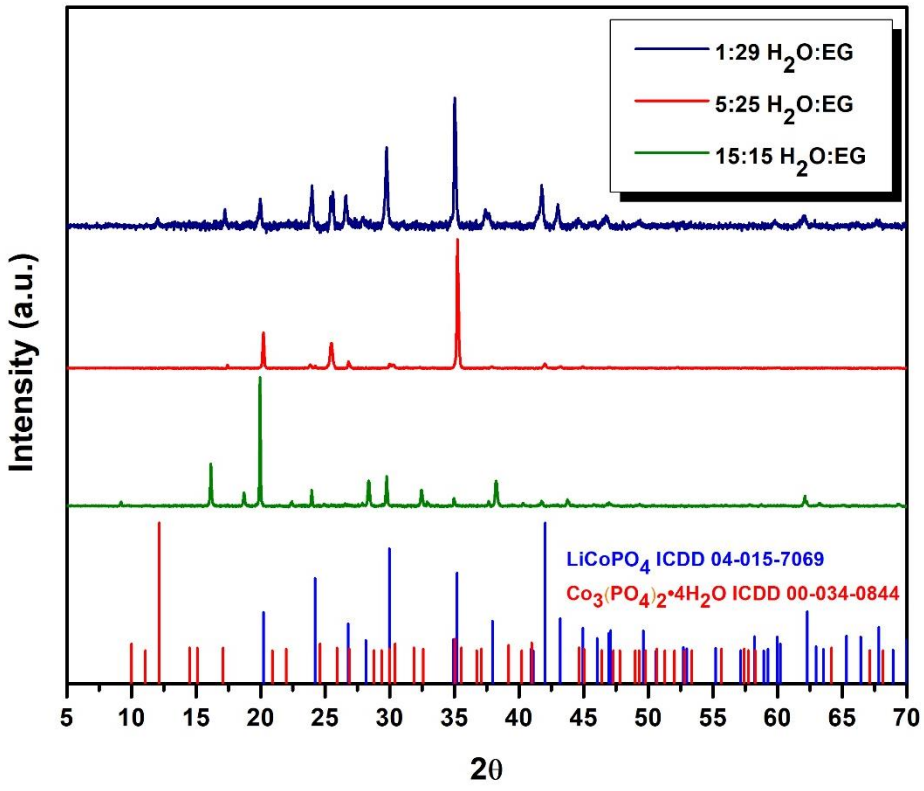

Figure 5.8. PXRD of H_2O:EG solvent study

The products were also examined by STEM to study their morphology. In the 5:25 H_2O:EG reaction, two distinct two-dimensional morphologies were observed: relatively thin sheets with multiple holes in them were seen and much thicker, belt-like sheets (Figure 5.9 A and B respectively). Both were 20-30 μm in lateral dimensions and had Co:P ratio of 1:1 as determined by EDS suggesting they were both $LiCoPO_4$. In the 1:29 H_2O:EG reaction, similar porous sheets were present (Figure 5.9 C), but some uniformly thin sheets were observed as well (Figure 5.9 D). The latter 2D morphology appear to crystalize in flower-like bundles and resemble the thickness and uniformity of the nanosheets obtained from the 5:25 H_2O:DEG reactions.

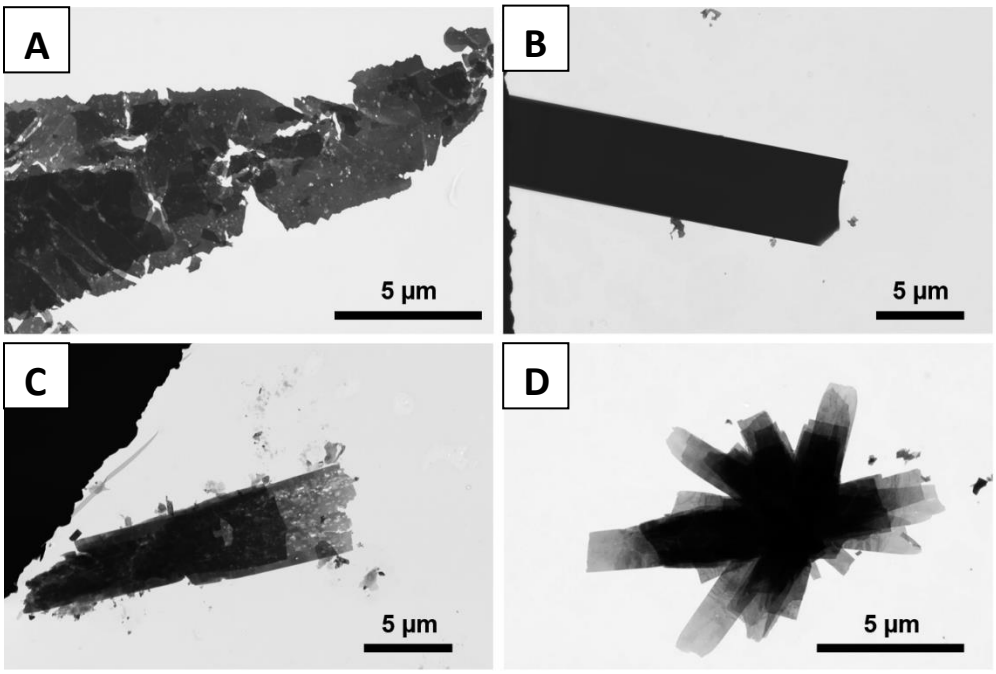

Figure 5.9. STEM images of product from a 5:25 H_2O:EG reaction (A and B) and 1:29 H_2O:EG reaction (C and D)

Ball-milling of $LiMnPO_4$

$LiMnPO_4$ nanosheets were previously synthesized and a methodology was established for achieving optimal results.[15] Their battery performance was also evaluated and while promising, it

was hypothesized that their large lateral dimensions may influence their performance as seen with other battery materials as well.[20] Thus, reduction of lateral dimensions was attempted using planetary ball-milling at different milling speeds with or without a liquid medium with the aim to decrease size but retain 2D morphology.

First, $LiMnPO_4$ nanosheets were ball-milled without any additives at 100 and 200 rpm for 30 minutes. Pristine $LiMnPO_4$ nanosheets had dimensions of 5-10 μm as demonstrated by TEM imaging (Figure 5.10 A). Once ball-milled, the nanosheets reduced in lateral dimension significantly – 2D morphologies with sizes of 200-500 nm were observed in both 100 and 200 rpm experiments (Figure 5.10 B and C). However, the formation of $LiMnPO_4$ nanoparticles was also observed suggesting that the dry ball-milling method might be too harsh to preserve the 2D morphology completely. Alternatively, the addition of a liquid medium to the ball-milling was employed to rectify this issue as it is expected to be gentler.

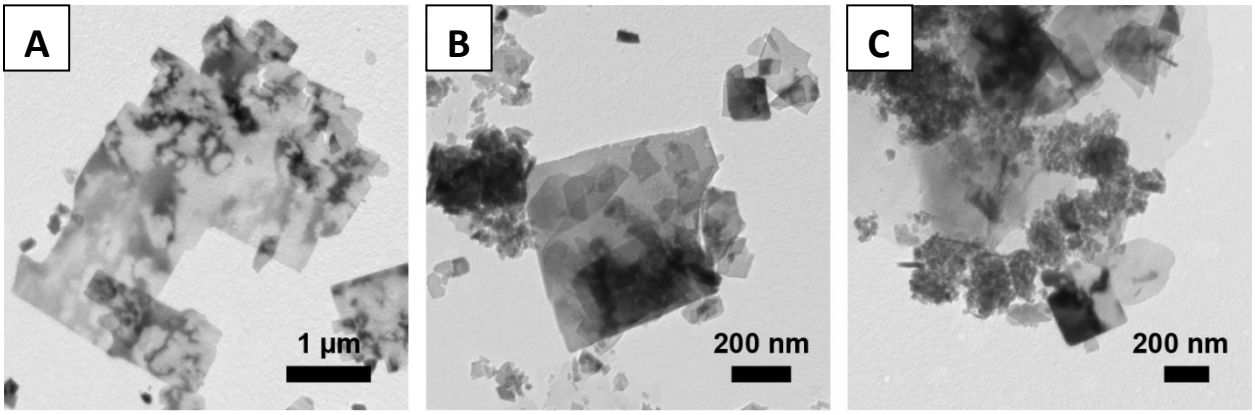

Figure 5.10. TEM images of $LiMnPO_4$ nanosheets – pristine (A), ball-milled at 100 rpm (B) and 200 rpm (C)

First, ethanol (EtOH) was added to the ball-milling vessel together with the $LiMnPO_4$ powder. Amounts between 0.1 and 0.5 mL were used and the ball-milled products were characterized. At 0.1 mL of EtOH, smaller nanosheets with sizes similar to the dry ball-milling were observed at both 100 and 200 rpm (Figure 5.11 A and B). However, small nanoparticles

were seen as well prompting us to increase the added volume. At 0.25 mL of EtOH, ball-milling was done at speeds between 100-400 rpm. While at lower rotating speeds, the sheets didn't decrease in size significantly (Figure 5.11 C and D), but at 300 and 400 rpm smaller sheets were observed (Figure 5.11 E and F). Regrettably, nanoparticles were still forming indicating that higher rpm with that volume of ethanol weren't the ideal parameters. Finally, the EtOH amount was increased to 0.5 mL and only the higher rotating speeds were tested since the lower ones yielded no significant change in size with the smaller EtOH volume. At 300 and 400 rpm, some of the nanosheets had decreased in lateral dimension, but a significant amount of them remained large meaning that amount of EtOH was most likely too large. Throughout the set of experiments

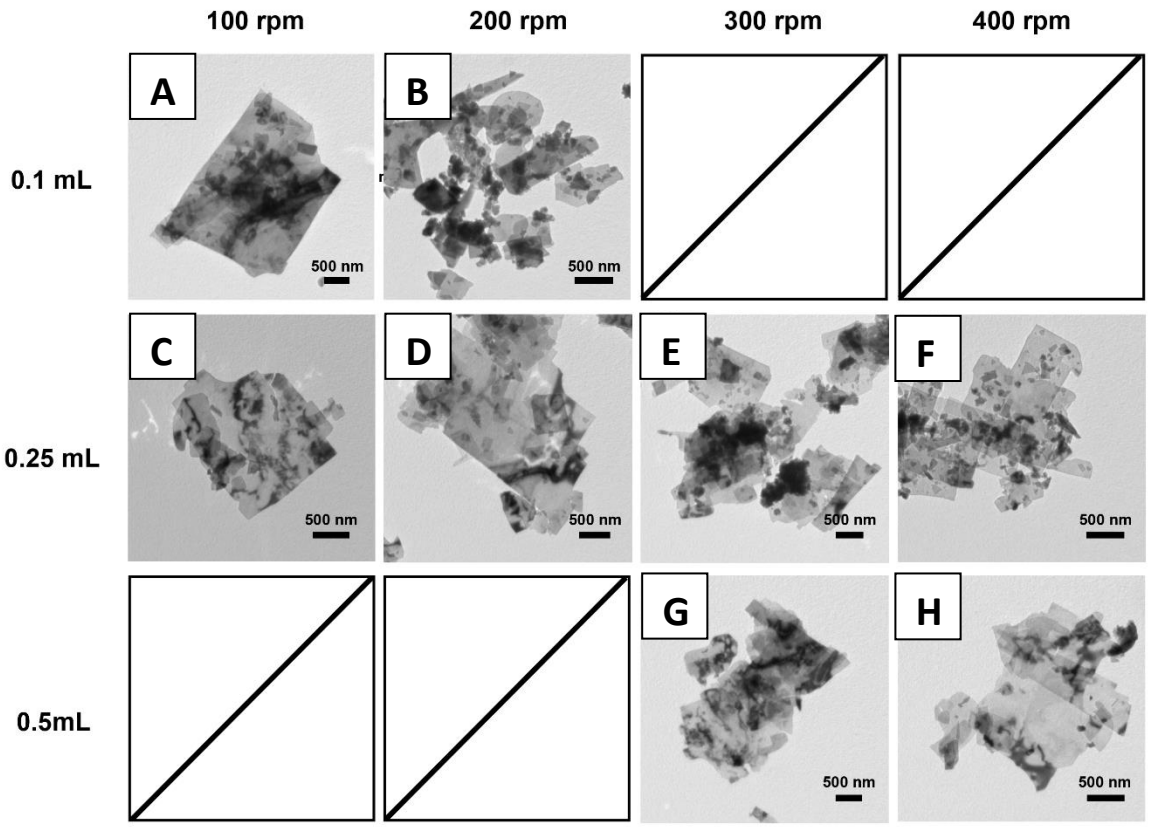

Figure 5.11. TEM images of $LiMnPO_4$ nanosheets – (1) 0.1 mL EtOH at 100 (A) and 200 rpm (B), (2) 0.25 mL of EtOH at 100 (C), 200 (D), 300 (E) and 400 rpm (F) and (3) 0.5 mL EtOH at 300 (G) and 400 rpm (H)

with ethanol, we determined that lower volume of ball-milling liquid media delivered the most promising results despite the formation of nanoparticles during the process.

Considering the results obtained so far, we decided to test a different medium to improve the final results. We theorized that when using ethanol, especially at lower volumes, some evaporation could have occurred once the liquid was deposited into the milling vessel due to its high evaporation rate. Thus, DI H_2O replaced ethanol as our milling medium. $LiMnPO_4$ nanosheets were milled with 0.1, 0.175 or 0.25 mL of water. Overall, it appeared that nanoparticles were formed a lot less when using water instead of EtOH as shown in the TEM images in Figure 5.12. For example, when using 0.1 mL of H_2O we didn't observe any nanoparticles until 300 rpm, while the same volume of EtOH produced them as early as 100 rpm.

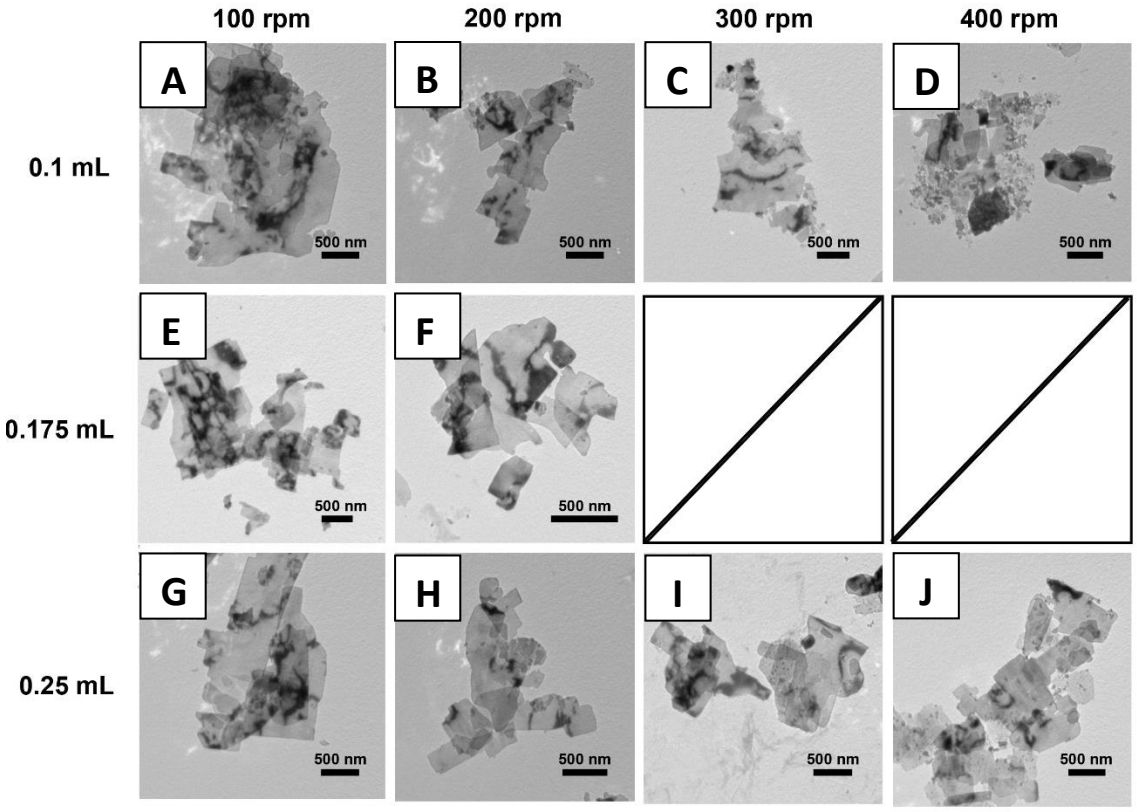

Figure 5.12. TEM images of $LiMnPO_4$ nanosheets – (1) 0.1 mL H_2O at 100 (A), 200 (B), 300 (C) and 400 rpm (D), (2) 0.175 mL of H_2O at 100 (E) and 200 rpm (F), and (3) 0.25 mL H_2O at 100 (G), 200 (H), 300 (I) and 400 rpm (J)

Higher volumes of water produced sheets with mixed sizes; some sheets were ~500-700 nm in lateral dimensions, while others seemed more similar to the pristine $LiMnPO_4$. From this study, we concluded that the best conditions, when using water as a milling medium, is lower volume at speed of 200 to 300 rpm.

Conclusion

$LiCoPO_4$ nanosheets were successfully synthesized from a $Co_3(PO_4)_2 \cdot 4H_2O$ nanosheet precursor by solvothermal reaction at 250 °C. The most consistent results were achieved in a mixture of 5:25 mL of H_2O:DEG where nanosheets with lateral dimensions of 5-20 μm were synthesized. It was discovered that the ratio between the solvents was a crucial parameter that yielded a variety of other cobalt-containing compounds when varied from the ideal 5:25 ratio. Additionally, the lithium salt was varied and while the synthesized product in some cases was $LiCoPO_4$, the morphology was more 3D than the desired 2D. So LiH_2PO4 proved to be the ideal lithium source for our reactions. Two-dimension morphologies of $LiCoPO_4$ also were synthesized in H_2O:EG mixtures. The products from these reactions were thinner, porous sheets as well as thicker, uniform ones. Based on PXRD patterns, the sheets grow along the (020) crystal plane, which differs from the ones produced in DEG, where they grew along the (200) instead. These results suggest that the composition of the final product is the same and the solvent plays a major role in determining morphology and orientation. Whereas morphology control has been demonstrated before with various polyol solvents, our results with DEG are somewhat unusual because it has been shown that both DEG and EG solvents produce $LiCoPO_4$ with exposed (020) facets in binary systems.[13]

Our work on the synthesis of 2D $LiCoPO_4$ has shown some extremely promising results, and this project has excellent potential. One of the biggest challenges is to fully characterize the cobalt precursor as the information in the literature about it is minimal and in a way contradicting. Thus, determining the exact structure of the starting material might reveal information about the growth mechanism of the $LiCoPO_4$ nanosheets. Additionally, considering

the promising results obtained with EG and DEG, more polyol solvents could be used to discover the ideal reaction parameters.

Our work also achieved minimization of the lateral dimensions of $LiMnPO_4$ nanosheets via milling techniques while still maintaining their 2D morphology. Wet milling experiments showed some very promising results that were much improved compared to the dry milling. Although many different solvents could be used, water seems like the logical choice because it does not react with the nanosheet material, is easy to work with, and produces consistent results. Additional avenues worth exploring are the amount of material put in the vessel, the number of milling balls, and the total milling time.

The two-dimensional nanostructuring of $LiMPO_4$ materials has come far in the past decade, but much remains unexplored. The successful production of uniform, thin nanosheets with certain exposed facets has been in the forefront of their study. Our simple synthetic approach with the use of nanosheet precursor at moderate temperatures and the ability to control the lateral dimensions of the final products has been a leap forward in making $LiMnPO_4$ and $LiCoPO_4$ adaptable for the ever-evolving battery industry, similarly to the commercially available $LiFePO_4$.

References

1. Fisher, C. A. J.; Hart Prieto, V. M.; Islam, M. S., Lithium Battery Materials $LiMPO_4$ (M = Mn, Fe, Co, and Ni): Insights into Defect Association, Transport Mechanisms, and Doping Behavior. *Chemistry of Materials* **2008,** *20* (18), 5907-5915.

2. Rui, X.; Zhao, X.; Lu, Z.; Tan, H.; Sim, D.; Hng, H. H.; Yazami, R.; Lim, T. M.; Yan, Q., Olivine-Type Nanosheets for Lithium Ion Battery Cathodes. *ACS Nano* **2013,** *7* (6), 5637-5646.

3. Oh, S. W.; Myung, S.-T.; Oh, S.-M.; Oh, K. H.; Amine, K.; Scrosati, B.; Sun, Y.-K., Double Carbon Coating of $LiFePO_4$ as High Rate Electrode for Rechargeable Lithium Batteries. *Advanced Materials* **2010,** *22* (43), 4842-4845.

4. Yoo, H.; Jo, M.; Jin, B.-S.; Kim, H.-S.; Cho, J., Flexible Morphology Design of 3D-Macroporous $LiMnPO_4$ Cathode Materials for Li Secondary Batteries: Ball to Flake. *Advanced Energy Materials* **2011,** *1* (3), 347-351.

5. Strobridge, F. C.; Clément, R. J.; Leskes, M.; Middlemiss, D. S.; Borkiewicz, O. J.; Wiaderek, K. M.; Chapman, K. W.; Chupas, P. J.; Grey, C. P., Identifying the Structure of the Intermediate, Li(2/3)CoPO(4), Formed during Electrochemical Cycling of LiCoPO(4). *Chem Mater* **2014,** *26* (21), 6193-6205.

6. Sronsri, C.; Danvirutai, C.; Noisong, P., Double function method for the confirmation of the reaction mechanism of $LiCoPO_4$ nanoparticle formation, reliable activation energy, and related thermodynamic functions. *Reaction Kinetics, Mechanisms and Catalysis* **2017,** *121* (2), 555-577.

7. Wu, J.; Li, Z.; Ju, L.; Li, D.; Zheng, J.; Xu, Y., Effect of the Impurities on Electrochemical Performance of High Voltage $LiCoPO_4$ Electrode. *Rare Metal Materials and Engineering* **2013,** *42* (4), 684-687.

8. Kreder, K. J.; Manthiram, A., Vanadium-Substituted LiCoPO4 Core with a Monolithic $LiFePO_4$ Shell for High-Voltage Lithium-Ion Batteries. *ACS Energy Letters* **2017,** *2* (1), 64-69.

9. Devaraju, M. K.; Rangappa, D.; Honma, I., Controlled synthesis of plate-like $LiCoPO_4$ nanoparticles via supercritical method and their electrode property. *Electrochimica Acta* **2012,** *85*, 548-553.

10. Brutti, S.; Manzi, J.; De Bonis, A.; Di Lecce, D.; Vitucci, F.; Paolone, A.; Trequattrini, F.; Panero, S., Controlled synthesis of $LiCoPO_4$ by a solvo-thermal method at 220°C. *Materials Letters* **2015,** *145*, 324-327.

11. Xing, L. Y.; Hu, M.; Tang, Q.; Wei, J. P.; Qin, X.; Zhou, Z., Improved cyclic performances of $LiCoPO_4$/C cathode materials for high-cell-potential lithium-ion batteries with thiophene as an electrolyte additive. *Electrochimica Acta* **2012,** *59*, 172-178.

12. Poovizhi, P. N.; Selladurai, S., Study of pristine and carbon-coated $LiCoPO_4$ olivine material synthesized by modified sol–gel method. *Ionics* **2011,** *17* (1), 13-19.

13. Ludwig, J.; Marino, C.; Haering, D.; Stinner, C.; Gasteiger, H. A.; Nilges, T., Morphology-controlled microwave-assisted solvothermal synthesis of high-performance $LiCoPO_4$ as a high-voltage cathode material for Li-ion batteries. *Journal of Power Sources* **2017,** *342*, 214-223.

14. Fang, L.; Zhang, H.; Zhang, Y.; Liu, L.; Wang, Y., Design and synthesis of two-dimensional porous Fe-doped $LiCoPO_4$ nano-plates as improved cathode for lithium ion batteries. *Journal of Power Sources* **2016,** *312*, 101-108.

15. Neher, G. R.; Salguero, T., *Two-dimensional metal phosphate nanomaterials for energy storage applications*. University of Georgia: 2018.

16. Neher, G.; Salguero, T. T., δ-Polymorph of Manganese Phosphate. *Crystal Growth & Design* **2017,** *17*, 4864-4872.

17. Hashimoto, K.; Toda, Y.; Hashimoto, K.; Arai, Y., Synthesis and Thermal Change of Cobalt(II) Phosphate Tetrahydrate. *Nippon Kagaku Kaishi* **1992,** *1992* (4), 369-374.

18. Mirghni, A. A.; Momodu, D.; Oyedotun, K. O.; Dangbegnon, J. K.; Manyala, N., Electrochemical analysis of $Co_3(PO_4)_2 \cdot 4H_2O$/graphene foam composite for enhanced capacity and long cycle life hybrid asymmetric capacitors. *Electrochimica Acta* **2018,** *283*, 374-384.

19. Peng, L.; Zhang, X.; Fang, Z.; Zhu, Y.; Xie, Y.; Cha, J. J.; Yu, G., General Facet-Controlled Synthesis of Single-Crystalline (010}-Oriented LiMPO4 (M = Mn, Fe, Co) Nanosheets. 2017; Vol. 29, pp 10526-10533.

20. Sun, H.; Varzi, A.; Pellegrini, V.; Dinh, D. A.; Raccichini, R.; Del Rio-Castillo, A. E.; Prato, M.; Colombo, M.; Cingolani, R.; Scrosati, B.; Passerini, S.; Bonaccorso, F., How much does size really matter? Exploring the limits of graphene as Li ion battery anode material. *Solid State Communications* **2017,** *251*, 88-93.

CHAPTER 6

CONCLUSIONS AND FUTURE WORK

Conclusions and Future Work

In Chapter II, I demonstrated the successful incorporation of Mg^{2+} in LaB_6 and the boride's exfoliation into nanosheets after a reaction with water. The modified structure was examined by EDS and the presence of magnesium was confirmed. Change is La environment was verified by SSNMR, while change in B one was suggested by Raman Spectroscopy. This method produced LaB_6 nanosheets, but lithiation methods remain the optimal approach to obtain thin and uniform 2D nanomorphologies.

In Chapters III and IV, I explored the same methodology with the alkaline earth metal hexaborides. The Mg^{2+} incorporation approach produced some interesting results. Similarly to the lithiation of CaB_6, the magnesiation route produced a modified structure with the addition of another species. The extra compound, which was also observed in BaB_6 reactions, was hypothesized to be a Mg-B species. To verify that, additional characterization is need, particularly one that could be executed in inert conditions such as synchrotron diffraction. The CaB_6 nanosheets produced during these experiments were obtained with shortened times for the modification step compared to previous Li^+ experiments.[1] These results support our hypothesis that using a metal ion from the same group as the metal in the boride can provide better incorporation and subsequent exfoliation. Moreover, the promising results from preliminary reaction with SrB_6 and BaB_6 were an indication that the magnesiation approach can be applied to

multiple species. Interestingly, the nanomorphologies obtained from the exfoliation of magnesiated strontium hexaboride varied significantly from those of the lithiated one.[2] While nanoparticles were the primary product of the reaction of $Li_xSr_{1-x}B_6$ with water, nanosheets were formed after the same reaction the Mg intermediate. This suggests that the pathway of formation of the modified structure differs somewhat between the two cases.

The work on the modification of metal hexaborides with Mg^{2+} is only in its introductory stages. One of the main questions that remain is what will happen if the magnesium ions are present in excess; one of the ways to do that is through a solvated electron system. In a such a reaction, elemental magnesium will be dissolved in liquid ammonia[3] and the stoichiometry between the metal ion and the boride can be precisely tuned. Reactions of LaB_6 in $Li/NH_{3(l)}$ system have achieved the best exfoliated 2D nanoproduct.[1] Furthermore, our work with calcium hexaboride showed that the size of the bulk crystals play a role in the degree of successful incorporation of the metal ion. Thus, an important part of study of the chemistry of the boride will be exploring different bulk powders to ensure that the modification method can be applied regardless of the source from which the boride was obtained. Finally, it is crucial to expand this work with other metal borides that are not part of the hexaboride group.

While a significant part of this work is devoted to understanding the chemistry of the modification of the metal borides, the industrial implications of our work are without a doubt extraordinary. The electronic, optical and chemical properties of the hexaboride nanosheets need to be studied and compared to the bulk. Moreover, 2D nanomorphologies of the hexaborides can drastically improve their processability completely eliminating the use of complex, high temperature methods. The ability of the nanosheets to remain suspended in solvents and form uniform coatings can expand where the hexaborides are being used in industry. Their application

as electron emitters, detectors, superconductors and thermoelectric materials can be further expanded by their 2D nanostructuring.[4-6] The expansion of our methodology to other borides can also steer the boride group further towards more exotic applications as high energy materials in rocket engines.[7]

Chapter V explored nanostructuring of lithium metal phosphates (LMPs). I demonstrated the formation of $LiCoPO_4$ nanosheets via a facile solvothermal method. During their synthesis, we discovered the most favorable conditions for their successful formation and dependence of their exposed crystal facets on the polyol used. Additionally, I studied the reduction of nanosheet lateral dimensions of previously synthesize $LiMnPO_4$ by planetary ball-milling. Dry and wet ball-milling was studied and it was determined that wet ball-milling reduces the formation of size morphologies. Water displayed better capabilities as a ball-milling medium than ethanol. The next steps in this work will be to characterize the battery performance of both of these nanosheet types and compare them to other 2D nanostructures. It is important to evaluate the dependence of their electrochemical performance on their lateral dimensions in order to determine their potential to be commercialized as another member of the lithium metal phosphate group, i.e. $LiFePO_4$. As two-dimensional energy storage materials have shown incredible promise in the formation of cathodes with their high surface area and high rate capabilities,[8] the synthesized LMP nanosheets have great potential that can surpass their oxide counterparts.

The development of new methods to produce nanosheets of different materials remains one of the top goals of the material science community. In this work, I demonstrate two different methods to produce nanosheets – a top down Mg^{2+} incorporation method to produce metal hexaboride nanosheets and a bottom up solvothermal approach to produce $LiCoPO_4$ ones. While

vastly different, both methods yield favorable results. More importantly, they aim to motivate the pursuit of scientific enhancement and progress.

References

1. Ramachandran, R. Nanostructured metal borides and metal fluorides. University of Georgia, Athens, Georgia, 2017.

2. Ramachandran, R.; Salguero, T. T., Nanostructuring of Strontium Hexaboride via Lithiation. *Inorganic Chemistry* **2018,** *57* (1), 4-7.

3. Kraus, C. A., Solutions of Metals in Non-Metallic Solvents. VI. The Conductance of the Alkali Metals In Liquid Ammonia. *Journal of the American Chemical Society* **1921,** *43* (4), 749-770.

4. Vandenberg, J. M.; Matthias, B. T.; Corenzwit, E.; Barz, H., Superconductivity of some binary and ternary transition-metal borides. *Materials Research Bulletin* **1975,** *10* (9), 889-894.

5. Swanson, L. W.; Gesley, M. A.; Davis, P. R., Crystallographic dependence of the work function and volatility of LaB_6. *Surface Science* **1981,** *107* (1), 263-289.

6. Aida, T.; Honda, Y.; Yamamoto, S.; Kawabe, U., Preparation, vapor pressure, and thermionic emission properties of BaB_6 powder. *Journal of Applied Physics* **1981,** *52* (2), 1022-1029.

7. Bondarchuk, S. S.; Matveev, A. E.; Promakhov, V. V.; Vorozhtsov, A. B.; Zhukov, A. S.; Zhukov, I. A.; Ziatdinov, M. H. In *Synthesis and Properties of Energetics Metal Borides for Hybrid Solid-Propellant Rocket Engines*, Cham, Springer International Publishing: Cham, 2018; pp 511-519.

8. Rui, X.; Zhao, X.; Lu, Z.; Tan, H.; Sim, D.; Hng, H. H.; Yazami, R.; Lim, T. M.; Yan, Q., Olivine-Type Nanosheets for Lithium Ion Battery Cathodes. *ACS Nano* **2013,** *7* (6), 5637-5646.